TÉCNICO LISBOA

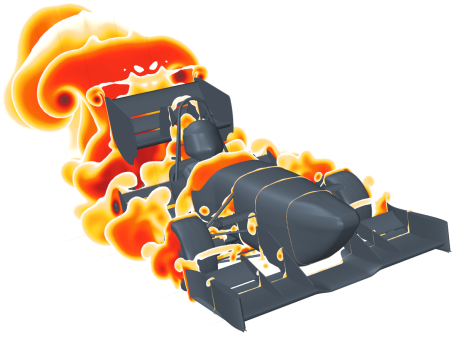

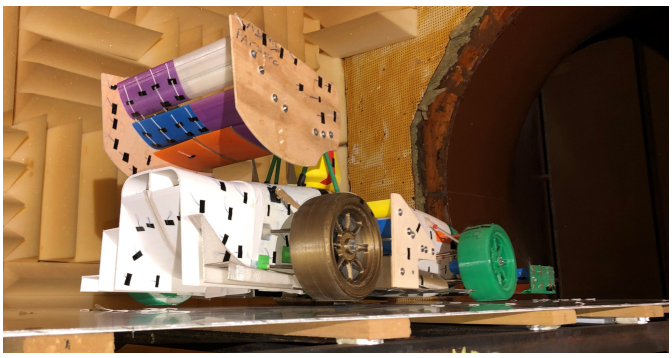

Aerodynamic Design and Wind Tunnel Testing of the Rear End of a Formula Student Vehicle

Luís Miguel Poeiras Afonso

Thesis to obtain the Master of Science Degree in

Aerospace Engineering

Supervisors: Prof. André Calado Marta
Prof. Luís Rego da Cunha de Eça

Examination Committee

Chairperson: Prof. Afzal Suleman
Supervisor: Prof. Luís Rego da Cunha de Eça
Member of the Committee: Prof. Duarte Manuel Salvador Freire Silva de Albuquerque

December 2022

I declare that this document is an original work of my own authorship and that it fulfills all the requirements of the Code of Conduct and Good Practices of the Universidade de Lisboa.

Acknowledgments

Fortunately, throughout this academic journey and particularly for this last stage, I could always count on those around me. For this would be impossible without you, I am extremely thankful.

First of all, I would like to express my gratitude to my supervisors, Professor André Marta and Professor Luís Eça, for allowing me and pushing me to seize this opportunity to further work on the project I was already very fond of, for their guidance and all the knowledge shared.

I would also like to thank the FST Lisboa team, for helping me with de needed resources. A special thank you note to the aerodynamics department of the FST10e, led by José Luciano, that introduced me to motorsports and that in between laughs and hard work ignited in me a curiosity for this world. João Morgado, it was great working with you with a common goal, and I am sure it improved both your work and mine. Another special thanks goes to Jaime Pacheco and Miguel Carreira who initially paved the way and constructed solid works that were on the base of this one.

To the many friendships that Aerospace brought me, I am eternally grateful, to Afonso, António, Diogo, Graça, Hugo, Luís, Luís, Miguel, and Tiago, among others, I am 100% sure that we will always look back to these years with a smile on our faces, while we joke about the many memories we've shared.

An honorable mention to Romão, who step out of his comfortable office and got his hands dirty to help during the calibration process, so that I could move forward. To Luís, who not only let me sleep under his roof so I was closer to the wind tunnel, but also trade his free time to make sure nothing bad would happen to me while the wind tunnel was turned on. To Gabriela, these last months, though tough, would be hell if we weren't there backing each other, as I hope we'll also be from this point forward.

I am definitely grateful for my snowmies, Gonçalo for helping me keep an open mind, João for showing me that spirit of sacrifice surely pays off, and Vasco for your support whenever needed.

Lastly, my biggest acknowledgment goes to my family, to my mother, my father, and my sister, everything I've accomplished is thanks to all your unconditional love, support, and encouragement. Words cannot express how lucky I am for you.

Resumo

Este trabalho foca-se não só em simulações MFC mas também na sua posterior validação via testes em túnel de vento para melhoria do desempenho aerodinâmico de um carro de Formula Student, de maneira a aumentar a confiança nos resultados obtidos nas simulações mas também a trilhar o caminho para que se recorra a este importante recurso com mais frequência.

Partindo de uma adaptação numa ferramenta que prevê o impacto da aerodinâmica nos resultados alcançáveis numa competição FS, foi obtido um valor ideal para o coeficiente de sustentação.

Foi também analisado o desempenho aerodinâmico do protótipo atual. Os difusores (laterais e traseiro) e a asa traseira foram identificados como os mais críticos, tendo sido escolhidos os difusores para melhoria. Quanto ao difusor lateral, a região de separação observada foi significativamente reduzida, mantendo a força vertical gerada. A região traseira do carro foi estendida e várias iterações de perfis para o difusor foram testadas e discutidas. Foi possível aumentar a downforce gerada cerca de 4.3% no design que foi posteriormente escolhido para imprimir e testar em túnel de vento.

As medições das forças durante os testes revelaram boa concordância com os valores previstos pelas simulações para o caso de escoamento alinhado com o carro e com ângulo de derrapagem $\beta = 4°$, os momentos foram substancialmente subestimados. Por outro lado, para $\beta = 10°$, os resultados foram considerados insatisfatórios e a visualização do escoamento com recurso a fios de lã, apesar de capturar alguns fenómenos importantes, ainda tem que ser melhorada.

Foi considerado que o novo design foi devidamente validado em túnel de vento.

Palavras-chave: Mecânica de Fluídos Computacional, Desempenho Aerodinâmico, Difusor, Dinâmica de Veículo, Validação, Visualização de Escoamento

Abstract

The aerodynamics design among Formula Student teams has been seeing increasing complexity. Particularly for the FST Lisbon team, the design phase of new prototypes is currently revolving solely around CFD simulations. This work focus on improving the performance of the car and validating it through wind tunnel testing, to boost confidence in the obtained results and to pave the way for it to become a more broadly resorted procedure.

By updating a lap simulator tool provided to predict the aerodynamic influence of the scores more accurately, the target was set to increase the downforce generated.

An aerodynamic performance assessment was performed by analyzing the simulation data from the baseline design. The most critical regions identified were both lateral and back diffusers, and the rear wing. The lateral diffuser was the first to be redesigned and simulated. The large separation region previously identified was successfully mitigated while granting that no downforce was lost. The rear region was also modified by extending the monocoque and varying the diffuser profile yielding a 4.3$\%$ increase in downforce.

This last design was scaled and 3D printed to be tested in the wind tunnel. Regarding the force measurements for slip angles of 0° and 4°, the results stood very close to the predicted CFD simulations while the moments were substantially underestimated. However, the results for $\beta = 10°$ were considered unsatisfactory and the flow visualization via wool tufts, while capturing some important phenomena, has to be further improved.

The redesign was validated in the wind tunnel.

Keywords: Computational Fluid Dynamics, Aerodynamic Performance, Car Diffuser, Vehicle Dynamics, Validation, Flow Visualization

Contents

Acknowledgments v
Resumo vii
Abstract ix
List of Tables xv
List of Figures xvii
Glossary xxi
Nomenclature xxii

1 Introduction **1**
1.1 Motivation 1
1.2 Formula Student Competition 2
1.3 Previous Work 4
1.4 Objectives 5
1.5 Thesis Outline 5

2 Racing Car Aerodynamics **7**
2.1 Vehicle Dynamics 7
2.2 Aerodynamics Phenomena and Effects 12
2.2.1 Pressure and Viscous Effects 12
2.2.2 Performance Related Effects 14
2.3 Main Aerodynamic Appendages 17
2.3.1 Wings 18
2.3.2 Undertray 21
2.3.3 Component Breakdown of Aerodynamic Performance 23
2.4 Aerodynamic Study Tools 24
2.4.1 Computational Simulations 24
2.4.2 Experimental Testing 25
2.5 Available Results 26
2.5.1 Wind Tunnel Test and Validation 27
2.5.2 CFD Test and Validation 29

3 Baseline Performance **31**
3.1 CFD Setup Parameters . . . 31
3.1.1 Computational Domain and Numerical Models . . . 31
3.1.2 Post-processing . . . 33
3.2 Vehicle Dynamics Simulation . . . 34
3.2.1 Dynamic Model . . . 34
3.2.2 Updated Model . . . 35
3.2.3 Aerodynamic targets definition . . . 36
3.3 Airflow Analysis . . . 39
3.3.1 General behavior . . . 40
3.3.2 Low Performance Regions Identification . . . 44

4 Car Modifications **46**
4.1 Lateral Diffuser . . . 46
4.1.1 Avoid Separation . . . 47
4.1.2 Increase Performance . . . 49
4.1.3 Airfoil Design . . . 51
4.2 Rear Diffuser . . . 53
4.2.1 Monocoque extension . . . 54
4.2.2 The Effect of Inverting the Top . . . 56
4.2.3 Double Suction Versus Rounded Profile . . . 58
4.3 Chosen Region . . . 61

5 CFD Validation Using Wind Tunnel **62**
5.1 Experimental Setup and Previous Notes . . . 62
5.1.1 Manufacturing New Parts . . . 62
5.1.2 Force Balance Calibration . . . 63
5.1.3 Wind Tunnel Testing Procedure . . . 65
5.1.4 Limitations . . . 66
5.2 Results . . . 67
5.2.1 CFD Simulations . . . 67
5.2.2 Wind Tunnel Testing . . . 70
5.2.3 CFD vs EFD . . . 71

6 Conclusions **74**
6.1 Achievements . . . 74
6.2 Future Work . . . 75

Bibliography **75**

A Results **81**

A.1 Wind Tunnel Testing 81

A.2 Full Car CFD Data 81

B Calibration **84**

B.1 Equations and Load Cases 84

List of Tables

4.1 Forces comparison among baseline and reduced lateral diffuser slopes designs 48
4.2 Efficiency comparison among baseline and reduced lateral diffuser slopes designs 48
4.3 Impact of the rotated SC flaps on the forces and efficiency of the car 50
4.4 Forces comparison between baseline and airfoil-shaped lateral diffuser designs 51
4.5 Impact of extending aft region of car on forces and efficiency 54
4.6 Impact of inverting aft upper surface on forces 56
4.7 Impact of inverting aft upper surface on efficiency 57
4.8 Forces comparison between designs with two expansion slopes and rounded back diffusers 58
4.9 Efficiency comparison between designs with two expansion slopes and rounded back diffusers 59

5.1 Forces relative changes between original and new design on CFD simulations for full car and 1/3 model 68
5.2 Comparison of changes in downforce among CFD and wind tunnel testing 72
5.3 Drag comparison of changes among CFD and wind tunnel testing 72

List of Figures

1.1 Competition Tracks 2
1.2 Power limited vs grip limited [5] 3

2.1 Car reference axis 7
2.2 Top View 8
2.3 Tire sideslip 9
2.4 Slip Ratio 9
2.5 Lateral Force vs Slip 10
2.6 Weighti Transfer 10
2.7 Steering 11
2.8 Pressure distribution around FS car 12
2.9 Boundary Layers 13
2.10 Displacement Thickness [12] 13
2.11 Flow separation under adverse pressure gradient [23] 14
2.12 Ground Effect 15
2.13 Vortex visualization in F1 car [29] 16
2.14 Vortex breakdown types [33] 17
2.15 Design boxes [34] 17
2.16 Front wing example and vortex visualization 18
2.17 Rear wing examples 18
2.18 Drag Reduction System [39] 19
2.19 Bullhorn and Gurney flap 20
2.20 Endplates characteristics 21
2.21 Underbody visualization 22
2.22 Vortex generators 22
2.23 Example of FS car with side wing and side cascade 23
2.24 Pressure Variation [40] 23
2.25 CFD modelling of turbulent jet [49] 25
2.26 UV Wool Tufts [8] 26
2.27 Wind tunnel examples 26
2.29 Comparison between CFD and WT 27

2.28 Wind tunnel testing methodology [2] . . . 28
2.30 Transition study . . . 29

3.1 CFD domain . . . 32
3.2 Mesh . . . 32
3.3 Post-Processing window pattern . . . 33
3.4 perfectLap Fluxogram . . . 35
3.5 Drag polar data and parabolic regression . . . 36
3.6 Predicted variation of the overall score with $C_L A$ . . . 37
3.7 Score variation of separated events with $C_L.A$ . . . 37
3.8 Score variation of endurance and efficiency with $C_L.A$ . . . 38
3.9 Aerodynamic package components . . . 39
3.10 Current distribution of downforce and drag. . . . 40
3.11 Static pressure on baseline design . . . 40
3.12 Axial and vertical pressure distribution . . . 41
3.13 Airflow speed at y=-100mm for baseline design . . . 41
3.14 Lateral diffuser-side cascade-rear wing system coupled behaviour visualization . . . 42
3.15 Vortex structures on front wing . . . 42
3.16 Bullhorn streamlines . . . 43
3.17 Side cascade vortex effect . . . 43
3.18 Outwash due to the airfoiled front wing enplates @ z=240mm . . . 44
3.19 Airflow under the car at y=-360.00mm plane . . . 44
3.20 Visualization of the effect of the driver's head on RW performance and body wake . . . 45
3.21 Friction coefficient on baseline design . . . 45

4.1 Studied lateral diffusers specimen . . . 47
4.2 Friction coefficient on the surface of the lateral diffuser (reduced slope) . . . 49
4.3 C_P plot of lateral diffuser on section cut y=360.0mm . . . 49
4.4 Airflow's total pressure coefficient @ y=360.0mm . . . 50
4.5 Projection of pressure coefficient in Z - lateral diffuser comparison . . . 51
4.6 Friction coefficient on diffusers (airfoil shaped lateral design) . . . 52
4.7 C_P plot of lateral diffuser on section cut y=360.0mm among cases studied . . . 52
4.8 Studied aft region specimen . . . 53
4.9 C_p plots on the rear wing for extended monocoque . . . 54
4.10 Pressure coefficient projected on Z acting on monocoque surface (comparison between baseline and extended rear) . . . 55
4.11 C_p plots on the side cascade for baseline and extended aft designs . . . 56
4.12 C_p plots on the rear wing for standard and inverted aft designs . . . 57
4.13 C_p plots on the body of the car for standard and inverted aft designs . . . 58

4.14 Comparison of pressure coefficient in Z between rounded and double suction back diffusers . . . 59
4.15 C_p plots on the back diffuser for the 3 diffuser profiles analyzed . . . 60
4.16 Airflow visualization on double suction back diffuser design . . . 60
4.17 Rear-side view of chosen design . . . 61

5.1 CAD designed module . . . 63
5.2 Printed module. . . . 63
5.3 Calibration setup . . . 64
5.4 Load case sheet example. . . . 65
5.5 Extensometer data example cases . . . 65
5.6 WT mounting setups . . . 66
5.7 Comparison of CFD component share on forces . . . 68
5.8 C_{P_Z} comparison between full model and 1/3 . . . 69
5.9 C_{F_X} comparison between full model and 1/3 . . . 69
5.10 Forces and moments obtained for $\beta = 4°$ for 6000 samples . . . 70
5.11 Downforce measure for $\beta = 10°$ . . . 71
5.12 Rear view capture $\beta = 0°$ . . . 72
5.13 Rear view capture $\beta = 4°$ . . . 73
5.14 Rear view capture $\beta = 10°$ . . . 73

A.1 Comparison of obtained forces among full size CFD, 1/3 scale CFD, and WT testing . . . 81
A.2 Lateral diffuser iterations . . . 82
A.3 Aft region iterations . . . 83

B.1 Calibration equations . . . 84
B.2 Full list of calibration load cases . . . 85

Glossary

AMR	Adaptive mesh refinement
AoA	Angle of attack
AR	Aspect ratio
BC	Boundary condition
BH	Bullhorn
BL	Boundary layer
BSL	Baseline
CAD	Computer-aided design
CFD	Computational Fluid Dynamics
CNC	Computerized numerical control
DF	Downforce
DNS	Direct numeric simulation
DoF	Degrees of freedom
DRS	Drag reduction system
EP	Endplate
F1	Formula 1
FS	Formula Student
FST	Formula Student Team Técnico
FW	Front wing
GE	Ground effect
LES	Large eddy simulation
LiDAR	Light detection and ranging
LT	Load transfer
MBR	System composed of the back diffuser, rear wing and monocoque
MFC	Mecânica de fluidos computacional
NS	Navier-Stokes
RANS	Reynolds-Averaged Navier-Stokes
RD	Research and Development
RH	Ride height
RW	Rear wing
SST	Shear stress transport
TKE	Turbulent kinetic energy
VG	Vortex generator
WT	Wind tunnel

Nomenclature

Greek symbols

α	Angle of attack.
β	Angle of side-slip.
δ	Steering angle.
μ	Molecular viscosity coefficient.
Ω	Angular velocity of the tyre.
ω	Vorticity.
ϕ	Rolling angle.
ψ	Yawing angle.
ρ	Density.
τ	Shear stress.
θ	Pitching angle.

Roman symbols

A	Area.
a	Distance between CG and front axle.
b	Distance between CG and rear axle.
C_D	Coefficient of drag.
C_L	Coefficient of lift.
F	Normal Reaction.
g	Acceleration of gravity.
H	Shape factor.
h	Height.

l Wheelbase.

m Mass.

N Force.

p Pressure.

p, q, r Angular velocity components.

R Tyre radius.

S Surface.

T Track width.

$\mathbf{V}$ Velocity vector.

u, v, w Velocity Cartesian components.

W Weight.

Subscripts

∞ Free-stream condition.

c Critical.

F Front axle related.

f Friction component.

i, j, k Computational indexes.

n Normal component.

R Rear axle related.

x, y, z Cartesian components.

Superscripts

* Displacement.

Chapter 1

Introduction

1.1 Motivation

Motorsports have always attracted the attention of many, from young people fueled by adrenaline, passing through curious enthusiasts that crave hands-on experiences, to some of the most strategic minds and best professionals in fields such as material science and mechanical engineering. In Europe, for instance, this reaches its apogee with Formula 1, where easily half of the population was aware that the last Grand Prix of 2021 would decide who would win the championship, Hamilton or Verstappen. A significant part of the budget of Formula 1 teams goes to the Research and Development (R&D) in aerodynamics because of the growth in importance given to increasing the downforce generated for greater cornering speed and decreasing the drag of the car to reach higher top-speed in straights.

Parallel to Formula 1 (F1), Formula Student is an open-wheel racing car competition where aerodynamics plays a significant role. Particularly concerning the Formula Student Team from Instituto Superior Técnico, FST Lisboa, although the increasing investment in aerodynamic studies of car components throughout the past years is noticeable, it is still lacking experimental validation. In this kind of racing competition, where each team creates a new prototype every year, the car is usually only built and ready to test on-track too close to competitions. An alternative validation tool can be wind tunnel testing, which, when combined with simulation software, can be very useful in the design phase of the car by providing more reliable results of the performance of the aerodynamic package and finally serve as a guide for future simulations.

The work that will be presented here is an extension of what has already been done by two colleagues of mine, Carreira [1] and Pacheco [2], who studied the car mostly focusing on track-tests and wind tunnel tests, respectively. Morgado [3], on the other hand, will work on the prototype at the same time as I am, but with a higher focus on reducing the drag produced by the rear wing which is the aerodynamic component where most of the drag is generated, whilst mine will revolve around assessing which components are underperforming and improving them.

Not only is this thesis focused on improving the aerodynamic capabilities of the car, but it also targets fulfilling the desires of the rest of the departments of the team, namely the Vehicle Dynamics team. In

an attempt to fill a lacuna by working together and using the tools developed by them, it will be possible to obtain milestones for the aerodynamic coefficients' values and distribution, which will help enhance the behavior of the car in terms of stability and drivability instead of just getting more grip while curving.

As a former member of the team, this is an opportunity to deepen the knowledge I have obtained and to give something back, as the whole process is developed in collaboration with the team and can serve as a starting point for future studies. Also, as an Aerospace Student, this is a remarkable way to get hands-on experience with the capabilities of wind tunnel testing, which would otherwise be unlikely.

1.2 Formula Student Competition

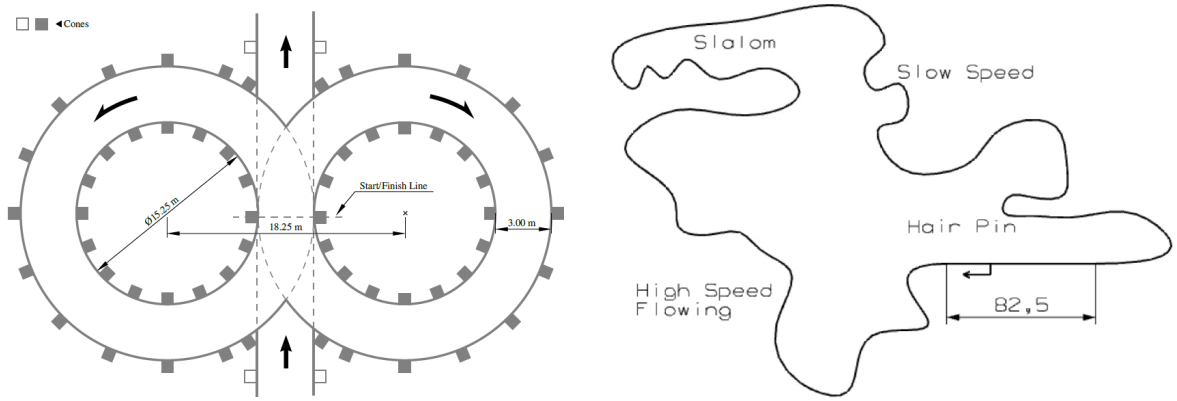

(a) Skidpad Track

(b) Generic Track [4]

Figure 1.1: Typical track designs

A Formula Student (FS) team's purpose is to build a car that will participate in one or more competitions. Given that, the main goal of the team is for the car to perform as well as possible in those. Each competition comprises seven events, divided into static or dynamic:

A) Static Events

- **Engineering Design:** where the engineering design and process of creation of the prototype is assessed;
- **Cost and Manufacturing:** evaluates the understanding of the costs involved in the whole process of designing and manufacturing the prototype;
- **Business Presentation Plan:** in this event, the profitability of the prototype is judged based on a business model built for a fictitious company.

B) Dynamic Events

- **Acceleration:** where the car has to accelerate through a 75m straight;
- **Skid Pad:** to test lateral acceleration, the car has to complete an 8-shaped track (fig. 1.1 a));
- **Autocross:** where one lap around the event's track (fig. 1.1 b)) is timed;

- **Endurance and Efficiency:** is the main event, consisting of a 22km race around the event's track. Additionally, energy consumption is also evaluated.

The most important effect of having an aerodynamic package on a Formula Student car is the higher allowable accelerations on braking, accelerating, and curving that are a result of the increased grip due to the downforce generated. Nevertheless, it is noteworthy that the addition of an aerodynamic package does not bring only advantages, as there is an increase in mass and drag. Given that, it is important to assess if the downforce increment benefit overcomes these disadvantages.

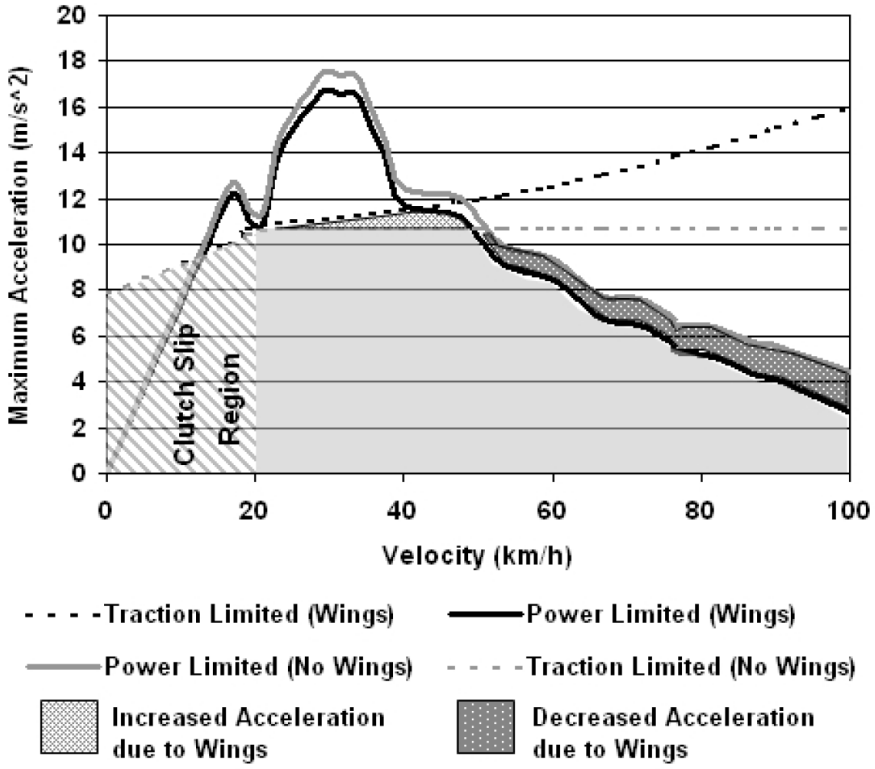

Figure 1.2: Power limited vs grip limited [5]

Wordley and Saunders [6] estimated that an FS car is traction limited (in terms of maximum acceleration achievable) until reaching 50km/h where it becomes power limited (fig 1.2). On an average FS track, the car is roughly 80% of the time below 50km/h, coming to the conclusion that it is traction limited most of the time and therefore that increasing traction by adding an aerodynamic package would be highly desired. However, their study was focused on a lap performance, only providing conclusions for the endurance and autocross events, so, to fully evaluate the necessity of aerodynamics on a Formula Student car, acceleration and skidpad events must also be assessed. On the acceleration event, it can be concluded that the best result would be achievable with a wingless car (i.e. without an aerodynamic package) due to the drag penalty that lowers the top speed and maximum acceleration (when grip ceases to be a restriction around 50km/h). Nevertheless, by reducing the incidence angle of the high-lift surfaces of the rear wing before the event (commonly known as Drag Reduction System, or DRS), the supra-cited penalty can be significantly decreased, especially because the rear wing is the main drag

contributor (refer to section 3.3). When it comes to the Skidpad event, the goal is to describe circular laps as fast as possible, being lateral acceleration the main driver. In order to potentiate it, higher levels of downforce must be generated. Summing up, it becomes clear that a correctly designed ”winged-car” should be advantageous in this kind of competition.

1.3 Previous Work

One of the two main precedents of my thesis is the work done by Carreira on [1]. He performed a mesh convergence and turbulence model study on the full-scale prototype and automated the process through the development of a macro that can be used to minimize input errors and time spent on the already time-consuming simulations. Other than that, he built a computer-aided design (CAD) model of the car where many parameters can be easily changed, namely rear and front ride heights, and steering angle. His main purpose was to obtain an aero map for the performance of the car for different values of ride heights in rolling, yawing, and steering which is important not only for the general overview of these parameters but also because it allows many different simulations in different flow conditions to be individually analyzed. Finally, through on-track testing, he managed to obtain trends that validate the computational fluid dynamics (CFD) simulations.

As well as Carreira, Pacheco also plays an important role as a predecessor of my work. In [2], he serves as a pillar for all future wind tunnel testing as he modeled the complete test section via CAD software that will be used together with the 6-bar balance ([7]), to measure the aerodynamic forces and moments. Besides that, he built the full baseline model of the car at a 1/3 scale with the static floor and appendices that can be used to vary the ride of the car and its attitude. He also perform a computational study of the 1/3 model of the car on different conditions (different ride heights, DRS) whose results were later used to compare with the experimental wind tunnel data to validate the numerical model through the trends observed.

It is also important to mention Morgado’s thesis ([3]), which was done at the same time as mine and with a common goal to improve the performance of the FS car via redesigning the aerodynamic package, resorting to computational and experimental methods. Whereas his thesis will revolve around reducing the rear wing’s drag, both our works are complementary and will be closely connected to the full behavior of the car in terms of handling and balance. As such, some parts of our works were done in cooperation and properly referenced when that is the case.

Although the open literature for motorsports can be quite scarce, which is no exceptioon for formula student teams, some previous works have been consulted and taken into account in the research stage of this work.

Wordley and Saunders [6] designs an aerodynamic package composed of a rear and front wing with the goal of producing maximum downforce. In he fully characterizes the necessities of a FS car based on the competition rules and studies the impact the design has on the competition performance. On a second paper, Wordley and Saunders [5] details the full procedure and results from the CFD, wind tunnel and on-track testing and development of the aforementioned aerodynamic package.

Craig and Passmore [4] presents a similar work where only the front and rear wings are concerned and in which a methodology to estimate the likely gains that having an aerodynamic package can bring to the competition scores is developed. The impact was considered sufficient to justify its inclusion.

A thorough study of the influence of the head restraint on the car's performance, both with and without side slip, can be found on Steinfurth et al. [8]. In this work, it was concluded that the installation of the head restraint causes a substantial decrease in the magnitude of downforce generated which consistently increases with its size (up to 5%. For small yaw angles, the impact of the size of the head restraint became less pronounced.

Outside FS environment, the works presented by Cooper et al. [9] and Ruhrmann and Zhang [10] are worth mentioning for this thesis as they both present assess the influence of undercar diffusers working in ground effect on the performance of the car, which will also be explored here.

1.4 Objectives

In the first stage, a detailed analysis of the aerodynamic behavior of the current prototype, which will result in an identification of critical regions (underperforming), is intended. Then, by adapting the current vehicle dynamics tool, which improves its capacity to predict the aerodynamic influence, the desired lift and drag coefficients will be obtained. By joining these values and the results of the aerodynamic analysis, an effort will be put into redesigning one or more of the underperforming regions identified and simulating them via CFD on an iterative process.

The improvements will be assessed and the best design will be chosen to be scaled, printed, and assembled to the current 1/3 scale model. After calibrating the force balance, the old and new models will be tested on the wind tunnel. The ultimate goal is to validate the enhancements verified on the CFD for the redesigned model on the wind tunnel.

This work will provide a thorough study of the optimization of the aerodynamics of an FS car, based on the modification of a component with a set specific goal rather than just reaching the highest achievable downforce and the experimental validation of it through wind tunnel testing. This should serve as a guide for future design phases. Along with that, there will be made available multiple simulations and experimental data that can be further analyzed.

1.5 Thesis Outline

This document is divided into 6 main chapters:

- **Chapter 1 - Introduction:** Where the main motivation is presented as well as an overview of the role of the aerodynamic package on a Formula Student car followed by a brief explanation of the rules and procedures of the competition. An introduction to the main predecessors of this work is performed as well as some conclusions from other FS aerodynamic studies.

- **Chapter 2 - Racing Car Aerodynamics:** This chapter serves as the pillar that sustains the work done by describing the aerodynamics behind a racing car and the methods that will be used to study and it, followed by the results and main conclusions of the studies that preceded this one, based on simulation, wind tunnel experiments and track tests;
- **Chapter 3 - Baseline Performance:** This chapter will start with a brief discussion of the setup parameters as well as of the models and will be followed by a study of the reference aerodynamic coefficients resorting to a vehicle dynamics tool. Finally, a detailed analysis of the aerodynamic behavior of the components of the baseline car and the identification of the underperforming regions.
- **Chapter 4 - Car Modifications:** The components to be modified will be chosen based on the goals set and the results obtained in the previous chapter. The new designs and some results for each will be presented. The process of choosing which modifications to implement is also discussed in this chapter;
- **Chapter 5 - Validation:** This chapter will feature the description of the manufacturing process of the new part as well as the calibration process and wind tunnel setup followed by the characterization of the impact of the wind tunnel limitations. The wind tunnel results will also be presented and discussed in this chapter.
- **Chapter 6 - Conclusion:** In this chapter, an assessment of the reached objectives will be made and future work on this matter will be proposed.

Chapter 2

Racing Car Aerodynamics

2.1 Vehicle Dynamics

In order to better understand how the flow around the car influences its performance, it is important to understand the main dynamics behind its typical behavior on a track.

The reference axis and physical quantities used throughout this work are illustrated in fig. 2.1. In addition, the rolling angle ϕ, pitch angle θ, and yaw angle ψ represent the angle variations around x, y, and z axis, respectively.

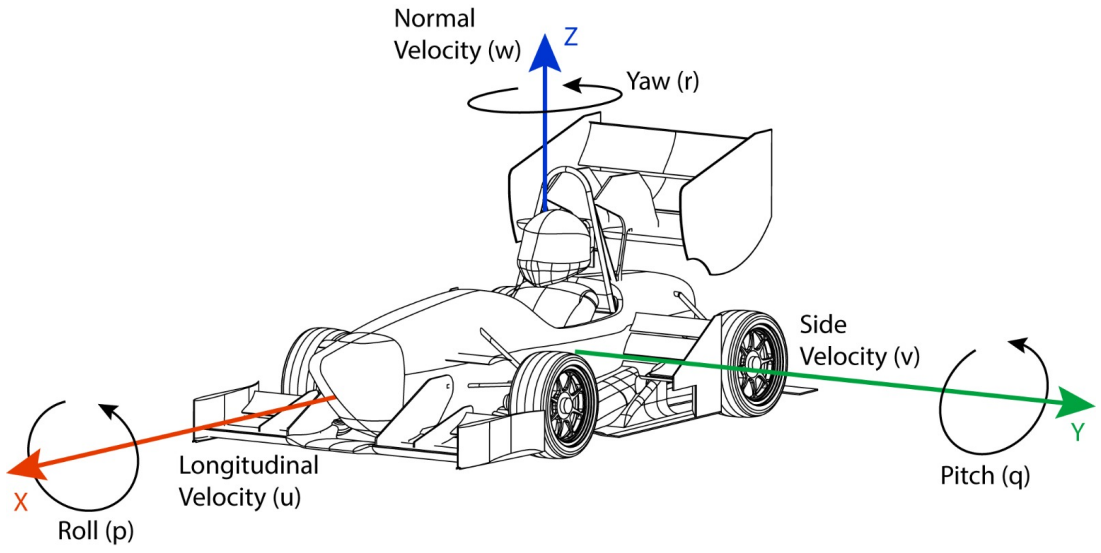

Figure 2.1: Car reference axis

Figure 2.2 represents a vehicle while describing a circular trajectory with a constant yawing ratio $\dot{\theta}$ and constant tangential speed $\mathbf{V}$. The sideslip angle of the car β is the angle between where the vehicle is heading and the traveling direction.

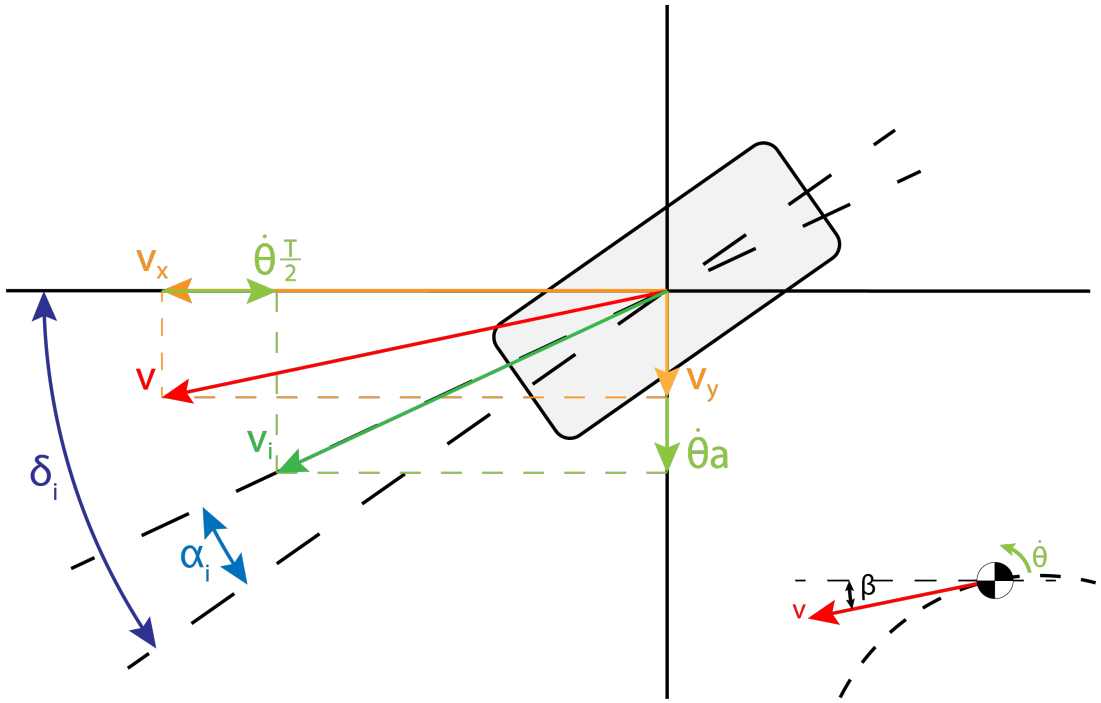

Figure 2.2: Geometric reference variables

Considering each tire individually: two angles are highlighted, the steering angle δ (for the front tires) which is the angle between the heading of the car and the heading of the tire; and the tire-slip angle α which, analogous to the car's slip angle, is the angle between the heading of the tire and its velocity V'. Additionally, T represents the track width and a the longitudinal distance between the tyre and the mass center (CG), where wheelbase $l = a + b$.

Because of the angular velocity r or $\dot{\theta}$, the velocity at the tires' frame will not be the same that the mass center senses, the front tires will be subjected to an increase in absolute side velocity while the rear wheels' absolute side velocity will decrease, considering the longitudinal velocity, the outside (related to the turning center) tires will see an increase and the inside tires will see a decrease. These velocity variations are as follows:

$$\Delta V_x = r\frac{T}{2}; \qquad \Delta V_y = ra \tag{2.1}$$

When the car is cornering, a lateral force is necessary to balance the centrifugal force appearing as a result of the circular motion, this lateral force comes from the contribution of each tire. When isolated, its sideslip, depending on the vertical force, will dictate how much lateral force is being generated. Figure 2.3 illustrates this relation and the impact of the vertical force. For example, to produce 150kg of side force, a more loaded car will not have to steer as much as a less loaded one.

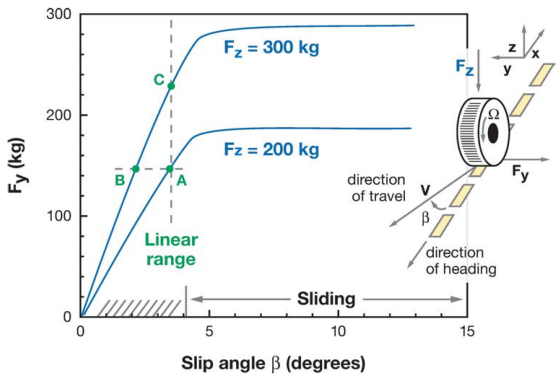

Figure 2.3: Tire sideslip plot [11]

As expected, the force necessary to brake or accelerate is also ultimately related to the tires, in particular, to the slip ratio, $ratio = \frac{\Omega R - V}{V}$ which represents the ratio between the speed of the surface of the tire (ΩR) and the speed of the tire (or the road). When the surface of the tire is faster, an accelerating force appears, whereas when the surface of the tire is slower a decelerating force is generated (in the case of braking). From a certain slip ratio, the tire will either spin or lock, for accelerating and braking phases respectively, for both cases, the force generated will tend to a constant value (that for the locked case will be the friction force $F_f = \mu_f N$), as illustrated in fig. 2.4. With higher braking and accelerating capabilities, the laptimes can be greatly increased as the car can decrease substantially the time spend reducing and increasing the speed before and after the corners.

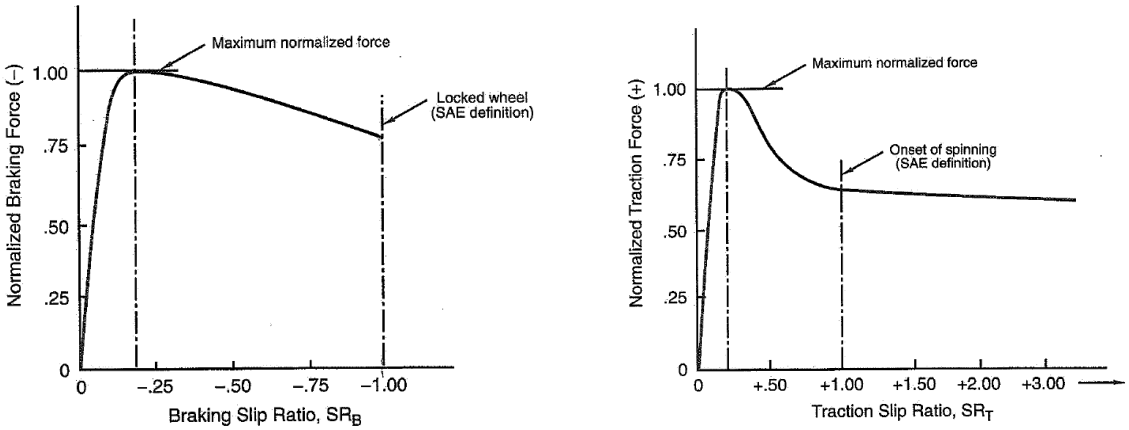

(a) Braking

(b) Acceleration

Figure 2.4: Longitudinal force as a function of slip ration [12]

It is noteworthy that, for most corners, the car is not purely turning, i.e. is also either accelerating or braking. When coupled, both the achievable lateral and longitudinal accelerations decrease. Figure 2.5 represents the achievable forces when both slip and sideslip are considered

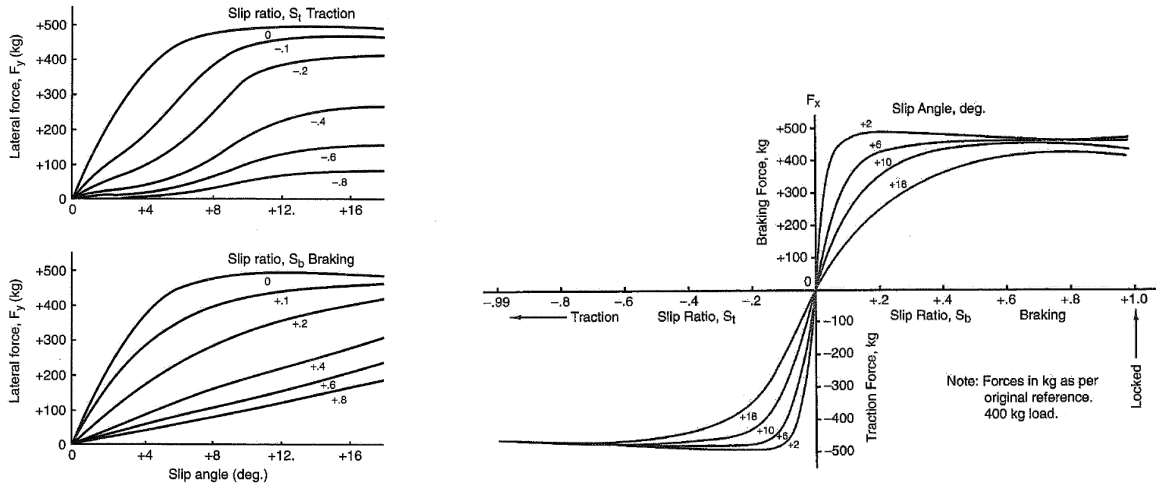

(a) Lateral force

(b) Longitudinal force

Figure 2.5: Available forces for a 400kgf load. [12]

As it has just been concluded, the achievable accelerations are dependent on the vertical forces on the tires and, ultimately, on its deformation. For a still car, these vertical loads come from a straightforward moment balance where each of the front and rear wheels will be subjected to $F_{zF} = W\frac{b}{l}$ and $F_{zR} = W\frac{a}{l}$, respectively, where $W = mg$ is the weight of the car. When a car is subjected to an acceleration (i.e. accelerating, braking, or cornering), the inertial force applied on the mass center has to be taken into consideration and, depending on if the acceleration is lateral or longitudinal, will cause a pitching or a rolling motion on the car. Due to this motion, a change in the vertical loads of the tires occurs, commonly known as weight transfer, as part of the load on a pair of tires is transferred to the other pair, as illustrated in fig. 2.6

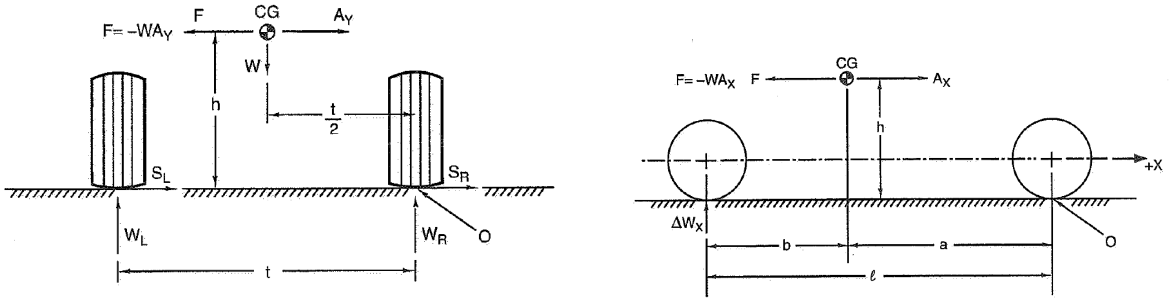

(a) Lateral

(b) Longitudinal

Figure 2.6: Weight transfer [12]

Being h the height of the gravity center, again from a moment balance, the vertical load transferred is given by:

$$LT = \frac{mah}{d}, \tag{2.2}$$

where d is the distance between the two tires in question. Considering the car reference axis in fig. 2.1

and dimensions presented in fig. 2.2, the total load on each tyre is summed up to

$$F_{Z_{i,j}} = DF_{i,j} + \frac{1}{2}W\frac{L-d_i}{l} + (-1)^i * \frac{ma_x h}{l} + (-1)^j * \frac{ma_y h}{T_i}, \tag{2.3}$$

where DF is the downforce, $i = 1$ for a wheel on the front axle, $i = 2$ for a wheel on the rear axle, $j = 1$ for a wheel on the right side and $j = 2$ for a wheel on the left side.

Another important factor in the performance of the car is the steering behavior, especially for stability and control. As illustrated in fig. 2.7, a car is said to be understeering if the lateral force produced on the rear axle surpasses what is produced on the front axle, creating a yawing moment opposite to the turn; this is usually desired when looking for stability (capacity of maintaining the steady-state when disturbed [13]). If an opposite moment is created, meaning that the lateral force of the rear axle is lower, the car has oversteer, which is usually preferred for control (response to inputs). The car is tuned and can be modified to tend more or less to under and over-steer. This modifications usually come down to the preference and driving style of the driver and the requirements of the track.

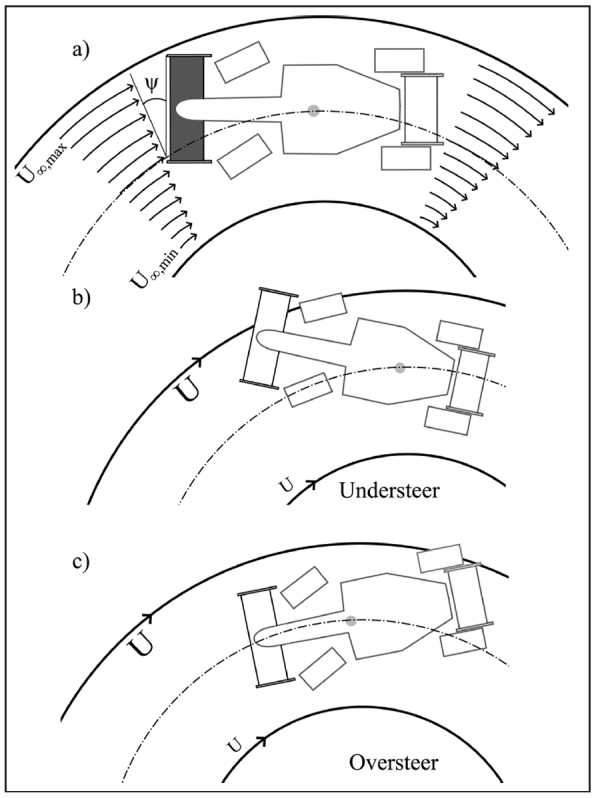

Figure 2.7: Understeer and oversteer [14]

As concluded, especially for cornering, the tires play a very important role. Although the main focus of this work is the capabilities of the aerodynamic package improving their efficiency, it is important to note that there are other geometry modifications that can be done that will also ultimately improve it. One example of that is the case of camber and toe and a comprehensive study on their influence can be found on [15].

2.2 Aerodynamics Phenomena and Effects

On this section, a brief introduction to the main aerodynamics phenomena will be given along with some racing car specific aerodynamic effects.

2.2.1 Pressure and Viscous Effects

Similar to airplanes, formula, cars make use of airfoil-shaped profiles to take advantage of the aerodynamic forces generated due to the relative airspeed around them. The physics behind it will not be presented as they are not the focus of this thesis but can be found in [16], [17] or [18]. For airfoil characteristics, refer to [19]. In macroscopic terms, change in momentum of the airflow passing over the car will change the pressure and viscous stresses distributions around it (fig. 2.8), which will produce a resultant aerodynamic force, applied on the pressure center, given by

$$\mathbf{F_R} = \oiint_S p\,\mathbf{n}\,\mathrm{d}S + \oiint_S \tau\,\mathrm{d}S. \tag{2.4}$$

Where S is the surface area of the car, p is the static pressure, τ is the shear stress on the surface and $\mathbf{n}$ is the unitary vector normal to the surface. When decomposed into two components, the drag and the side force are the horizontal components (pointing rearwards and sidewards) and the downforce is the vertical component (pointing downwards).

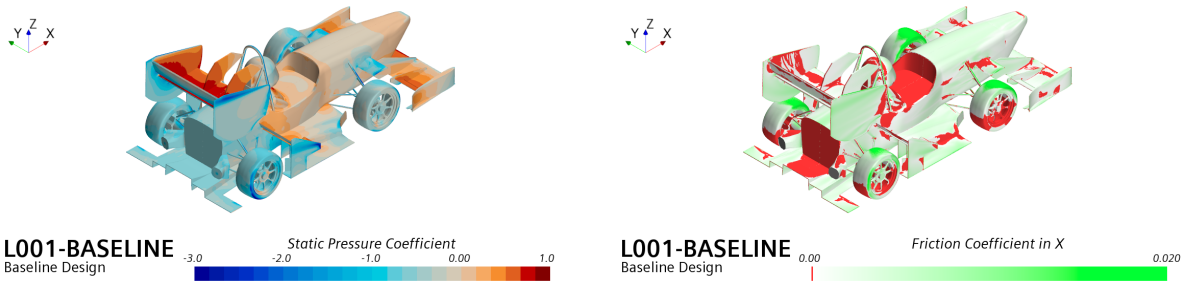

(a) Static Pressure

(b) Friction

Figure 2.8: Pressure distribution around FS car

Boundary Layer

The Boundary Layer (BL) is the thin layer of flow adjacent to the body surface where dissipative effects are included and its existence is a direct consequence of the viscosity of the fluid, which imposes a no-slip condition at the contact region (i.e. the speed of the air in contact with the airfoil - commonly referred to as wall - equals the speed of the surface). The BL is the region where the speed of the flow differs from the free stream, as illustrated in fig. 2.9. It can be laminar, in which the flow will be smooth and reassemble layers, or turbulent, marked by the presence of eddies and mixing of the previously mentioned layers, the intermittence of turbulence (refer to [20]) helps dictating the type of BL. The turbulent boundary layer is usually thicker and the curvature of its velocity profile is more pronounced, as fig. 2.9 (b) suggests.

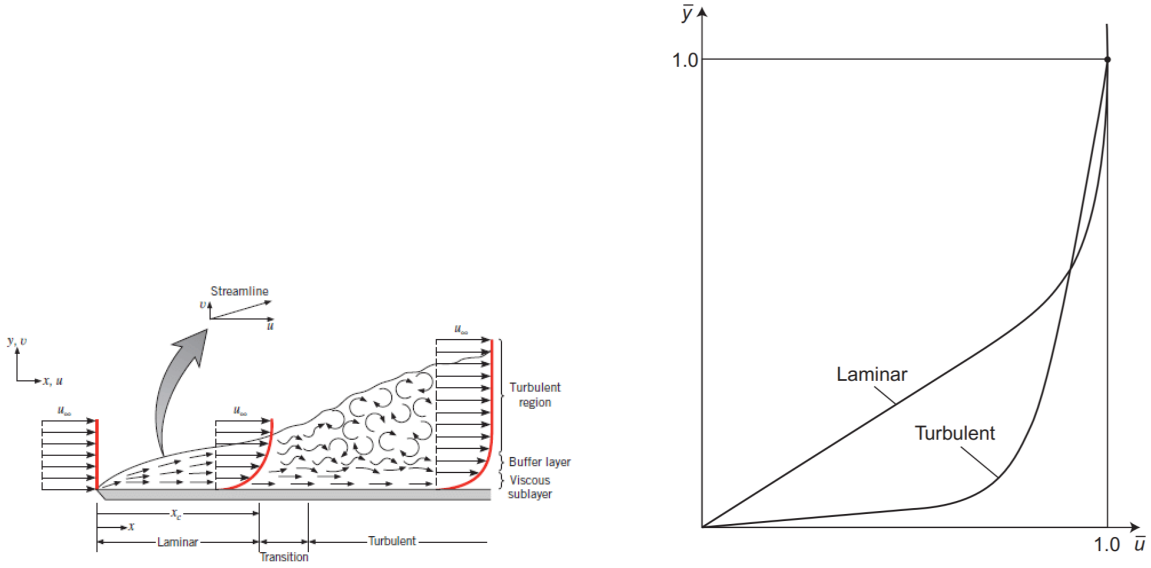

(a) Transition from laminar to turbulent BL on flat plate

(b) Velocity Profiles

Figure 2.9: Boundary Layers [21]

From the velocity profile, some quantities can be retrieved, starting by the boundary layer thickness δ, defined as the height normal to the surface at which $u = 0.99u_\infty$ ([22]), the displacement thickness δ^* (illustrated in fig. 2.10) that represent the distance that the surface would have to be displaced for an inviscid flow to have the same flow rate as the boundary layer flow. Analogously, momentum thickness θ can be defined as the distance which the surface must displaced so that, without BL, the total momentum is the same as that actually occurring [23]. Finally the shape factor $H = \frac{\delta^*}{\theta}$ which can sometimes be used to differentiate between turbulent and laminar flow (as turbulent flow have lower shape factors).

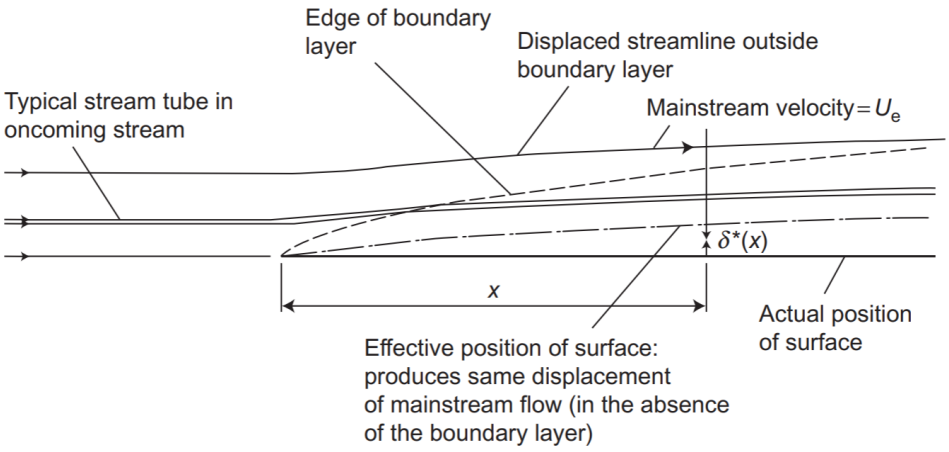

Figure 2.10: Displacement Thickness [12]

Separation

For slender bodies with thin BL, the pressure inside it equals the pressures outside on the direction

normal to the surface. In adverse pressure gradients ($\frac{\mathrm{d}p}{\mathrm{d}x} > 0$, x being the direction of the flow), the flow elements tend to retard inside the BL. For the near-wall layers, more remote from the free-stream, the effect of these pressure forces may surpass the diffusion. Separation occurs, when the velocity gradient at the wall is zero ($\frac{\mathrm{d}u}{\mathrm{d}y}|_{wall} = 0$), and is generally highly unwanted. If the inflection point strays from the wall, reversed flow (i.e fluid moving upwind) will be encountered in the inner regions of the BL. The severity of the separation depends on the reattachment of the boundary layer, and whether it happens close or far from the separation point. As the angle of attack increases, the adverse pressure on the suction side becomes more evident and thus more prone to separation, being the angle at which it starts to occur called critical angle α_c.

To satisfy continuity, the boundary layer thickens and the curvature of the streamlines changes, decreasing the lift generated. Another direct consequence of the separation is the increase in the thickness of the wake and reduction in pressure rise which will, in turn, increase the drag of the profile. Due to the interchange in momentum inside a turbulent boundary layer (increase in diffusion), it is much harder for separation to occur than on a laminar boundary layer. That is why some aerodynamic surfaces like wings have devices that promote transition even at the cost of increasing the skin-friction drag (as this type of friction is proportional to the shear stress τ_w at the wall).

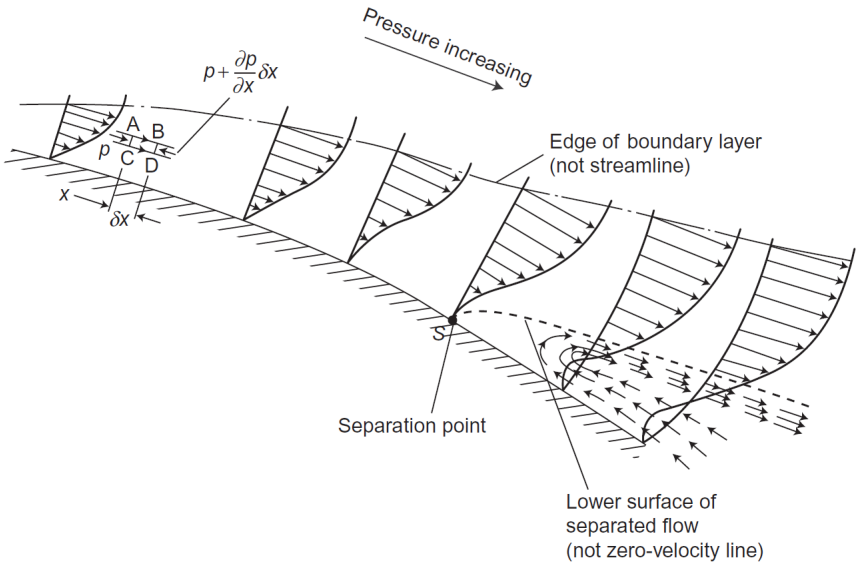

Figure 2.11: Flow separation under adverse pressure gradient [23]

2.2.2 Performance Related Effects

Grip contribution

As it was previously referred to, higher normal forces allow higher accelerations, commonly referred to as ”more grip”, and that is where downforce plays an important role. In addition, its distribution through the vehicle will influence the handling and stability of the vehicle, i.e. the consequence of having the pressure center behind the center of mass is that the additional grip will be more pronounced on the

rear wheels than on the front wheels. This will increase its stability while cornering by giving the car a more understeering behavior. Whilst this might be preferable for most cases, it is not a one-size-fits-all strategy and should be adjusted based on the driver's preferences and track configuration. Usually, there is a tendency to keep the pressure center as close to the mass center as possible so that the driver does not sense significant changes in the handling when reaching higher speeds [24]. It is noteworthy that both slip angles and slip ratios increase tire wear and heating.

Ground effect

Ground effect consists of making use of the proximity to the ground to enhance aerodynamic capabilities. It was first introduced in aircrafts to reduce the induced drag by interrupting the wingtip vortices. The same principle can be applied to an inverted airfoil where a significant downforce can be obtained by further reducing the pressure by constricting the flow. Similar to what happens in a Venturi tube, when the section area under the car reduces, to maintain the mass flow, velocity must increase, consequently. From potential flow theory, constrained convexly curved streamlines will reduce even further the static pressure under the wing, enforcing the effect of the ground on the aerodynamic performance. Of course it does not work exactly as Venturi as for this case it is an open system, but up to a certain extent, a parallel can be drawn. Surprisingly, only in the late 70s was this concept introduced in motorsports and it was immediately a game-changer (McBeath [25]).

As investigated in [26] and [27], the values of the downforce and the suction peak increase with proximity to the ground until a certain limit (fig 2.12), from where a significant reversion of tendency can be observed. At this point, the gap is so thin that viscous effects become significant and the boundary layers of the airfoil and ground merge throttling the airflow. Additionally, it has been concluded that this downforce reducing phenomenon occurs at higher ground clearances (h) the more cambered the profile is. Concerning drag, it increases monotonically with decreasing height [28]. Toet and Zhang on [29] review and summarize several studies on ground effect of different car elements and their main conclusions.

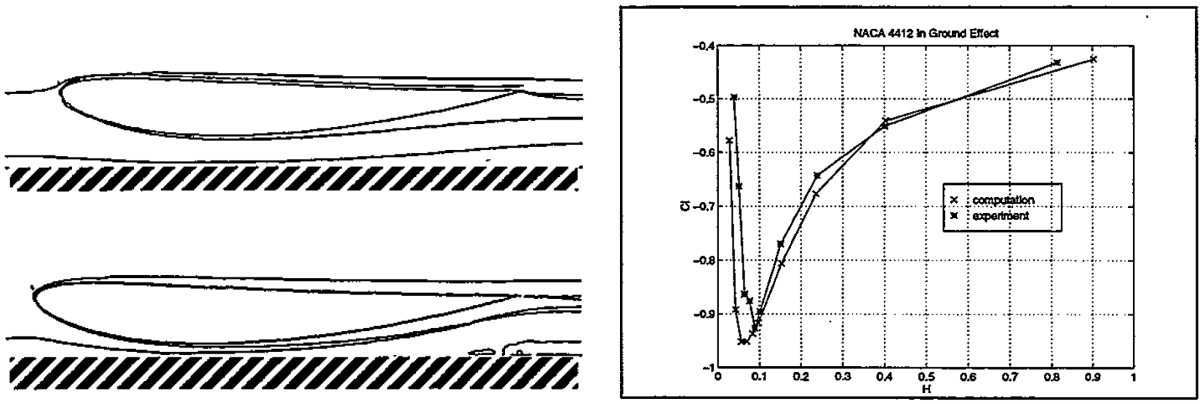

(a) Boundary layers in ground effect [28]

(b) Lift coefficient vs ground clearance [28]

Figure 2.12: Ground effect

Vortex and Vortex Breakdown

Green [30] defines vortex, in a non-rigorous way, as a "region of concentrated vorticity", as an attempt

to deal with its imprecise nature, where vorticity $\vec{\omega}$ of a velocity flowfield $\vec{u}$ is defined by the expression:

$$\vec{\omega} = \nabla \times \vec{u}.$$

Vortex Structures are usually found on separated flows (in the form of vortex shedding) or in the form of streamwise vortices. Separation is highly undesired in aerodynamics, therefore, the focus should be directed to the latter. One example of such could be the wingtip vortex that is easily recognizable and is caused by rotational airflow that is driven by the pressure gradient between the suction and pressure sides of the wing. The upwash generated will add a drag component known as lift-induced drag $C_{d_i} = \frac{C_L^2}{\pi ARe}$. Although at first these characteristics might look only detrimental, vortices gained attention in the 90s ([31]) as a means of increasing downforce resourcing to its core low pressure (under the car, for example), or by using it to divert (in front of the tires) or seal the flow (so that a region of low pressure is maintained). Fig. 2.13 presents an example of the generate vortices on a F1 car.

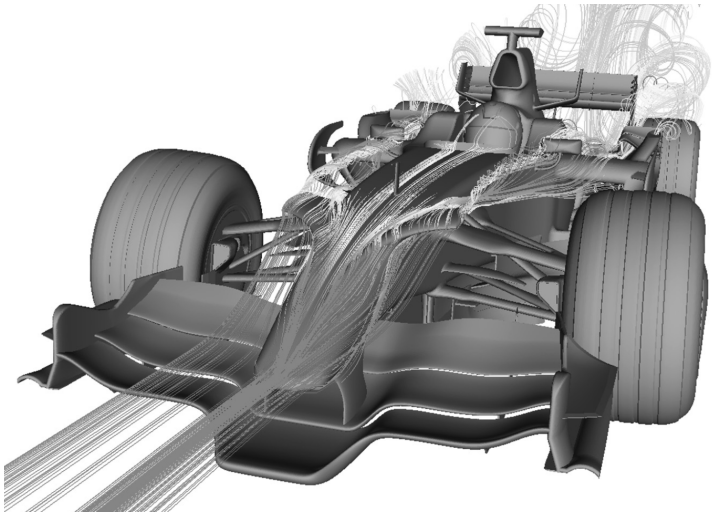

Figure 2.13: Vortex visualization in F1 car [29]

If it is true that a stable and controlled vortex can cause a positive effect on performance, it is also true that an abrupt change in its structure, commonly referred to as vortex breakdown, can be highly damaging as the vortex stops serving its purpose and disturbs the flow downwind, in most cases creating significant wake regions. Given its sensitivity to disturbances, these structural changes are common but quite unpredictable and are not as well documented in open literature as other aerodynamic phenomena. Leibovich [32] characterizes breakdowns as an internal stagnation point accompanied by reverse axial flow in the core of the vortex and they appear predominantly in two types, bubble-like or spiral (fig 2.14).

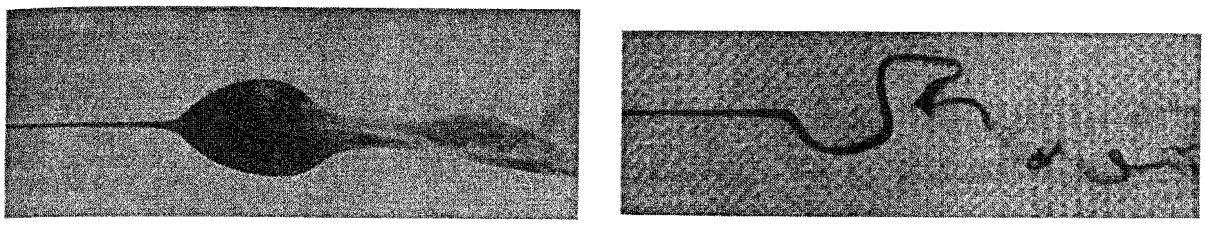

(a) Bubble (b) Spiral

Figure 2.14: Vortex breakdown types [33]

On the previous two sections, the main dynamic and aerodynamic phenomena related to the car were introduced. Given that they serve as pillars on its performance analysis, not only separated but also coupled, increasing the complexity, the understanding of the these concepts is deemed necessary.

2.3 Main Aerodynamic Appendages

Before describing all the parts and appendages that make part of the aerodynamic package, the Formula Student design limitations presented in fig 2.15 show the regions where they can be added.

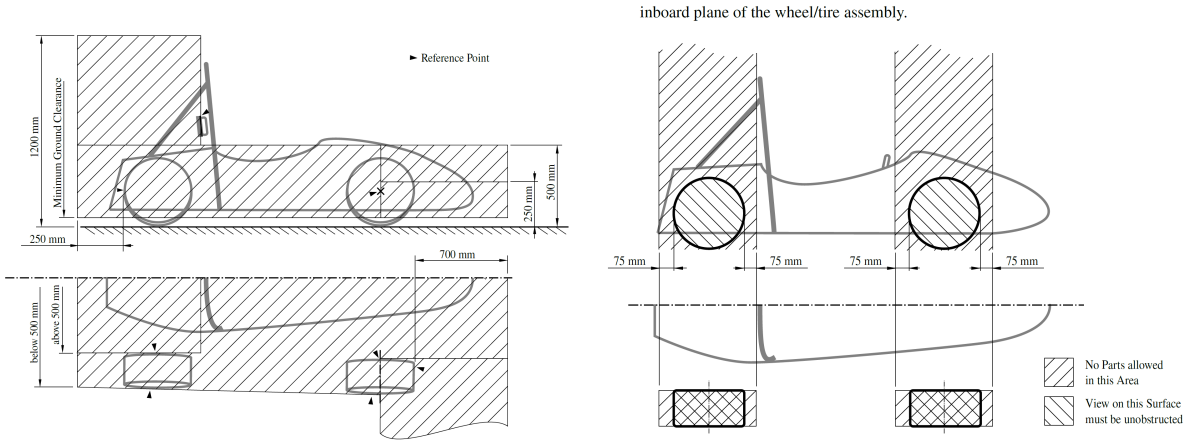

Figure 2.15: Design boxes [34]

As it can be drawn, the regulations of the FS competition permit significant changes between cars, allowing creativity and diversity in the aerodynamic design.

2.3.1 Wings

(a) FS front wing example (elephant racing)

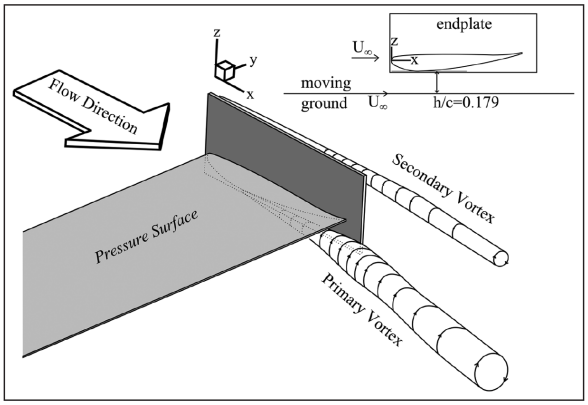

(b) FW vortex representation [35]

Figure 2.16: Front wing

Front Wing (FW)

The front wing (fig. 2.16) is the aerodynamic component that contacts first with the upcoming flow so it is in a privileged position as the air is a lot less disturbed than at any other part. Taking advantage of the ground effect, given its low position, the front wing is responsible for generating a significant part of the total downforce, with a relatively low drag penalty.This downforce will balance the distribution so better handling can be achieved and is essential to grant grip on the front axle. The front wing is also responsible for ensuring that enough flow is directed downward to the underbody to make it efficient. So, since high loads induce upwash, limiting the amount of flow that could go under the car, the front wing is usually more loaded on the sides (in front of the wheels) than on the middle [11].

Depending on the design decisions, the front wing might also be used to divert the flow from the tires minimizing the wake behind them [36], or to create specific vortexes to limit or control the flow downwind.

It is noteworthy that the front wing's performance will affect (and at a smaller scale be affected by) the behavior of the flow around the rest of the vehicle, meaning that an increase in its downforce does not necessarily mean an increase in total downforce[37].

(a) FS exemplar

(b) F1 exemplar

Figure 2.17: Rear wing examples

Rear Wing (RW)

The presence of a rear wing is usually how one can distinguish right away a sports car from a common one and, when compared to the front wing, the airflow that reaches the rear wing is a lot more disturbed and less energetic, leading to less predictable behavior.

The rear wing is generally composed of a variable number of elements (the FST10 prototype has 3 elements - one main wing and two high lift surfaces) and its main purpose is to generate high levels of downforce. In order for that to happen, there will be a low-pressure region below and behind the wing that will, on one hand, enhance the functioning of the underbody [] and laterally deflect the flow inwards [38] (suction) and, on the other hand, increase the drag of the car, being the main drag contributor, limiting its top speed. One way to mitigate this penalty when high downforce is not required (in straights, for example) is by changing the incidence angle of the more inclined elements so they are more streamlined, usually referred to as Drag Reduction System (DRS)(fig. 2.18). This can be done actively, like in F1 races, where the pilot activates the DRS when he is close to the car in front of him (less than 1s) and wants to overtake, or passively, like it is now done by the team, configuring the incidence angles based on the type of event. It is noteworthy that this change will alter significantly the pressure distribution of the car and the handling, as a consequence.

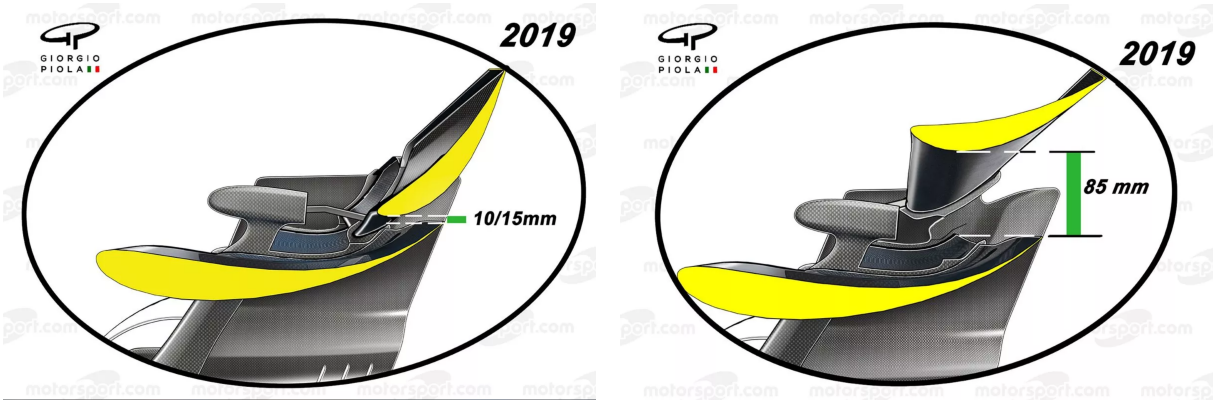

(a) Inactive (b) Active

Figure 2.18: Drag Reduction System [39]

There are two smaller appendages that are usually present in formula student cars, the **bull horn** and the **gurney flap:**

The bull horn (BH), unlike all the previously presented profiles, (fig **??**) is not composed of an inverted airfoil. At first thought it looks incoherent, why would a lift generating surface be added to a car in which one of the main aerodynamic design purposes is to produce exactly the opposite force? Well, as it was presented previously, the aerodynamics of a formula-type car go beyond the forces produced and have to deal with many effects and interactions. The bull horn, in particular, is added to generate a wing-tip vortex that will, at first instance, pull clean air from the outside and push away the dirty-air that comes from the tire and its interaction with the front wing flow. Downwind, the vortex trail will have another important effect when it reaches the rear wing since the bull horn tip vortex and the rear wing tip vortex have opposite vorticities, it will attenuate the impact of the latter one, increasing the effective angle of

attack of the rear wing flaps (by decreasing the local upwash), and decreasing the wake drag.

Especially but not exclusively on the rear wing, is commonly noticeable the addition of a small, thin perpendicular tab at the trailing edge of the last flap. This kind of device is known as a **gurney flap (fig 2.19)** and, through the generation of small vortices fore and aft of the tab [31] not only promotes the reattachment of the separated trailing edge but also changes the curvature of the streamlines creating an effect similar to increasing the camber of the profile that will, ultimately, result in higher lift [40].

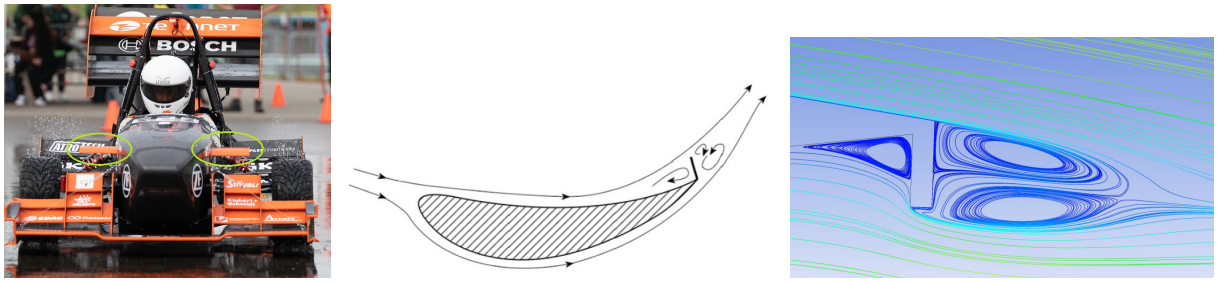

(a) Front view of FS car with BH (b) Wing with Gurney flap (c) Close-up of gurney vortices [41]

Figure 2.19: Bullhorn and Gurney flap

End Plates (EP)

The aforementioned wing-tip vortex, in its full extent, and especially at the rear wing, is undesired. To mitigate it, a flat or profiled plate, usually know as endplate, can be added to the side of the wing. By attenuating the intensity of the vortex, the effective angle of attack increases, enhancing the generated downforce, and the drag caused by the low-pressure rotational flow downwind reduces. It can also serve as a barrier to prevent the tire wake to reach the rear wing.

Figure 2.20 (a) presents an example of the increments in drag and downforce due to the addition of endplates on a rear wing, and shows that, for low angle of attacks, the efficiency (L/D) of the wing increases.

Although it can be found in most wings, front and rear wing endplates are significantly more complex and should be subjected to special attention. In the case of the front wing, one determinant factor is the position of the endplate (directly linked to the wingspan). As reported in [38], when the endplate of the front wing is closer the inner section of the wheel, the wing-tip vortex is directed inside and, by increasing the angle of attack (AoA), it might reach the rear wing and substantially spoil the downforce. On the other hand, having a wider front wing not only potentiates the downforce generated (as there is more area available) but also makes use of the position of the endplate to divert the flow outside of the front tires as a means of decreasing wheel drag. To further enhance this effect, these endplates are usually profiled shaped, creating additional side-wash downwind.

As the flow passing through the rear wing will not contact any other aerodynamic device, given its position, its endplates are designed mainly to reduce the intensity of the vortices. Although the basic flat plates alone fulfill that purpose, modifications can be made, such as the addition of louvers to further attenuate the wing-tip vortex's impact. Louvers (seen on fig. 2.20 (b)) are small lofted gaps that work by creating a stream that comes from the high-pressure region above the wing to the lower-pressure region outside the rear wing, creating a vortex that rotates in the opposite direction, therefore reducing

its intensity.

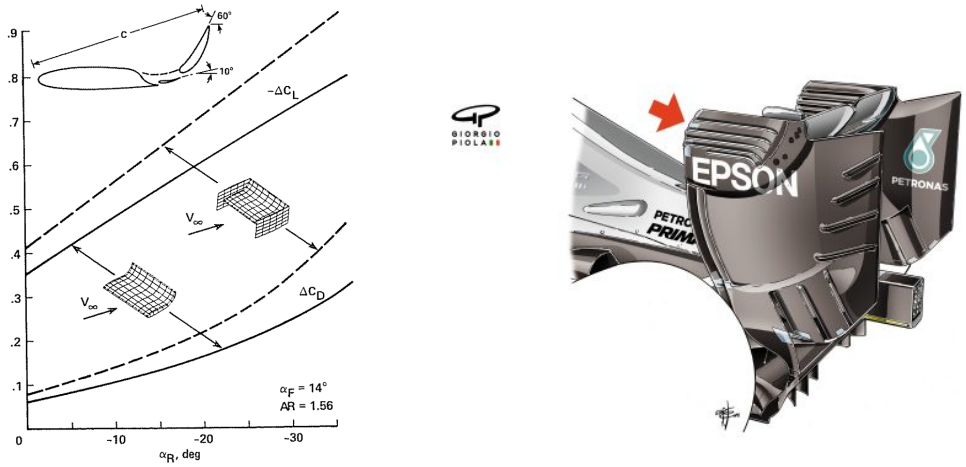

(a) Force increments due to EP [42]

(b) RW with louvers

Figure 2.20: Endplates characteristics

2.3.2 Undertray

The undertray (or underbody) consists of the large area under the car that is closer to the ground (fig. 2.21). Depending on the regulations and design decisions of the team, it is usually the most efficient aerodynamic part of the car, responsible for up to half of the total generated downforce, while having a low contribution to the total drag, taking advantage of the ground effect. It comprises the intake, which should be sized in accordance with the intended mass flow, that accelerates the flow in a favorable pressure gradient until a transition low-pressure zone. The last region is the diffuser, which will grant a gradual transition to the slower freestream while ensuring that the suction region upwind is maintained.

The performance of the diffuser is measured by its pressure recovery [43] and it is influenced by many factors such as inlet and outlet areas, ramp angles [10], and flow conditions. Thanks to two main effects - upsweeping, which works similarly to the camber on an airfoil, and pumping, as means of a suction peak at the inlet of the diffuser, coupled with the ground effect they are subjected to, the diffuser becomes a key player in the production of downforce [9].

As it works in adverse pressure gradients, it is prone to separation, so there must be and increased effort to avoid it. Amongst other ways of doing so, it can be done by adding a small flap close to and above the outlet [25], adding another diffuser stage, or by active methods like blowing (to reenergize the flow) or sucking (to extract the low energy BL flow).

It is worth mentioning that usually, above the lateral diffusers are placed the side pods, where most of the cooling air is captured, being that capture its main purpose. Nevertheless, they are also designed to avoid separations on the side of the car and increase the its aerodynamic performance.

Another characteristic of the underbody that has an influence on the airflow is the rake angle (fig 2.21 b)), which is the angle between the undertray and the horizontal. Higher rake cars allow for more air volume under the car at the same time that facilitates the diffuser job. However, low rake cars can take more advantage of the ground effect and tend to have fewer drag penalties.

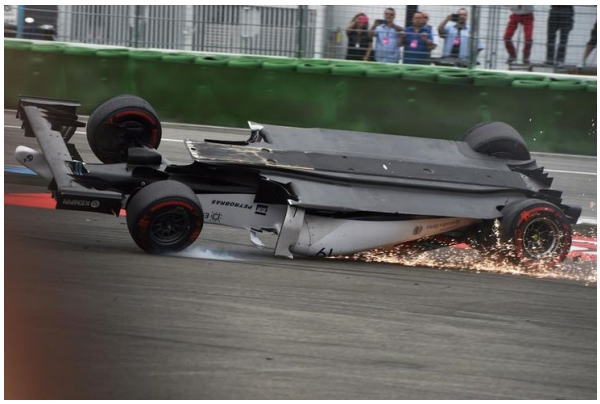

(a) Undertray example

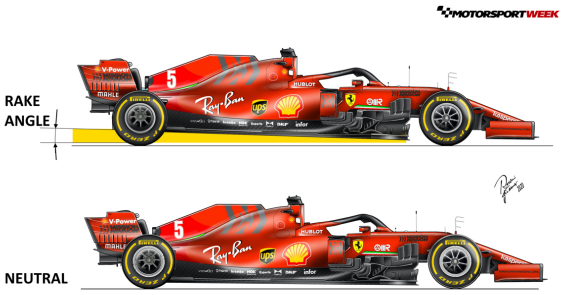

(b) Rake Angle

Figure 2.21: Underbody visualization

Vortex Generators

Alongside endplates, vortex generators (VGs) are also a resource intended to maximize the aerodynamic capabilities of a specific device. They are responsible for creating streamwise vortices that might serve multiple purposes. Garcia and Katz [44] present a full report on the impact that the inclusion of VGs can have (fig. 2.22 (a)) and which variation of parameters (number of plates, the distance between them, VG angle, and the angle between consecutive VGs) returns the best results. The main conclusions being that outside directed VGs (the inner inclined 30 degrees and the outter 40 degrees) delivers the most downforce. They also observed that a detrimental roll-up phenomenon between the vortices (fig. 2.22 (b)) can be avoidable by reducing ground clearance. Besides that, VGs are used across multiple aerodynamic applications, from aircraft wings to wind turbines, to control separation by promoting the interchange of momentum between the BL flow and the freestream flow. Kuya et al. [45] performed an extensive study on the capacity of a VG to mitigate separation on a wing in high adverse pressure gradient, different types of VGs were analyzed, from symmetric to parallel and with different heights (sub boundary layer or above).

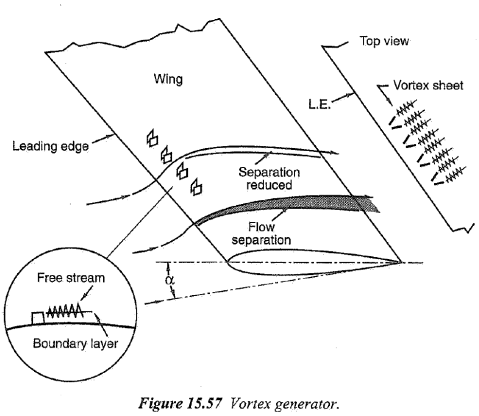

Figure 15.57 Vortex generator.

(a) Wing vortex generators [44]

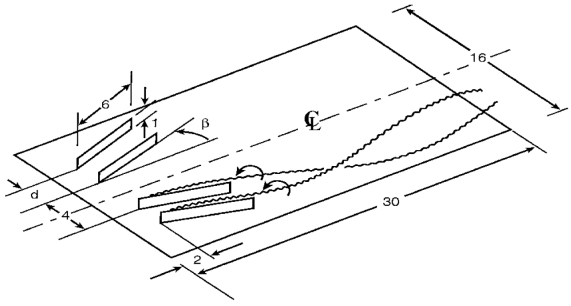

(b) Vortex roll-up [11]

Figure 2.22: Vortex generators

As there is still a significant region far from the ground and between the two axles, the airflow there

can still play key roles, from generating extra downforce, to diverting flow from the rear wing or enhancing the performance of other aerodynamic elements. In fig. 2.23, two examples of such devices are presented:

Figure 2.23: Example of FS car with side wing and side cascade

2.3.3 Component Breakdown of Aerodynamic Performance

Finally, as a formula car is a very complex body, all these effects must be analyzed in terms of overall impact but also in respect to each component and the interactions between them. In fig. 2.24, an example of the pressure distribution below the car is presented and an example of the influence of the addition of each component is assessed, again verifying the non-linearity and coupling of components.

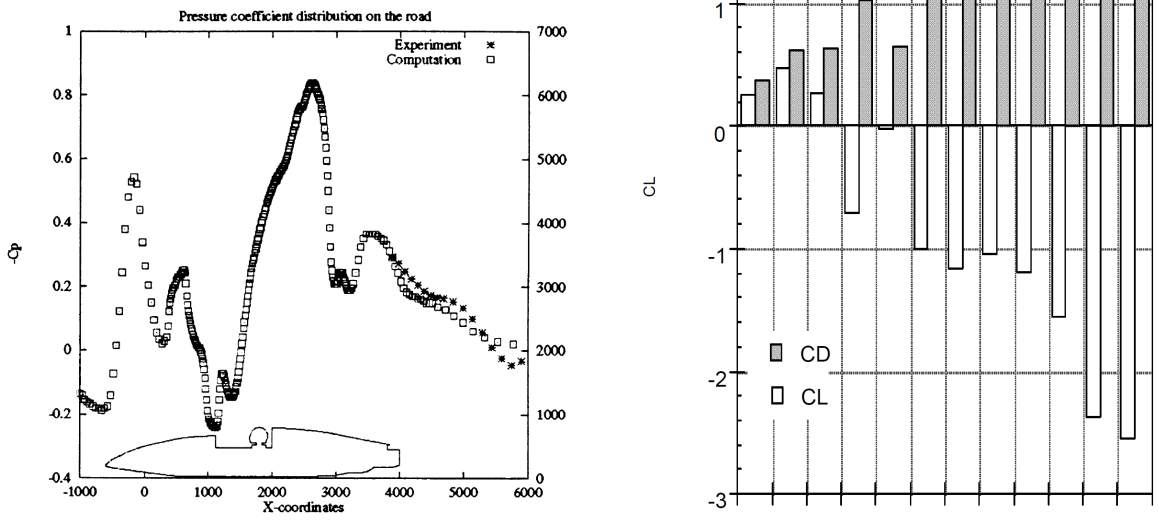

(a) C_p Distribution

(b) Car Components C_L Variation

Figure 2.24: Pressure Variation [40]

2.4 Aerodynamic Study Tools

The results that will be presented in this thesis come essentially from the aerodynamic analysis of computational fluid dynamics simulations and subsequent validation resorting to wind tunnel facilities.

2.4.1 Computational Simulations

Computational fluid dynamics (CFD) comes as an extremely powerful tool to predict the behavior of the airflow surrounding the car without the associated costs of running track tests or the necessity to build models to retrieve data from wind tunnels, and, as so, it plays a key role in the design phase. CFD resorts to the Navier-Stokes (NS) equations, which are a set of partial differential equations used to describe the behaviour of a moving viscous fluid and how velocity pressure and density are related to one another. Due to its high complexity and non-linearity, it is extremely difficult to resolve them analytically, and based on how turbulence is addressed, there are three main types of simulations.

Direct Numerical Simulation (DNS) solves the NS equations for all temporal and spacial scales and as a result, retrieves the most reliable solutions. Nevertheless is extremely expensive either in time matters and computational requirements and so it is only applied to simple geometries and, at least for now, is out of the question for car simulations. In terms of complexity.

Bellow DNS stands Large Eddy Simulation (LES), in which the small eddies are modeled and large eddies, where most of the turbulent kinetic energy (TKE) is stored, are numerically solved. As it presents a better compromise between computational costs and reliability of the results, it has seen increased usage in car applications.

Finally, the vast majority of simulations are based on Reynolds Averaged Navier-Stokes (RANS) equations, first proposed by Reynolds [46], in which the flow quantities are decomposed into an average component and a fluctuating component. To compute the velocity fluctuations, it resorts to a turbulence model. This is, therefore, the less accurate out of the three, but composes a good compromise between computational effort and accuracy for many aerodynamics applications, like the one presented on this work. Fig. 2.25 displays a visual comparison among this types of simulations.

As the flow is highly turbulent, the choice of the right turbulence model is of utmost importance (except for DNS). Two-equation based models such as $k-\omega$ described in [47] and $k-\epsilon$ can be used in different applications as the first captures well the essence of the boundary layer flows and the latter works better with flow outside the boundary layer (while $k-\omega$ tends to overestimate the turbulence on that region). In an attempt to combine the best properties of both models while introducing some variations, Menter [48] described two new models: Base-line (BSL) and Shear-Stress Transport (SST) that proved to be reliable in solving turbulent flows.

The computational phase of the design consists of multiple stages. In order to capture the whole essence of the flow, particularly smaller phenomena that can impact the flow, a grid study should be performed, having into consideration that the more elements a grid contain, the higher computational cost it will carry. For a better compromise, local refinements should be performed, for example in regions subjected to strong adverse pressure gradient . Another factor that should be addressed is the definition

of boundary conditions such as rolling surfaces or velocity inlets in an attempt to remain as close to real conditions as possible.

The chosen models and boundary conditions used for the simulations throughout this work are presented on Sec. 3.1.

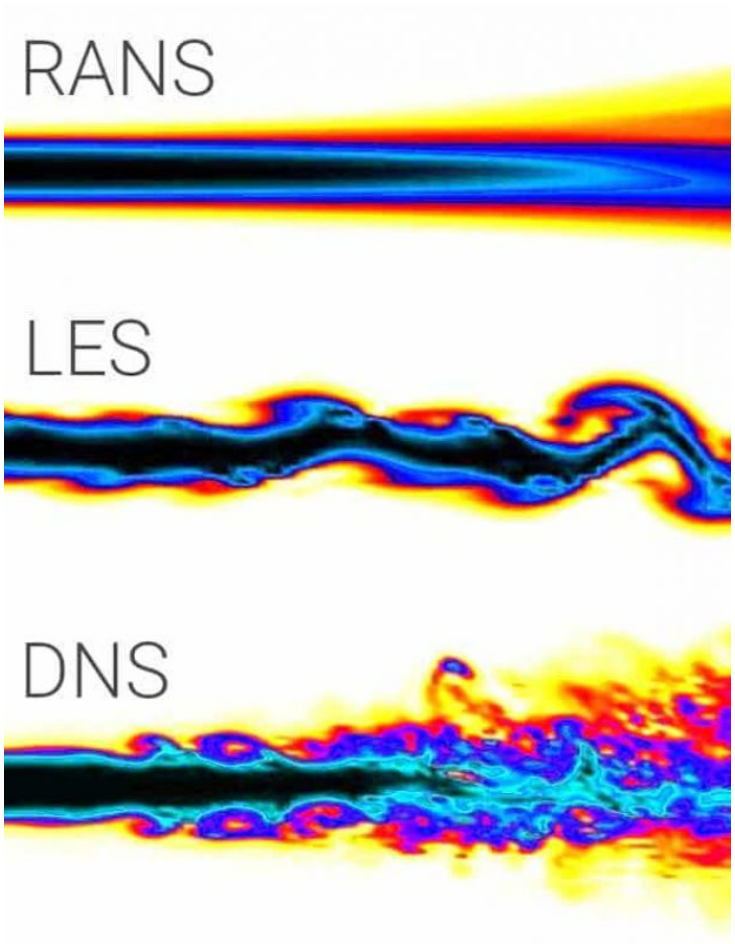

Figure 2.25: CFD modelling of turbulent jet [49]

2.4.2 Experimental Testing

Although being an excellent tool and allowing the materialization of multiple ideas that would otherwise be unfeasible, the reliability of computational simulations is greatly increased upon validation of the models, wind tunnel testing comes as a wise investment for this matter.

Wind tunnels allow the controlled simulation of real-world conditions and, by using a scaled model to evaluate if the behavior is similar to what was predicted by the software, the reliability of the software can be assessed and the confidence in future simulations can be greatly increased.

Wind tunnels may be found in many different configurations, but can be classified as open or closed, both regarding the wind tunnel type and the test section.

Regarding the data collection, there are three main types, measurement of pressure through the utilization of pressure taps on critical regions, measurement of forces and moments by means of a force balance, and flow visualization through special paints (flowviz) or wool tufts (fig. 2.26).

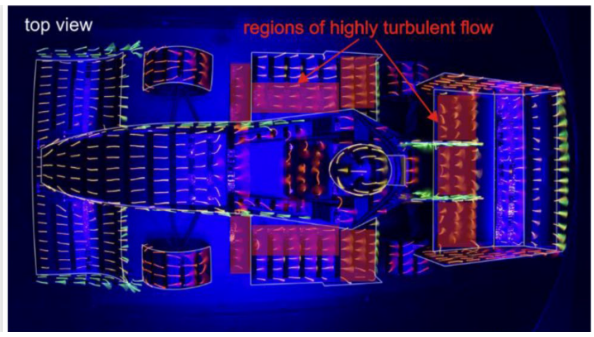

Figure 2.26: UV Wool Tufts [8]

When compared to race-track tests in the fully finished or semi-finished car, model tests on wind tunnels have the advantage of being significantly less expensive and require fewer logistics, as there is no need to book track time and car transportation. Wind tunnel testing is generally used in the design phase in order to allow for the change of unpredicted low performing regions or the complete change of the aerodynamic package while race-track testing is the final phase before competitions where there is still room for fine-tuning or some small adjustments but no major modifications should be made.

(a) Wind tunnel IST (before closing test section)

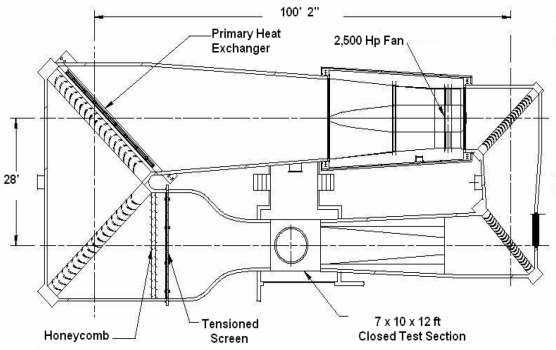

(b) Generic Plant [22]

Figure 2.27: Wind tunnel examples

On sec. 3.1 the setup and models that was used for the CFD simulations regarding this work is presented. Later, on sec. 5.1, the whole procedures done for the calibration and testing on the wind tunnel is described, along with the main limitations encountered.

2.5 Available Results

Before exploring the progresses of this work, it is important to assess previous results and methods used on Pacheco [2] and Carreira [1], as some of them will be used throughout this thesis and, as aforementioned, this work is, on some extent, an extension of what will be presented next.

2.5.1 Wind Tunnel Test and Validation

Pacheco [2] divided his work into multiple parts. He first modeled, through computer-aided design (CAD) software, the full test section of the wind tunnel along with the car's scaled model and support infrastructure. Together with a characterization of the jet flow in terms of the velocity profile on several sections and turbulence intensity, it allows for computational simulations to better represent what will then be tested on the wind tunnel. A full testing methodology (fig. 2.28) which takes into account many variables (i.e. temperature, erratic measurements, wind tunnel procedures) was also elaborated, this composed a great starting point for the testing methodology used on this work and helped to avoid repeating the same mistakes.

In addition, the complete 1/3 scaled model of the FST10 prototype was built by resorting to 3D printing and computer numerical control (CNC) machining. Finally, a macro intended to accelerate the simulation process without the need for UI inputs was developed after a mesh refinement study was performed.

Wind tunnel tests of the model and equivalent computational simulations allow the assessment of the validity of the simulation results, which was the ultimate goal of his work. This assessment was done by comparing forces measured on a 6 DoF balance and the forces reported on the CFD software as well as comparing the airflow visualization by bounding wool tufts on the surface of the car and post-processed images of the simulations. Five different configurations were tested, the baseline in three different heights and the low-drag configuration, where the rear wing flaps are aligned with the flow, and another with a small device in front of the rear wing that represents a LiDAR sensor. All of them were tested at three different speeds (15, 20, and 25 ms^{-1}) From the airflow comparisons, the front and rear wings presented the most discrepancies, mostly due to separated regions that were captured on the simulations that were not present in the wind tunnel testing (fig. 2.29), this can be related to the length of the wool tufts, making them unable to capture small scale phenomena.

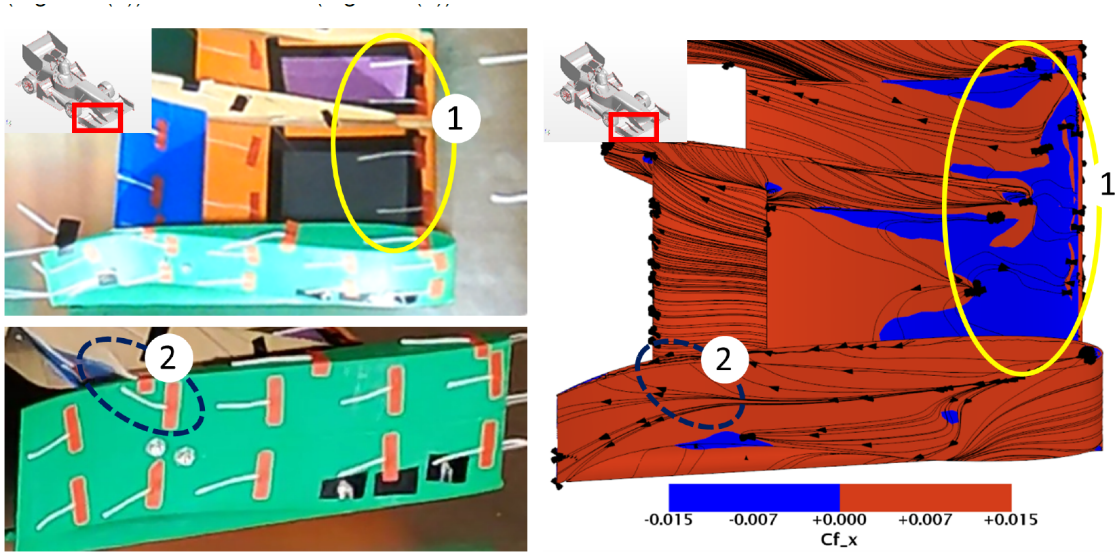

Figure 2.29: Comparison between CFD and WT

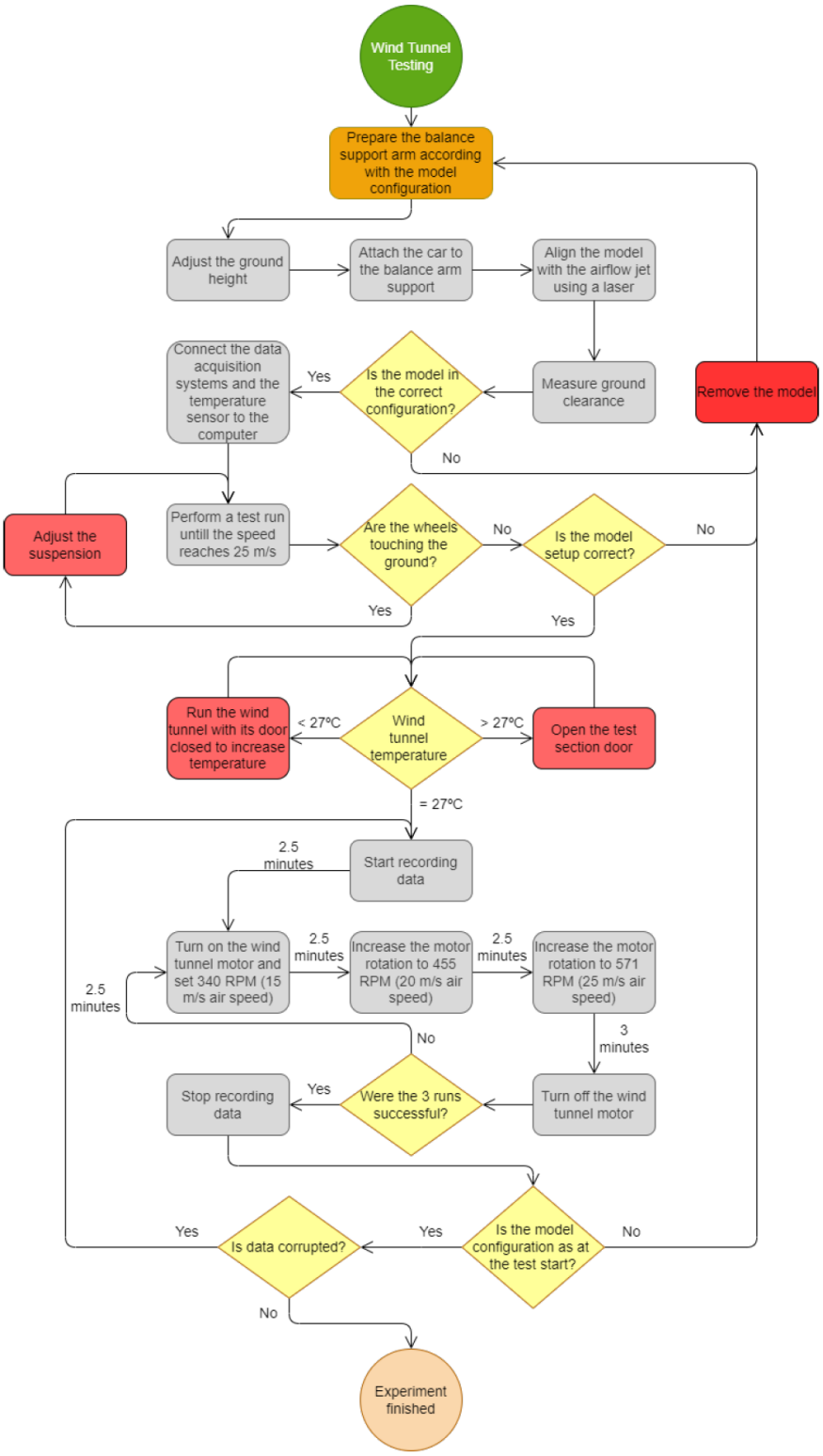

Figure 2.28: Wind tunnel testing methodology [2]

2.5.2 CFD Test and Validation

On the other hand, the work present on Carreira [1] was mostly focused on the computational domain. On the base of the simulations, the author modeled the full-scale geometry, where many parameters can be easily modified to facilitate the study of different configurations.

Resorting to the CFD software Star CCM+ by Siemens, the numerical models that best captured the physical phenomena were chosen (presented on sec. 3.1) and a mesh convergence study was performed. For the case of the models, the option of using a transition model (Gamma Transition) for the simulations was discarded as the changes in the variables of study, forces, and moments were not considered significant for the price of an increase in the computational time. The changes in pressure coefficient (fig. 2.30) were mostly found on the front wing.

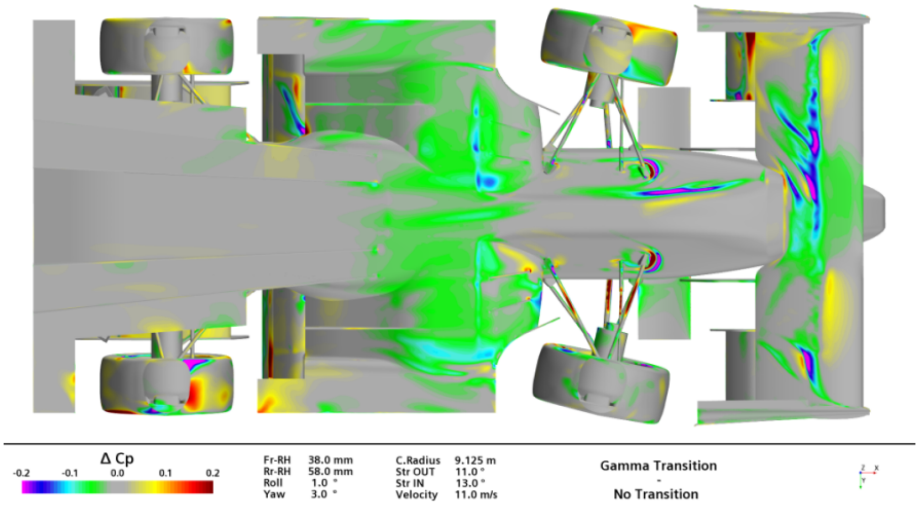

Figure 2.30: Transition study

For the mesh refinement study, an Adaptive Mesh Refinement (AMR) method was tested, where the mesh size is automatically adapted, either to coarser or finer grid sizes, in the function of the solution for a chosen variable. For this case, the total pressure was chosen and the adaptive behavior was defined. Although it presented good results and better capturing important vortex structures, this method was discarded as it proved to be too sensitive to the corner radius and a fully converged simulation could not be obtained. Refer to [1] for the error analysis.

Considering the parametric study, which was the core deliverable of that work, a complete macro including the mesh generation, the simulation, and the post-processing was developed in order to automate the simulations, speeding up the preparation process while granting that human errors on the setup were minimized. More than one hundred different configurations were tested by varying, separately, front and rear ride heights, roll angle ϕ, steering angle δ, and yaw angle ψ. Given that the simulation parameters for my thesis were determined by the study performed in [1], a good part of this macro could be used with some adaptations for the simulations performed.

As a result of this process, many conclusions were drawn. Lower ride heights (RH) proved to obtain

higher downforce, up to a certain threshold where the reverse effect takes place (enforcing the effect described in subsection 2.2.2). When a roll angle is added to the baseline configuration, both downforce and drag register a decreasing trend, this was attributed to the side of the front wing that gets closer to the ground presenting a behavior similar to the one described before for lower RH. Changes in steering angle do not impact significantly the drag and downforce generated, although it alters the structure of the flow, i.e. the outer rear wing tip vortex is strengthened and the inner is weakened. At last, by increasing the yaw angle, a large drop in downforce and drag was observed, accompanied by a drastic forward shift of the center of pressure.

Chapter 3

Baseline Performance

This chapter serves as a starting point for all the studies performed on the prototype throughout this work. First, the CFD setup used will be described alongside how the data will be presented in this document. Next, the lift and drag goals retrieved from the aforementioned study resorting to the vehicle dynamics tool provided as well as other results are discussed. On sec. 3.3 the current prototype is analyzed from an aerodynamics perspective and the underperforming regions are identified.

3.1 CFD Setup Parameters

3.1.1 Computational Domain and Numerical Models

The geometry used as a baseline for this study is a clean, airtight, simplified CAD model of the prototype FST10e, where a driver was added (since its impact on the rear wing performance cannot be neglected). Also, the tires were slightly changed to account for the deformation. Additionally, it is important to remember that the reference frame introduced in sec. 2.1 will be used.

Unlike Carreira [1], which performed a parametric study of specific configurations of the car (like changing the rear ride height), the changes in the design that will be the focus of this work are based on additions or changes of the aerodynamic components. The software used for the designing phase was Solid Works.

As to not waste resources repeating the procedures and grid refinement studies done by [1], the domain and setup for the simulations presented next, along whith the mathematical models and boundary conditions chosen resulted from that work so, refer to it for further information. As, ultimately, the validation of the mathematical model through wind tunnel experiments can only take into account straight flow, the design phase of this work will also consider solely straight flow. That being said and taking advantage of the fact that the flow will be nearly symmetric, to save computational effort by reducing the number of cells, only half of the car will be used and the results will be mirrored. The domain consists of a 50x7x10 rectangular prism (fig. 3.1).

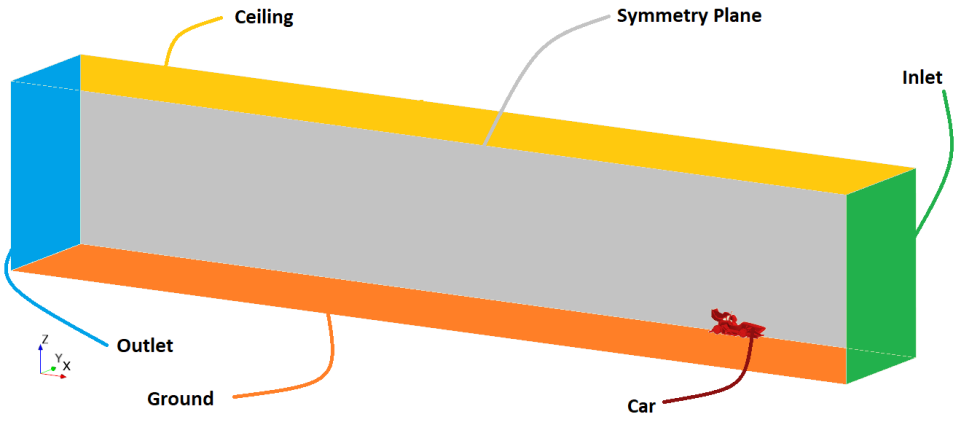

Figure 3.1: CFD domain

To model the physical phenomena, the following setup was used:

- **Boundary Conditions (BC) -** Velocity inlet (15m/s); Pressure outlet; No slip condition on the floor ground and all the car surfaces (rotating wheels); Symmetry BC on the remaining faces.
- **Mathematical Models -** Reynolds-averaged Navier-Stokes; Fully turbulent free stream, $k-\omega$ SST turbulence model; Steady flow; Segregated flow, Incompressible fluid with constant viscosity.
- **Additional techniques** FVM; Three Dimensional; All y+ treatment; Cell Quality remediation.

As referred in sec. 2.5, both a transitional model and adaptive mesh refinement were discarded as the small changes do not compensate for the additional computational effort.

Additionally, all this procedure is automated by means of a macro (coded in java) to allow for less downtime of the workstations and more simulations on the equivalent time. From the mesh convergence study previously performed, which resulted in a 10 million element mesh.

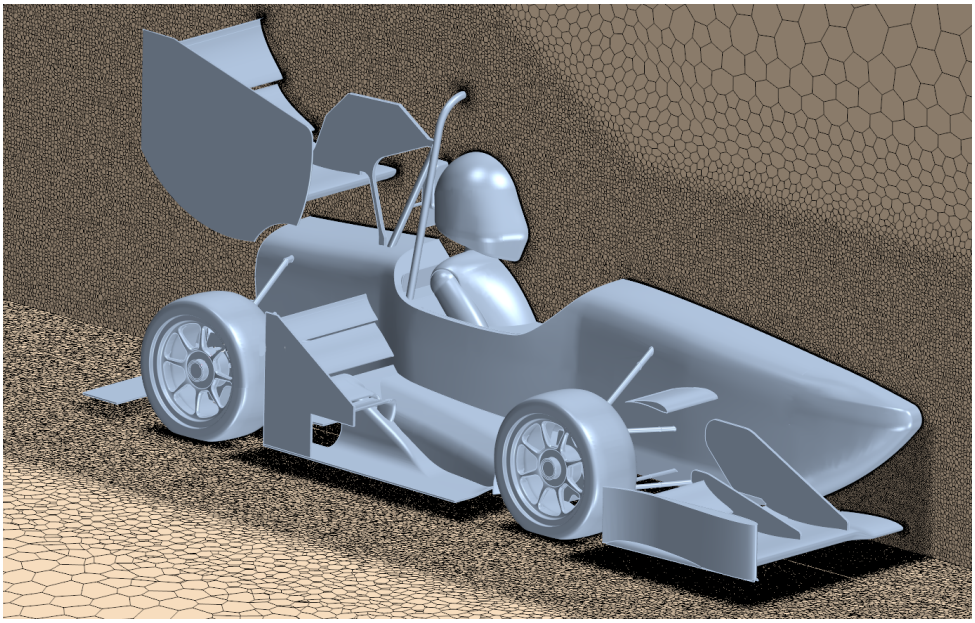

Figure 3.2: Mesh

It is noteworthy that the model that will be used later for the wind tunnel experiment does not include some components, namely the radiator and fan, and that the floor will be static. In addition, as the data acquired is returned on a 6-bar balance connected to the car, the tires have to be lifted from the floor, so there is no transmission of forces between the car and the floor or to any other structure other than the balance. Nevertheless, for the initial design phase, it was decided that the conditions simulated should be the closest to the real racing case, justifying the setup aforementioned. More considerations on the limitations of the wind tunnel can be found on sec. 5.1

3.1.2 Post-processing

After the models and other specifications are selected and the numerical simulation starts, it is important to monitor some parameters for convergence, namely the continuity, momentum, turbulent kinetic energy, and specific dissipation rate residuals, as well as the forces (both overall and for each component) and the pressure drop on the cooling components.

For the post-processing itself, three types of data were collected:

- **Flow and force reports:** a spreadsheet can be exported with the drag, downforce, and side force on all the components as well as mass flow in defined areas;
- **Pressure plots:** static pressure and friction plots on predetermined sectional cuts of the components;
- **Figures with data either from the airflow on or from the surface of the car**

In general, the figures previously mentioned will follow the pattern depicted in fig. 3.3.

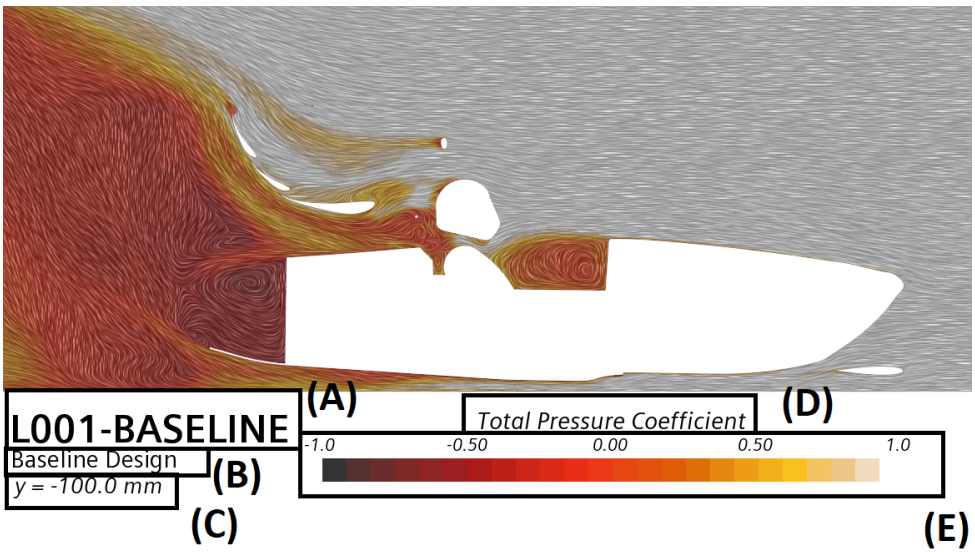

Figure 3.3: Post-Processing window pattern

- **(A) -** Simulation number and code;
- **(B) -** Title of the design which might contain some details;

- **(C) -** Additional information, like the section plane focused;

- **(D) -** Scalar or vector quantity of study;

- **(E) -** Colorbar.

3.2 Vehicle Dynamics Simulation

3.2.1 Dynamic Model

In order to better understand the influence that changing aerodynamic parameters can have on the overall performance and handling of the car, a brief study was performed making use of the race simulator that is currently in use and was provided by the vehicle dynamics department of the team.

perfectLap is a MATLAB-based, quasi-steady state, point-mass with longitudinal loads transfers car model, lap-time simulator. It allows the user to vary multiple car parameters such as wheel characteristics and friction, mass and dimensions, and aerodynamic coefficients. The user can model a track from scratch (via CAD) or choose one of the many existing tracks available. Then, restrictions and the desired settings for the events to be simulated must be chosen. With all these inputs, the tool returns the velocity and energy plots, the lap time, and the points awarded on each event based on a reference time.

To model the vehicle's progress on track, the simulator resorts to Newton's equations of motion. By repeatedly checking the vehicle's velocity and comparing it to the following section limit, and bearing in mind the maximum accelerations achievable (not only from driving and braking but also due to aerodynamic drag and rolling resistance), the velocity in the next step is estimated. The fluxogram of the simulator can be found in fig. 3.4.

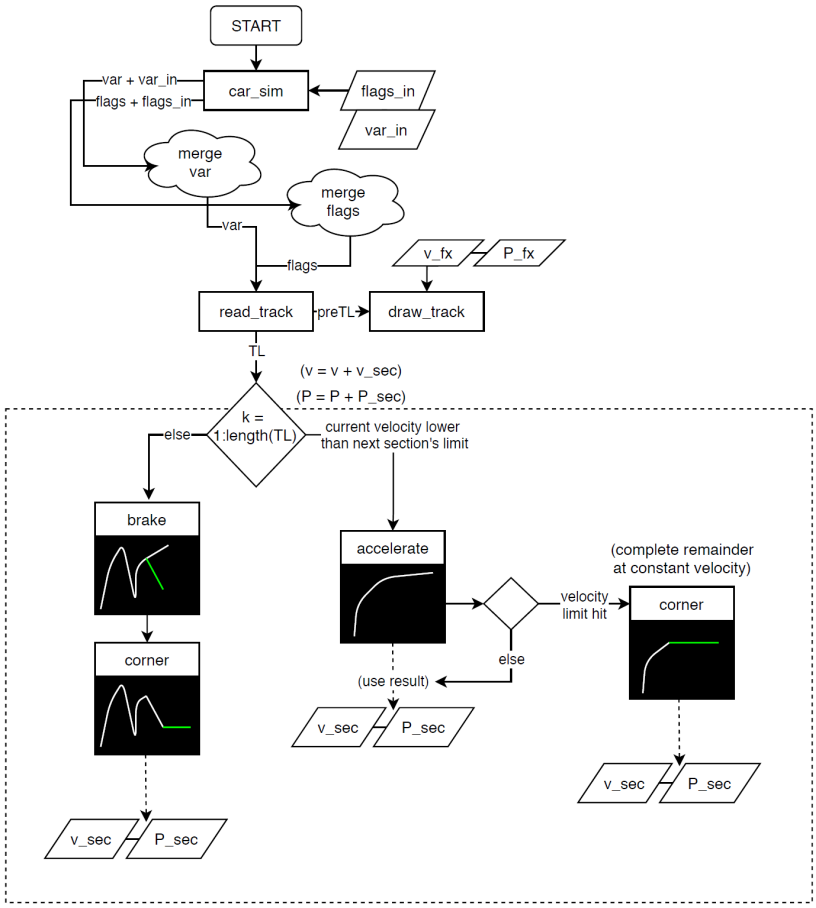

Figure 3.4: perfectLap Fluxogram

3.2.2 Updated Model

Although this simulator considers some key aspects of the race, as well as some characteristics of the car, the segregation of drag and downforce contributions (meaning that drag would vary as an independent parameter) and the lack of relation between gains in aerodynamic performance and changes in mass, some minor changes on the code were conducted in order to achieve a more realistic model.

First, based on the aforementioned data obtained from Carreira [1] and data from a stripped car (i.e. without an aerodynamic package), a parabolic regression that related the drag with the downforce generation was found. Parabolic regressions are commonly found on the drag polar ($C_D = C_{D_0} + k_1 C_L + k_2 C_L^2$) of aerodynamic bodies at subsonic speeds and that is the reason behind the choice of this approach. The spread of data can be found in fig. 3.5, which resulted in the parabolic regression:

$$C_D A = 0.0244(C_L A)^2 + 0.2616 C_L A + 0.4232. \tag{3.1}$$

Unfortunately, changes in attitude on this type of car are not supposed to cause substantial changes in the aerodynamic forces, being that the reason why the data is so contracted. Nevertheless, for this set, the parabolic regression yields in a $R^2 = 0.934$ and given that the purpose of this work is to change

a single component of the car and not redesign it in its entirety, it is expected to model the behavior satisfactorily.

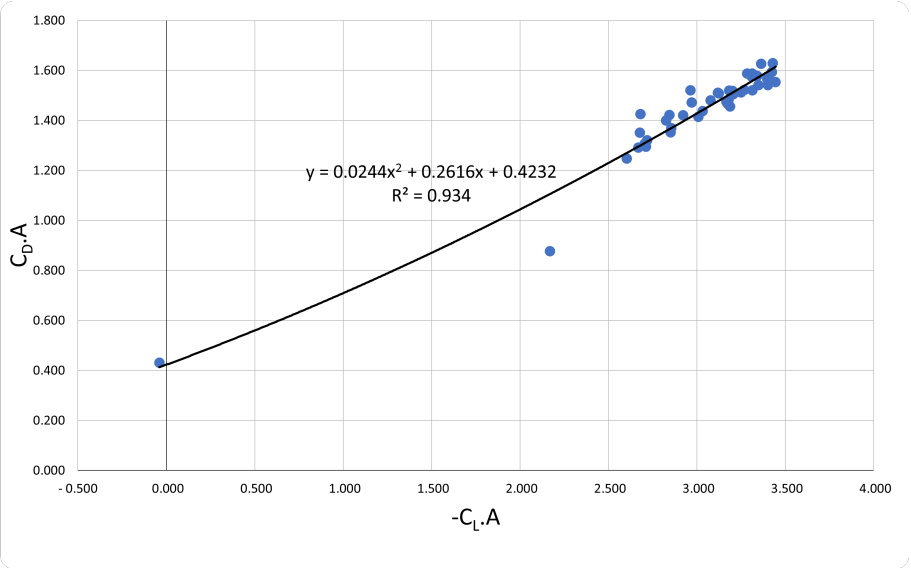

Figure 3.5: Drag polar data and parabolic regression

Secondly, from the need to relate the increase in mass with the additional aerodynamic performance, a ”worst-scenario” relation was established. This was done by relating the weight of the aerodynamic package after the manufacture of the components of the two most recent prototypes of the team (FST09e and FST10e) with the additional surface area. This resulted in the relation:

$$m = 2.67 C_L A + 1.673. \tag{3.2}$$

It is noteworthy that this relation does not correspond necessarily to reality as C_L can be increased without increasing mass (for example, by redesigning components). This relation was added as a ”worst-case scenario”, one where the increase in downforce would have a penalty in mass, given that, like in real racing, the simulator is sensitive to it.

3.2.3 Aerodynamic targets definition

A new study was performed with the updated vehicle dynamics model, where the goal was to determine the optimum C_L value to be used as a reference for the design phase. As the main purpose of the prototype is to perform well on the competition as a whole (rather than peak velocities or peak accelerations), this study focused on the scores hypothetically obtained in the dynamic events previously described in sec. 1.2, both overall and for each individual event.

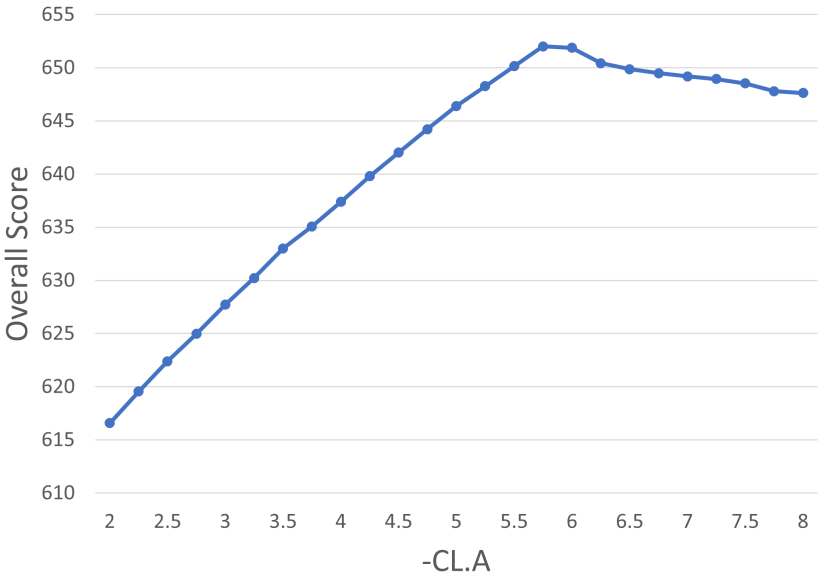

Figure 3.6: Predicted variation of the overall score with $C_L A$

Figure 3.6 summarizes the results obtained for the sum of all the events. From the observation of this plot, one can conclude that increasing the downforce is always desirable up to the value of $C_L A = 5.75m^2$, where the score reaches its maximum and from where it decreases towards a constant. Although a guiding path can already be decided, as the optimal value of $C_L A$ is substantially higher than the current one, breaking down this variation of scores between the multiple dynamic events can help understand how the parameters influence each type of event and assess if the simulator is responding as expected.

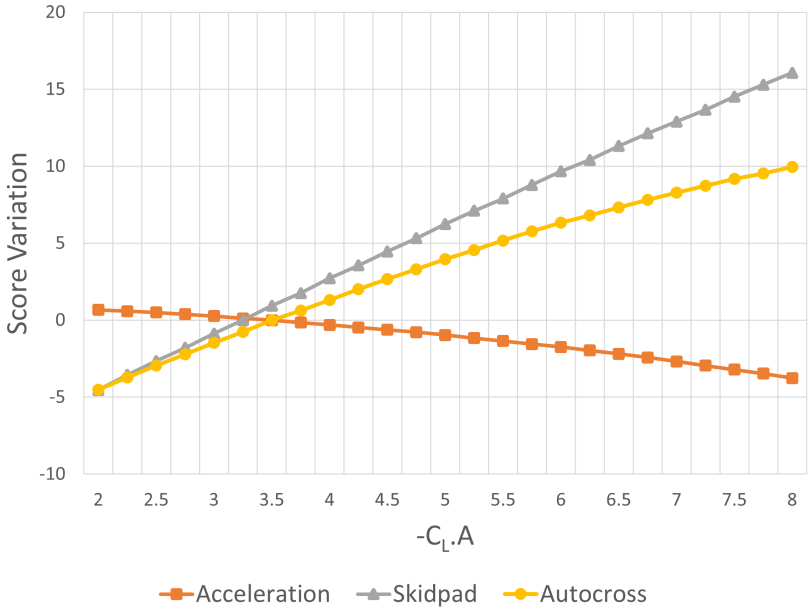

Figure 3.7: Score variation of separated events with $C_L.A$

In fig. 3.7 the variation of the score for the skidpad, autocross, and acceleration events is displayed. One can easily infer that an increase in $C_L A$ is advantageous for the autocross and the skidpad event, being the improvement for the first more pronounced. This is in accordance with what was expected since, in these two events, the car is subjected to high accelerations (lateral accelerations in the first case, and both longitudinal and lateral in the latter) so the traction enhancement due to the additional vertical aerodynamic force will allow higher speeds and ultimately lower times for the completion of the tracks. As the speeds achieved are relatively low, the drag has a low impact on these events. Nevertheless, this is probably the differentiating factor that causes the autocross event to benefit increasingly less for higher $C_L A$ values. In contrast, the increase in $C_L A$ proves to be disadvantageous for the acceleration event, mostly due to the increased drag that becomes prevailing for the achieved speeds, lowering the peak velocity.

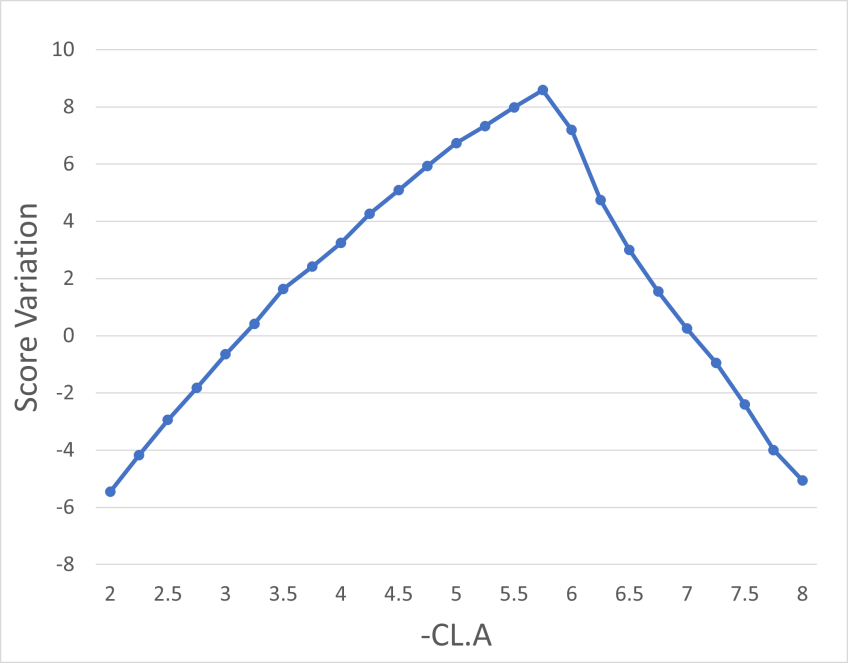

Figure 3.8: Score variation of endurance and efficiency with $C_L.A$

Lastly, the impact of the increase in $C_L A$ on the endurance and efficiency events can be found in fig. 3.8. This event focuses on efficiency and, as observed, is highly sensitive to the variation of the studied parameters and has a clear region where the points increase followed by a region where they decrease. This maximum was found to be $C_L A = 5.75m^2$, similar to the overall score maximum in fig.3.6

From this study, and given that the current $C_L A$ of the FST10e prototype stands around 3,7, the focus of the redesign should be on increasing the downforce generated. Adversely to what was believed, this study indicates that the score obtained on a Formula Student competition is not much sensitive to drag, especially considering that the events where the drag becomes detrimental (i.e. acceleration and endurance) were simulated from a ”single-configuration-car” point of view, and it is known that the angles of the rear wing’s flaps can be adjusted depending on the event which allows for a substantial reduction of the total drag.

3.3 Airflow Analysis

As a starting point, a comprehensive analysis of the airflow and components of the baseline model should be performed in order to assess its current performance. This analysis will be supported by adequate images of the post-processing of the simulation results. Figure 3.9 evidences the most important groups of aerodynamic structures present in the prototype and, although every part of it contributes to the aerodynamic behavior, these are considered the most influential.

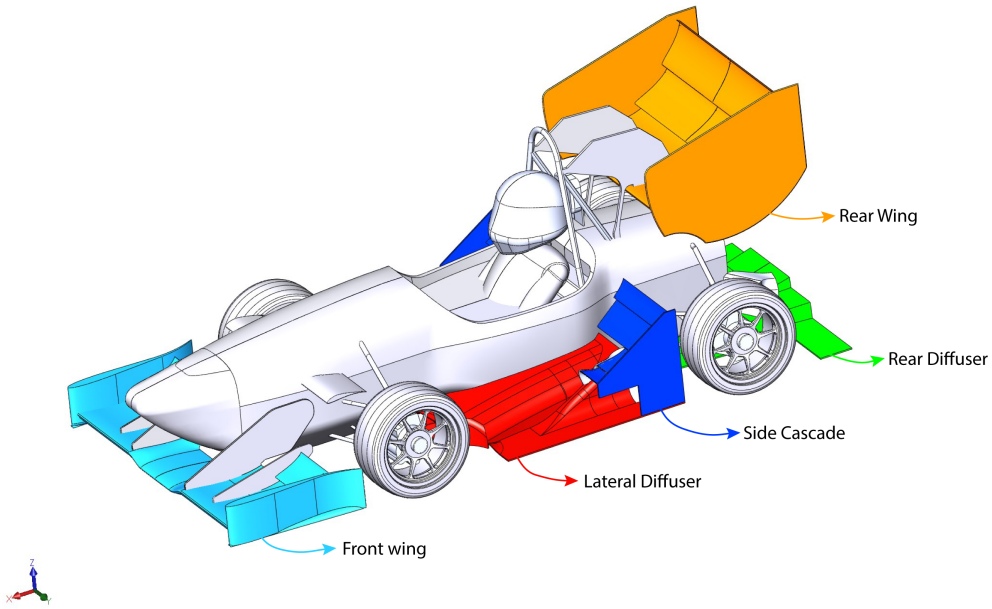

Figure 3.9: Aerodynamic package components

The piecharts found in fig. 3.10 reflect the current distribution of the drag and downforce among the aforementioned components and the car's monocoque. One can infer that the major players on the downforce generator are both the rear and front wings and the lateral diffuser (taking the lead). While both the side cascade and the monocoque (mostly due to the ground effect) still have some significance, the back diffuser is close to irrelevant. Considering the drag, the rear wing becomes the most detrimental component of the car, responsible for almost half of the total drag generated. Again, the back diffuser has little importance, the front wing takes advantage of the undisturbed air that surrounds it to minimize the drag, and the remaining components have a fair share of it. Additionally, it is important to note the high aerodynamic efficiency of the lateral diffuser ($L/D \approx 8.5$ for 15m/s), allowing it to generate a substantial part of the downforce and still not penalizing the car significantly.

In quantitative terms, for the speed of 15m/s, this translates into a total downforce of 500N, roughly a quarter of the weight of the car, and a total drag of 220N.

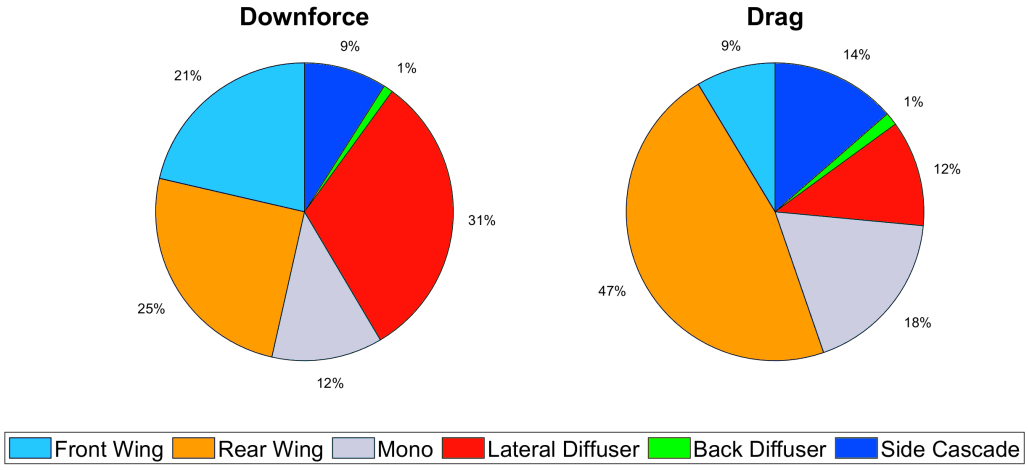

Figure 3.10: Current distribution of downforce and drag.

3.3.1 General behavior

Figures 3.11 a) and b) present the static pressure distribution around the car from two different perspectives, providing help to better understand where suction and pressure are more pronounced. By noting that the upper parts of the car mostly sit around positive pressure values and the lower part the opposite, one can conclude that there is an agreement among the different components and that the car is working towards sticking to the ground as a whole.

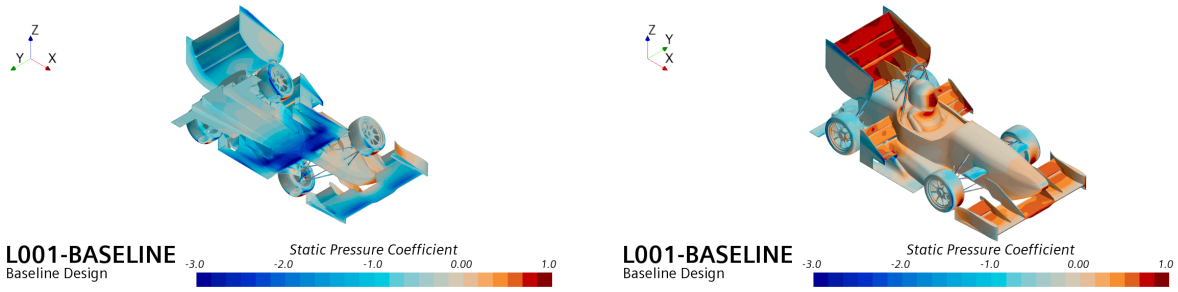

(a) Lower isometric view

(b) Upper isometric view

Figure 3.11: Static pressure on baseline design

By projecting this pressure in Z and X directions, (figures 3.12 a) and b), respectively), it can be verified that the distribution of downforce and drag goes accordingly to what was stated before and also highlight where, inside the component, the pressure is acting the strongest. In fig. 3.12 a) the vertical suction is more pronounced near the suction point of the front wing and on the high adverse region under the car between the end of the intake and the beginning of the side diffuser, which also corresponds to the lower part of the car, Figure 3.12 b) suggests that the two flaps of the rear wing compose the biggest sources of drag.

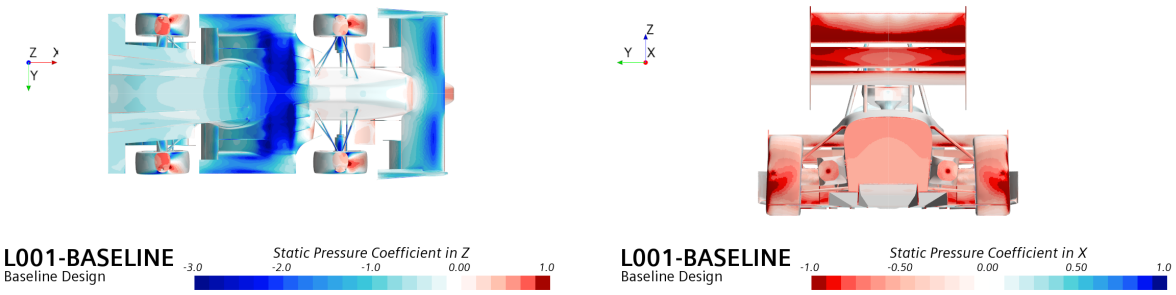

(a) In vertical (z-axis) direction

(b) In logitudinal (x-axis) direction

Figure 3.12: Axial and vertical pressure distribution

Figure 3.13 presents the absolute velocity of the airflow on a plane section close to the symmetry plane. From observation, one can easily identify regions where the flow is near stagnation, highlighted in blue, like the cockpit, the region immediately behind the driver, and the large wake region behind the car. It is also noticeable the upwash downstream, a clear indicator of the vertical change in momentum. On the other end of the spectrum, three main regions of accelerated flow are visible, under the front wing and the middle portion of the undercar, and below the flaps of the rear wing.

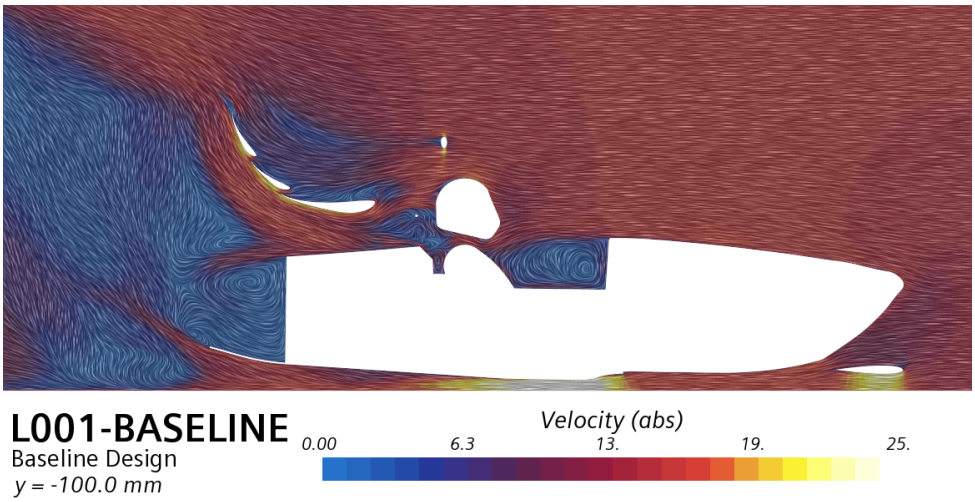

Figure 3.13: Airflow speed at y=-100mm

Side elements

On multiple occasions have been referred to the coupling composed of the different components of the prototype, being one of the best examples the system side diffuser, side cascade, and rear wing, which work together to potentiate its performance. The working of the side cascade is pretty straightforward as it is quite similar to the flaps of a standard airplane's wing where the added elements' suction peak will further of the diffuser flow and attenuate or delay separation. Although not behaving exactly in the same way, the presence and position of the rear wing have a similar effect on the flow that exits the cascade.

In fig. 3.14 (a) the negative relative static pressure makes it easier to understand the inter-dependency

of the system. In fig. 3.14 (b) is displayed, in green, some of the streamlines that enter the side diffuser (span-wise distributed), and it becomes clear that a fair share of them follow the path that has just been described. In red are highlighted the streamlines that exit through the back diffuser.

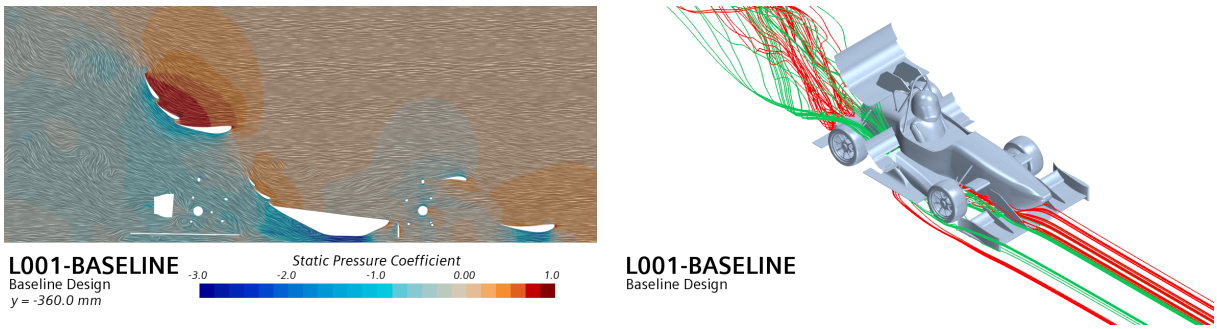

(a) Airflow pressure @y=-360.0mm (b) Streamlines

Figure 3.14: Lateral diffuser-side cascade-rear wing system coupled behaviour visualization

Front wing

As previously mentioned, the generation of vortices is pervasive in formula-type cars (refer to Sec. 2.2.2). The cut on figure 3.15 emphasizes the vortices that are being created on the front wing of the car: the wingtip vortex (1) which is formed as a direct consequence of the existence of an endplate, the footplate vortex (2) which is a controlled vortex generated to add an extra source of downforce due to the low pressure on its core. (3) and (4) are two counter-rotating vortices that are formed because of the gradient of pressures between the sides of the mid-span plate, (5) is formed on the upper edge of the support plate, finally, vortex (6) is generated on the transition loft between the symmetric profile and the airfoil-shaped one and flows to the floor, enhancing the suction generation at the intake of the diffuser. It is noteworthy that due to the numeric diffusion inherent to CFD the vortex structures might be incorrectly propagated downwind, altering the airflow.

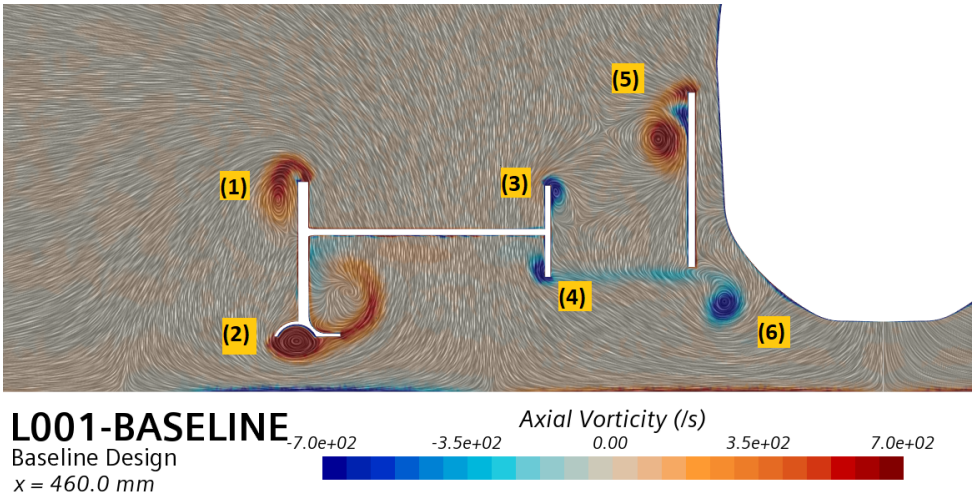

Figure 3.15: Vortex structures on front wing

Appendages

The bull horn was added to this car with two purposes, to prevent the large front wing vortices from reaching the rear wing and to generate a controlled vortex that will balance the rear wing endplate vortex and increase the performance and efficiency of this device. As fig. 3.16 illustrates, the bullhorn is far from fulfilling its purpose, and since it is a source of lift and drag, it should be either removed or modified.

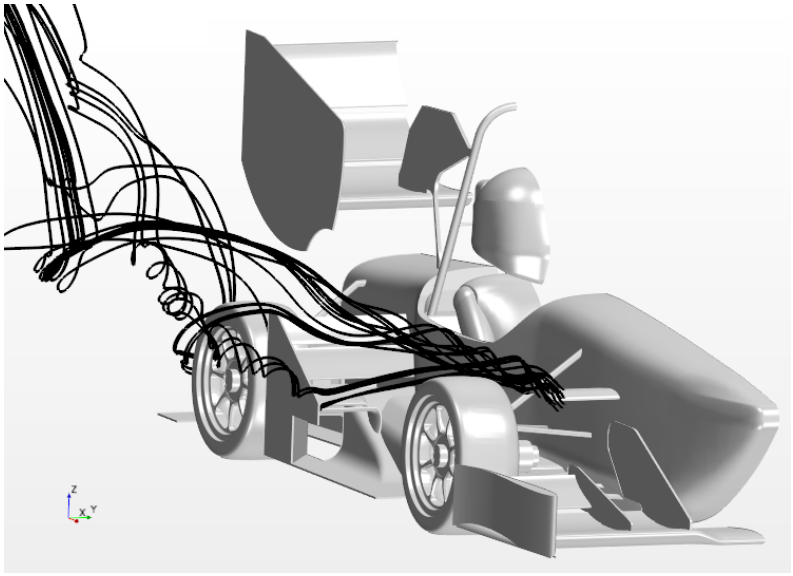

Figure 3.16: Bullhorn streamlines

One can also notice the addition of a small gurney flap (described on sec. 2.3) on the trailing edge of the last flap of the rear wing, its purpose here is to further increase the downforce.

Endplates

One of the purposes of the endplates is to attenuate the intensity of wingtip vortices. In the case of the side cascade, there is still a strong vortex being created at the endplate. In figure 3.17 a), one can highlight its low-energy core and the beneficial effect it has on deviating low-energetic flow (coming from upstream and from the wake of the rear tires) from the path of the rear wing can be identified in 3.17 (b) (as red implies outwash and blue stands for inwash).

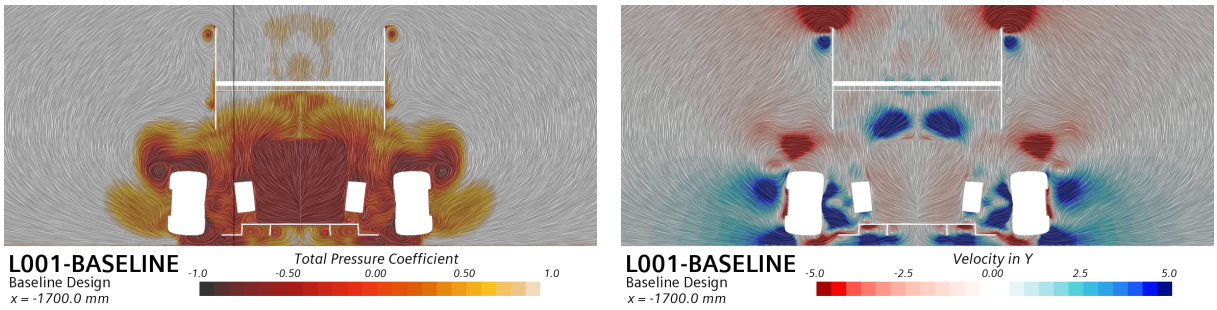

(a) Total pressure coefficient

(b) Velocity in Y

Figure 3.17: Side cascade vortex effect

One of the key innovations of the current front wing design was the airfoiled-shaped endplates. Its purpose was, in a first instance, to prevent part of the airflow coming from the front wing to reach the

front tires, and then, as an attempt to deviate the low-energy air that surrounds these tires from the remaining aerodynamic surfaces, so as not to worsen their performances. The high efficiency observed on the lateral diffuser is also a consequence of this innovation, as it works mainly in undisturbed airflow. Figure 3.18 a) offers good visualization of this effect.

Fig. 3.18 b) was added to ease the visualization of the outwash in the middle portion of the car which is a result of the aforementioned endplates, highlighted in red in the figure. There is a highlighted blue region downwind, this represents the inwash that is a result of both the low-pressure wake behind the car and the high suction below the rear wing.

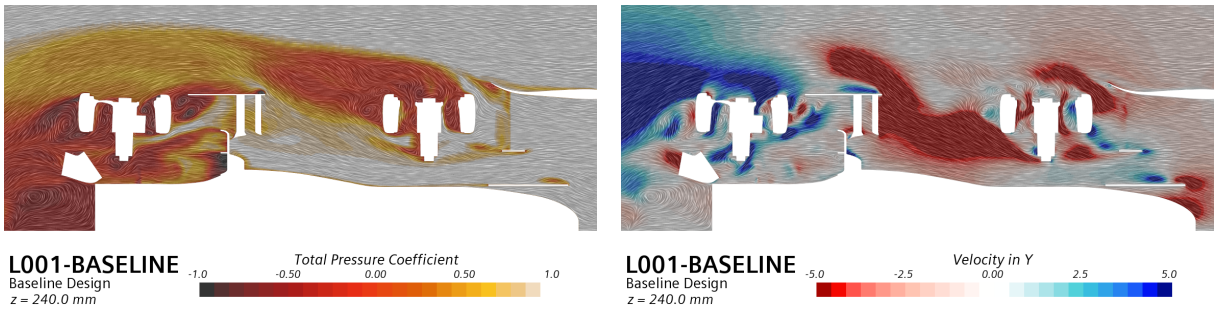

(a) Total pressure coefficient (b) static

Figure 3.18: Outwash due to the airfoiled front wing enplates @ z=240mm

3.3.2 Low Performance Regions Identification

Although being a highly efficient component and responsible for almost a third of the total downforce generated, the side diffuser was found to be housing a large separation region on its inner expanding zone, like fig. 3.19 (a) evidence. On (b) a region of reversed flow characteristic of high adverse pressure gradients can be identified by the blue color near the diffuser.

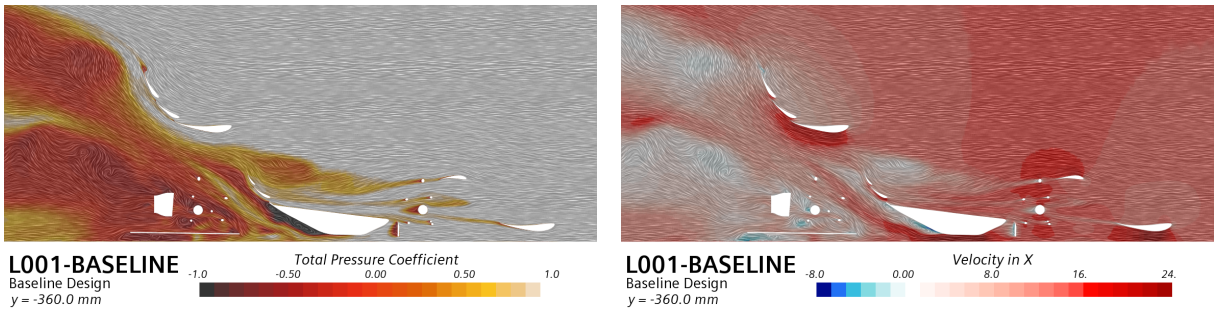

(a) Total pressure coefficient (b) static

Figure 3.19: Airflow under the car at y=-360.00mm plane

Next on the most evident issues from an aerodynamics point of view comes the large wake region behind the car. Although due to the particularity of the race track, where long straights are scarce and the speeds reached are relatively low, causing the drag penalty to be less impactful than it would be otherwise. This large region is spotlighted in fig. 3.20 (a) as the dark low-pressure zone, is limiting the

car's peak velocity, which directly affects the acceleration event and, at the same time, that is forcing the engines that will, ultimately, worsen the endurance and efficiency event.

Figure 3.20 also highlights the wake coming from the driver's head and heading directly to the rear wing. The impact of this lack of momentum present in this flow is depicted in fig. 3.20 (b) where the medium section (behind the head) of all the rear wing flaps is generating less downforce than the side sections.

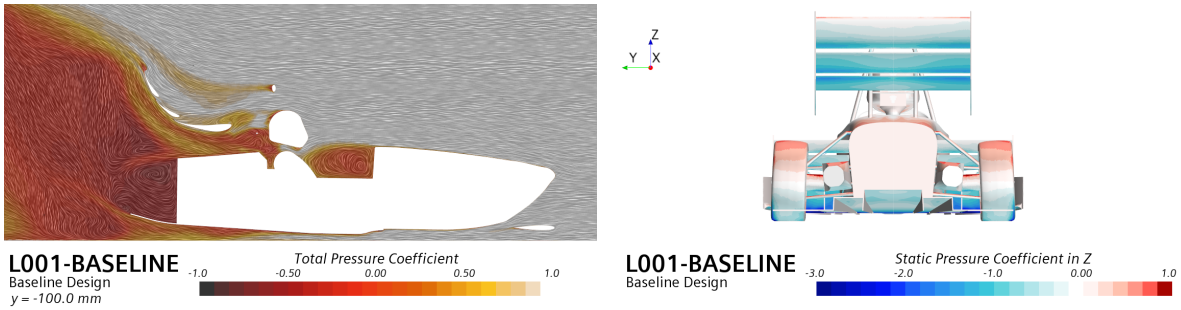

(a) Total pressure coefficient @y=-100.0mm

(b) Projection of C_P in Z

Figure 3.20: Visualization of the effect of the driver's head on RW performance and body wake

Figure 3.21 displays the projection of friction coefficient on the longitudinal x-axis, where red represents the reverse flow areas and, concerning the remaining areas, the greener they are, the higher the friction is there (and therefore more friction drag). Many undesirable regions can be identified, starting with the inner portion of the side diffuser that has already been described following fig. 3.19, a large separation zone can also be identified under the car close to the center, on a portion of the car designed to slowly expand the flow before it reaches the back diffuser. The front wing also presents poor behavior since a recirculation region can be found not only on the suction side of both the main wing and side flap but also on the pressure side. As this is the first component that the airflow reaches and will highly influence the rest of the car, it is highly undesired and must be tackled. The main flap of the rear wing also presents a recirculation zone on the pressure side. Many other less relevant spots of separation can be identified: on the back diffuser, on the pressure side of the side diffuser, and on the bull horn (reinforcing its detrimental behavior).

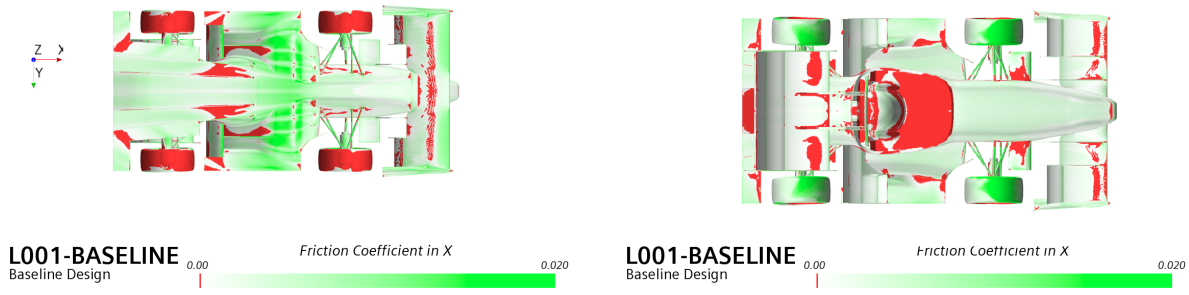

(a) Bottom view

(b) Top view

Figure 3.21: Friction coefficient on baseline design

Chapter 4

Car Modifications

In section 3.2 it was concluded that the best aerodynamic strategy to follow, in order to obtain better scores in the endurance and efficiency events, is to substantially increase the lift generated. Bearing in mind that the purpose of this work is to add or replace one component of the car and not to redesign the whole aerodynamic package, and given the complex nature of the interactions and influence between components, the main object of focus will be the undertray and the rear of the car, as changes there are less prone to drastically alter the airflow around other components, demanding unwanted redesign. At the same time, these regions of the car play an important role in the performance and still have room for improvement as seen in sec. 3.2. Whilst being a component with plenty of room to improve, the rear wing will be left out of this study as it is already the main focus of Morgado [3] that, is being developed in parallel.

Ergo, this study is composed of design iterations in two main regions: the **lateral diffuser** in sec. 4.1 and the coupling of the **rear portion of the car and back diffuser** in sec. 4.2. Between repetitions, variation in conditions, and scale models, around 40 simulations were performed, while around 30 different designs were considered. The complete CFD data for the considered simmulations is gathered on figs. A.2 and A.3.

4.1 Lateral Diffuser

Although referred to as lateral diffuser, the component that will be the subject of focus comprises not only the diffuser itself but also the intake, the in-between (lowest region), the flat plate on the side, and the lid that is covering all these.

As Section 3.3 suggests, the main issue that the diffuser is facing is the significant separation on its inner surface and, despite being the most efficient component of the prototype, not only can it be further enhanced if this problem is solved, but it might also improve the performance of the whole car by correcting it, since the airflow that leaves the diffuser after the expansion has yet to approach some other aerodynamic devices downwind.

It was decided to tackle this issue from two ends: the first is the more intuitive one: since separation

is usually caused by an adverse pressure gradient, the solution would pass by decreasing the expansion slope, even at the cost of losing some of the downforce generated. This is then followed by substantially altering the side cascade structure by increasing the suction on its upper two elements potentiating the diffuser (and ultimately compensating the loss of downforce); The second approach is all about redesigning the lateral diffuser, substituting the current 3-phase device (intake, flat floor, diffuser) for a continuous airfoil-shaped undercar. Figure 4.1 displays a section cut of an example of each of these designs, next to the current one.

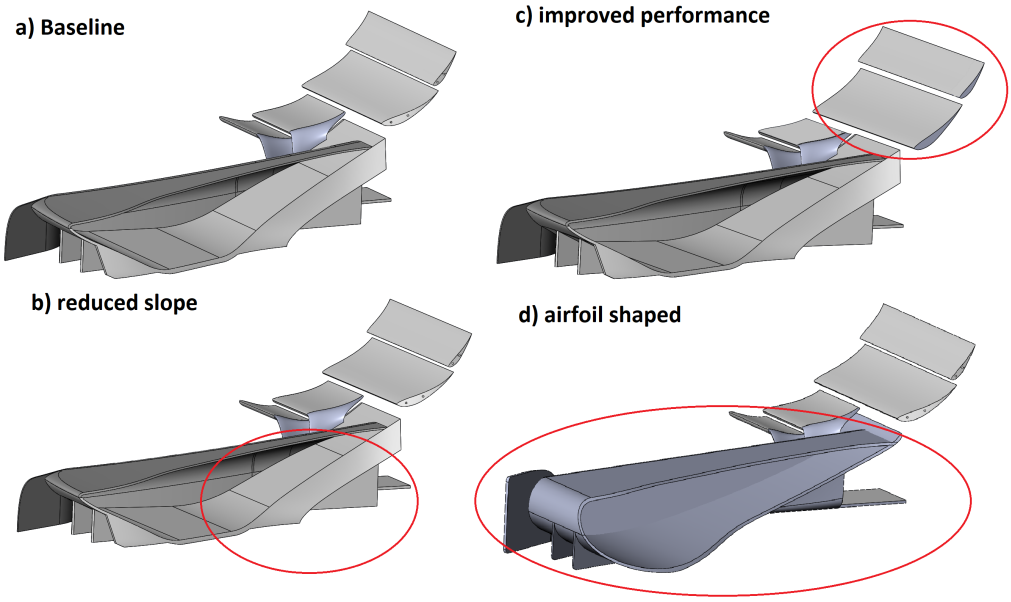

Figure 4.1: Studied lateral diffusers specimen

4.1.1 Avoid Separation

As referred to, the first approach consisted of decreasing the expansion slope. So, from the initial 25°, it was first reduced to 15° and then to 18°. As expected, both resulted in a small decrease in the generated forces not only on the diffuser itself but also in general terms. Nevertheless, it is noticeable that the relative decrease in drag surpasses the decrease in downforce, which, ultimately, upgrades the already most efficient aerodynamic device of the car. The aerodynamic efficiency $\frac{C_L}{C_d}$ rose from the initial 8.5 to around 9.15 and 9.2, for the 15° and 18° slope cases, respectively. Tables 4.1 and 4.2 include the main data retrieved for these simulations.

Table 4.1: Forces comparison among baseline and reduced lateral diffuser slopes designs

	Downforce (N)					Drag (N)				
	Base	15°	Δ (%)	18°	Δ (%)	Base	15°	Δ (%)	18°	Δ (%)
Force Coeff.	3.674	3.580	-2.5	3.623	-1.4	1.569	1.550	-1.2	1.570	+0.1
Front Wing	56.92	56.13	-1.4	56.10	-1.4	7.43	7.32	-1.5	7.32	-1.4
Mono	32.03	30.43	-5.0	31.13	-2.8	15.68	15.20	-3.0	15.38	-1.9
Lateral Diffuser	83.72	79.48	-5.1	82.04	-2.0	24.46	24.87	+1.7	25.03	+2.4
Side Cascade	23.96	24.37	+1.7	24.51	+2.3	24.46	24.87	+1.7	25.03	+2.4
Back Diffuser	2.70	3.15	+16.9	2.24	-17.1	1.19	1.31	+9.8	1.21	+1.3
Rear Wing	66.73	67.13	+0.6	67.48	+1.1	40.15	40.11	-0.1	40.59	+1.1

Table 4.2: Efficiency comparison among baseline and reduced lateral diffuser slopes designs

	Baseline	15°	Δ (%)	18°	Δ (%)
Overall	2.342	2.311	-1.3	2.308	-1.5
Front Wing	7.66	7.67	+0.1	7.66	+0
Mono	2.04	2.00	-2.0	2.02	-0.9
Lateral Diffuser	8.45	9.15	+8.3	9.19	+8.8
Side Cascade	0.98	0.98	+0	0.98	0.0
Back Diffuser	2.26	2.40	+6.5	1.85	-18.1
Rear Wing	1.66	1.67	+0.7	1.66	+0

Fig. 4.2 displays a view of the diffusers as seen from below, where the airflow is coming from the right to the left, and the black lines represent the streamlines on the vicinity of the surface. By comparing the friction coefficient on the surface of the diffuser, it can be concluded that even if the viscous force decreases, the airflow remains attached longer, delaying separation, which was the main goal of this first stage. As both both designs fulfilled its purpose and the 18° delivered better results, that is the design that will be further analyzed and be adapted on section 4.1.2.

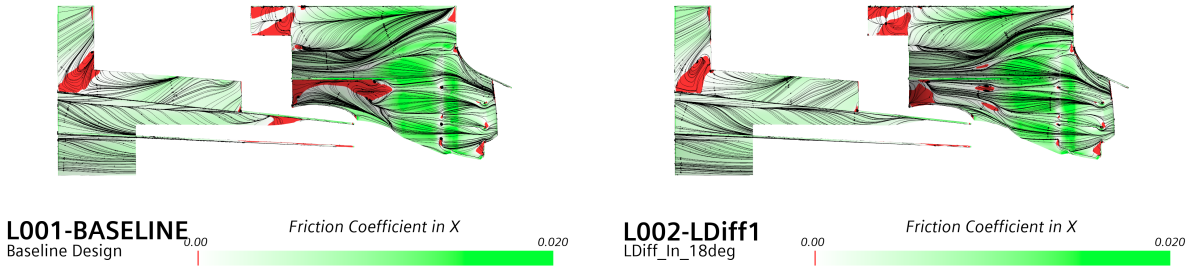

(a) Baseline design

(b) Design with 18° slope

Figure 4.2: Friction coefficient on the surface of the lateral diffuser (reduced slope)

In figure 4.3, the pressure coefficient around the diffusers is plotted. Not only can one observe that the suction peak is more pronounced, but the pressure recovery, is also enhanced.

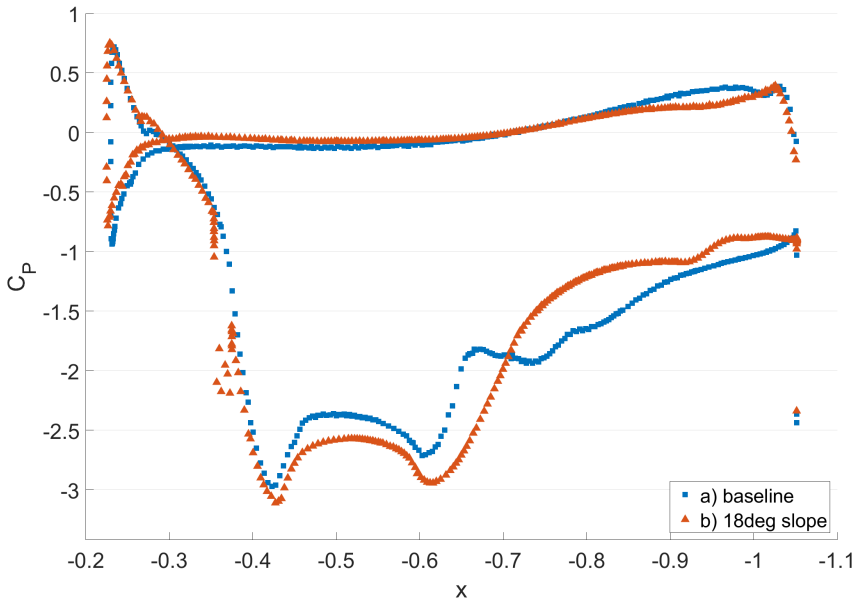

Figure 4.3: C_P plot of lateral diffuser on section cut y=360.0mm

Additionally, a rounded diffuser was simulated. Similarly to the presented designs, separation was delayed but not avoided. However, in this case, the decrease in downforce was even more pronounced. Although not being, per se, a valuable design, it was useful as a precedence for the third group of changes in this component, which will be tackled in sec. 4.1.3.

4.1.2 Increase Performance

Now that the great region of separation is mitigated, it is important to regain the performance lost, especially in terms of downforce. As referred to multiple times, the car is a complex body where multiple structures interact beneficially for better behavior. In this particular case, the side diffuser and the side

cascade work almost symbiotically, so a change in the first one will inevitably impact the second. To tackle it, the upper two flaps of the cascade were rotated and translated accordingly to the new shape, so that their suction would help reattach the underbody flow while incrementing its momentum through the mixing with the energetic airflow coming from above the lid.

Table 4.3: Impact of the rotated SC flaps on the forces and efficiency of the car

	Downforce (N)			Drag (N)			Efficiency (L/D)		
	Base	AVG	Δ (%)	Base	AVG	Δ (%)	Base	AVG	Δ (%)
Force Coefficient	3.674	3.691	+0.5	1.569	1.588	+1.2	2.342	2.325	-0.7
Front Wing	56.92	56.87	-0.1	7.43	7.45	+0.2	7.66	7.64	-0.3
Mono	32.03	31.18	-2.6	15.68	15.71	+0.2	2.04	1.98	-2.9
Lateral Diffuser	83.72	83.84	+0.1	24.46	9.11	-62.8	8.45	9.20	+8.9
Side Cascade	23.96	23.75	-0.9	24.46	24.26	-0.8	0.98	0.98	0.0
Back Diffuser	2.70	3.03	+12.5	1.19	1.31	+9.9	2.26	2.31	+2.4
Rear Wing	66.73	68.74	+3	40.15	40.74	+1.5	1.66	1.69	+1.5

Table 4.3 presents the average data resulting from designs performed during this phase, this time instead of presenting the results for all the tested designs, it was decided to present an average of the resulting forces, as, at this point, the main goal is to assess the main trends. From it, it can be concluded that the main purpose was fulfilled, as not only the generated downforce on the side diffuser increased to the point of surpassing the original value, but the performance of the whole system diffuser - cascade - rear wing was improved. Careful analysis indicates that although the impact on the cascade as a whole is barely insignificant, the two elements that were altered got their downforce increased by around 10 percent.

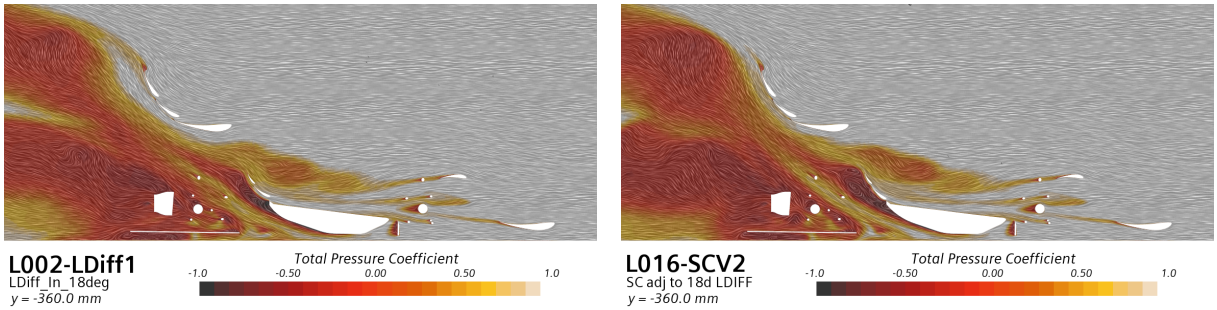

(a) Without side cascade enhancements

(b) With side cascade enhancements

Figure 4.4: Airflow's total pressure coefficient @ y=360.0mm

Analysing fig. 4.4, which displays a section cut where the flow used to separate strongly (as observed in sec. 3.3), a larger region of low energy flow appears to be forming after the cascade. On the other hand, an increased upwash is noticeable for the airflow over the rear wing which is consistent with its increased downforce value.

4.1.3 Airfoil Design

The last approach consisted of replacing the current format of the lateral diffuser with a continuous curving surface. This profile followed the suction side of the S1123 airfoil present on the front wing, which also works in ground effect. This allowed the airflow to work against a weaker adverse pressure gradient, leaving it less prone to separation. Additionally, as aforementioned, it is known that inverted wings are potentiated under ground effect.

Table 4.4: Forces comparison between baseline and airfoil-shaped lateral diffuser designs

	Downforce			Drag			Efficiency		
	Base	AVG	Δ (%)	Base	AVG	Δ (%)	Base	AVG	Δ (%)
Force Coefficient	3.674	3.691	+0.5	1.5655	1.588	+1.4	2.342	2.33	-0.7
Front Wing	56.92	56.48	-0.8	7.43	7.38	-0.6	7.66	7.65	-0.1
Mono	32.03	34.54	+7.9	15.68	14.29	-8.8	2.04	2.42	+18.3
Lateral Diffuser	83.72	86.64	+3.5	24.46	10.91	-55.4	8.45	7.94	-6.0
Side Cascade	23.96	22.14	-7.6	24.46	22.65	-7.4	0.98	0.98	-0.2
Back Diffuser	2.70	2.52	-6.6	1.19	1.23	+3.2	2.26	2.04	-9.5
Rear Wing	66.73	64.35	-3.6	40.15	39.44	-1.8	1.66	1.63	-1.8

Table 4.4 gathers the average downforce, drag, and efficiency data for the airfoil designs tested (which differ in small parameters like the slope and the shape of the lid). The increase in downforce on the monocoque and on the lateral diffuser highlighted on it can be verified in fig. 4.5.

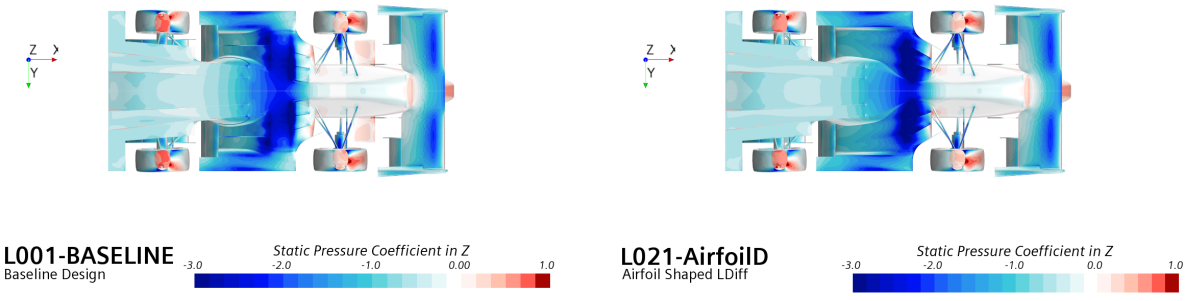

(a) Baseline

(b) Airfoil shaped lateral diffuser

Figure 4.5: Projection of pressure coefficient in Z - lateral diffuser comparison

Regarding the main purpose of this study, figure 4.6 suggests that separation was avoided and, considering that the performance was not damaged, these designs turned out to be up to the task. Unfortunately, this design led to a poorer performance both on the side cascade and on the rear wing, mostly because, as stated, they work together as a system and were dimensioned accordingly to the design of the previous lateral diffuser. It is noteworthy that the airfoil-shaped designs substantially improved the performance of the mono by increasing the downforce generated while decreasing the drag, which allowed up to 18% efficiency enhancement.

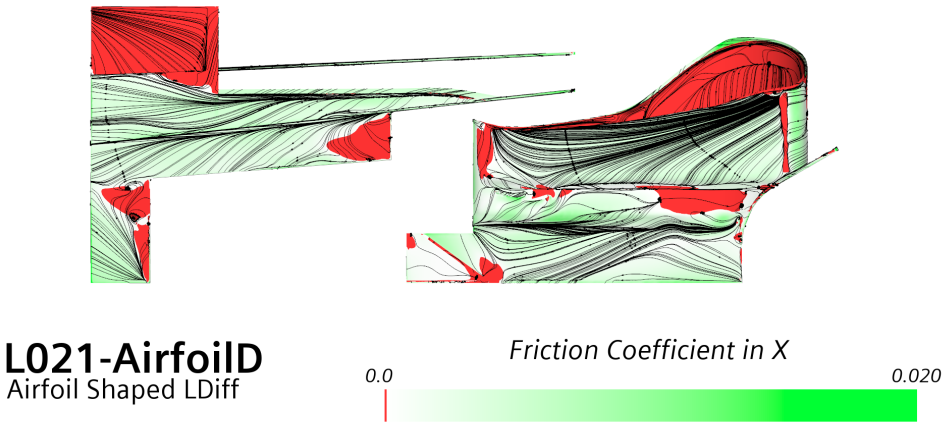

Figure 4.6: Friction coefficient on diffusers (airfoil shaped lateral design)

On a concluding note for the chapter, all the designs met the main goal - delaying the large separation region on the inner suface of the lateral diffuser. The two approaches presented similar overall results, nevertheless, the airfoil-shaped diffuser is chosen as the best design because the performance of the diffuser alone is substantially better and the car as a whole, for this case, has a lot more room for improvement, since the side cascade and the lid have yet to be further adapted to work together with the new diffuser. Fig. 4.7 displays the pressure distribution of the pressure along the upper and lower surfaces on a longitudinal section of the inner region.

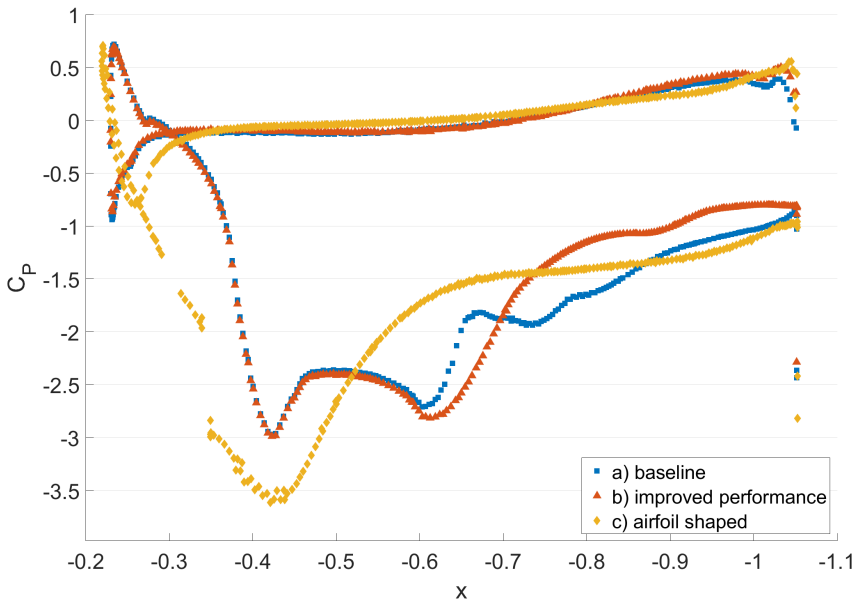

Figure 4.7: C_P plot of lateral diffuser on section cut y=360.0mm among cases studied

4.2 Rear Diffuser

Figure 3.10 evidences the small share that the back diffuser has on the gerated forces, which is a direct result of the lack of attention that the aft region of the car has received so far. Moreover, enhancing the effectiveness of the diffuser further improves the airflow under the whole car. Mainly because of these two reasons, this part of the work will focus on redesigning the aft region.

On the current model, the small thin extension of the back diffuser is seen to oscillate more than what would be desired when tested in the wind tunnel, altering the expected behavior by introducing additional unsteadiness. As this would hinder the validation of the components, and given that the current rear cut of the monocoque is responsible for a large region of wake downwind (figure 3.20), it was decided to extend the body of the prototype providing the necessary support for the new back diffuser and streamlining the design of the car at the same time. It is important to notice that with a larger contact surface, viscous effects will impact the drag generated, but, like in many applications in aerodynamics, it comes down to a balance between the form and friction drag.

Fig. 4.8 presents the current rear of the car followed by exemplars of models that contain the changes studied that will be studied in this section. As can be concluded, the design of this component revolves essentially around the definition of the profiles of the main and secondary diffusers, as well as the slope of the upper part, below the rear wing. So, despite not being a parametric thorough study of the variation of these slopes, it does consist of more subtle changes than the lateral diffuser design presented before.

This section will be divided into three sets of studies. First, to assess if this new part benefits the prototype, the focus was to extend the body of the car and change the slopes of both the expansion of the diffuser and the top of this rear block. Secondly, the idea of tilting the top upwards and its interaction with the rear wing as well as its influence on the flow as a whole was tested. The third study consisted of trying to further increase the downforce generated in two ways: a rounded profile and a diffuser with two consecutive expansion slopes instead of the current single expansion region.

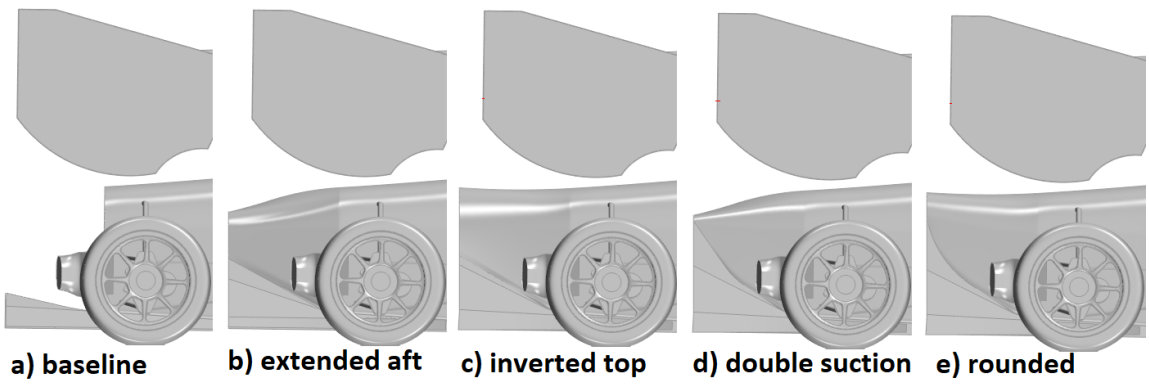

Figure 4.8: Studied aft region specimen

4.2.1 Monocoque extension

As mentioned, this set of designs is supposed to illustrate the impact that extending the monocoque can have on the airflow around and forces acting on the car. The results yield a starting point for the subsequent designs.

Table 4.5: Impact of extending aft region of car on forces and efficiency

	Avg DF	Δ (%)	Avg Drag	Δ (%)	Avg Eff. (L/D)	Δ (%)
Overall Force Coeff.	3.794	+3.3	1.580	+0.7	2.401	+2.5
Front Wing	56.71	-0.4	7.41	-0.3	7.65	-0.1
Mono	28.23	-11.8	12.96	-17.4	2.20	+7.5
Lateral Diffuser	87.41	+4.4	10.05	+1.4	8.70	+2.9
Side Cascade	24.87	+3.8	25.40	+3.9	1.0	-0.1
Back Diffuser	8.73	+224.1	3.63	+203.9	2.52	+11.8
Rear Wing	69.31	+3.9	41.10	+2.4	1.69	+1.5
MBR[1]	106.28	+4.8	57.69	+1.2	1.84	+3.6

Table 4.5 gathers the collected data regarding the average forces and efficiency of the main aerodynamic devices from the designs that meet the criteria of having a single straight expansion slope. A 4% increase in the downforce of the rear wing is noticeable on the table. Figure 4.9 illustrates the decrease of pressure on the suction side of all the elements of the rear wing, both near the centerline (y=0mm) and closer to its wing span (y=300mm) that is on the origin of the DF increase referred to.

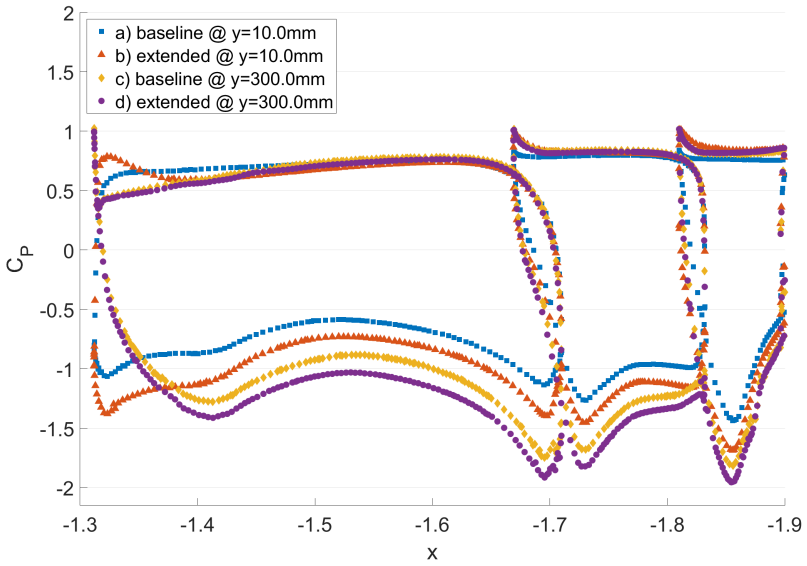

Figure 4.9: C_p plots on the rear wing for extended monocoque

By extending the rear portion of the car, the region of low pressure (wake) downwind, close to the

rear wing, that would lure the airflow downwards (limiting the momentum change upwards that ultimately generates downforce) ceases to exist, thus allowing the rear wing to increase its effect. Furthermore, the extended portion will have an effect on the rear wing similar to the ground effect on the front wing, which, by constraining the flow also contributes to this increase in downforce. While this effect only brings advantages when there is actually a ground surface promoting it, for this case, the decreased pressure between these two surfaces will end up pushing the lower (monocoque) upwards, thus the decrease in downforce noticeable in table 4.5 and which can be confirmed in fig. 4.10

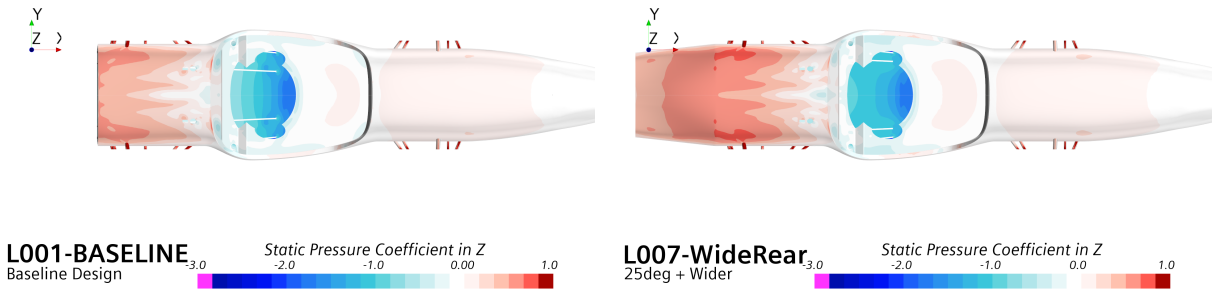

(a) Baseline design

(b) Extended rear

Figure 4.10: Pressure coefficient projected on Z acting on monocoque surface (comparison between baseline and extended rear)

From table 4.5 one can also notice the outstanding increase in downforce on the back diffuser and, although the improvement of this device is the main focus of this section, it is noteworthy that the forces, acting on this device, only contemplate the surface under the rear portion whereas for the baseline it also includes the upper surface of the diffuser, subjected to the low-pressure wake region. To bridge this gap and for the sake of a better understanding, throughout this study, the most important object contemplated is the group composed of the monocoque, the back diffuser, and the rear wing, which will be referred to as MBR from this point forward.

For this case, the average increase in downforce of the MBR was close to 5% while the increase in its efficiency stood around 3,5%.

Another noticeable change in the results is the increase in downforce of the side cascade on around 4%, confirmed by the increase in suction verified in fig 4.11. This increase is due to two main factors: first, the increase of the suction on the rear wing which, as has been reinforced in sec 4.1, works together with the side cascade and the lateral diffuser; and, secondly, the stronger suction on the rear of the car increases the mass flow under the car, which will help to enhance the performance of every component of the undertray.

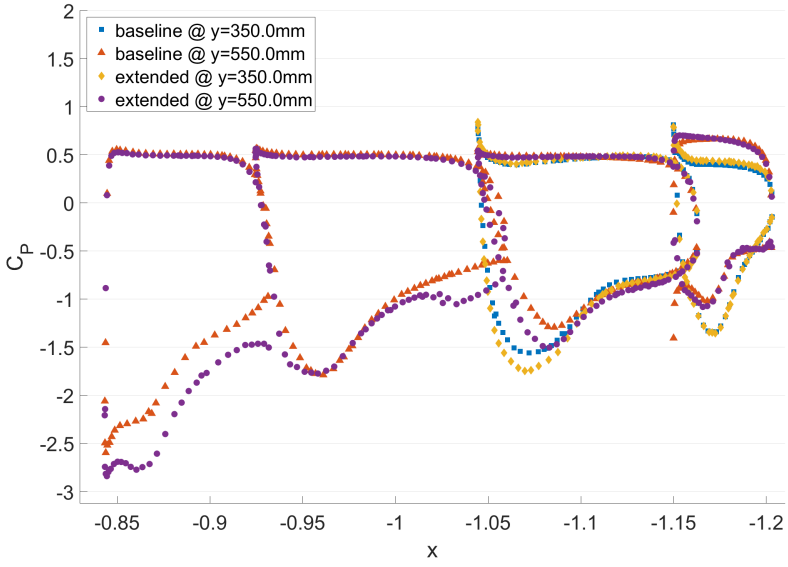

Figure 4.11: C_p plots on the side cascade for baseline and extended aft designs

Overall, it can be concluded that by extending the monocoque while subtly changing (or not) the slope of expansion of the back diffuser, the car can increase its generated downforce and efficiency up to 3.3%.

4.2.2 The Effect of Inverting the Top

For this set of designs, the top of the aft part of the car was tilted upwards. The results and their influence will be discussed next.

Table 4.6: Impact of inverting aft upper surface on forces

	Standard		Inverted		Standard		Inverted	
	Avg DF	Δ (%)	Avg DF	Δ (%)	Avg Drag	Δ (%)	Avg Drag	Δ (%)
Force Coeff.	3.805	+3.6	3.817	+3.9	1.5786	+0.6	1.583733	+1.0
Front Wing	56.85	-0.1	56.50	-0.7	7.44	+0.1	7.38	-0.7
Mono	27.17	-15.2	27.09	-15.4	11.60	-26.0	10.47	-33.2
Lateral Diffuser	88.39	+5.6	86.85	+3.7	10.11	+2	10.00	+0.9
Side Cascade	24.70	+3.1	24.63	+2.8	25.22	+3.1	25.15	+2.9
Back Diffuser	9.34	+246.4	11.25	+317.4	4.83	+304.4	5.99	+401.0
Rear Wing	69.83	+4.6	70.52	+5.7	41.35	+3	41.68	+3.8
MBR	106.68	+5.2	108.59	+7.0	57.87	+1.5	58.10	+1.9

Table 4.7: Impact of inverting aft upper surface on efficiency

	Standard		Inverted	
	Avg Eff. (L/D)	Δ (%)	Avg Eff. (L/D)	Δ (%)
Force Coefficient	2.41	+3.0	2.41	+2.7
Front Wing	7.64	-0.2	7.66	-0.1
Mono	2.34	+16.9	2.59	+26.5
Lateral Diffuser	8.74	+3.7	8.69	+3
Side Cascade	0.98	0.0	0.98	0.0
Back Diffuser	1.93	-3.8	1.88	-18.9
Rear Wing	1.69	+1.8	1.69	+1.6
MBR	1.84	+3.7	1.87	+5.1

Tables 4.6 and 4.7 gather the average values of the forces acting on the main aerodynamic devices alongside its efficiency from the five designs of each type. Considering the main focused group (MBR), the performance of the designs with an inverted top achieved 7% and 5% improvement in downforce and efficiency, respectively, surpassing its counterpart by more than a third of their increases.

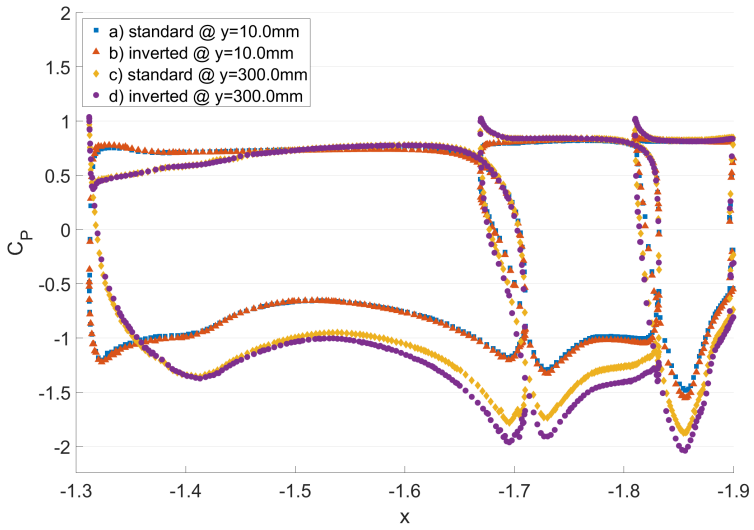

Figure 4.12: C_p plots on the rear wing for standard and inverted aft designs

Figure 4.12 illustrates the pressure distribution around the elements of the rear wing for similar designs in which the main difference is the tilt on the top. Although not much pronounced, the increased suction is noticeable on the inverted top case.

Figure 4.13 presents the pressure distribution, above and under (back diffuser) the rear part of the car's body. For the inverted design, near the centerline (4.13 (a)), a plateau is observable, in the place of the pressure decrease of the standard case. This happens because, by tilting it upwards, the airflow becomes subject to a favorable pressure gradient. In fig. 4.13 (b) the increase in pressure above the car

is also noticeable, but less pronounced.

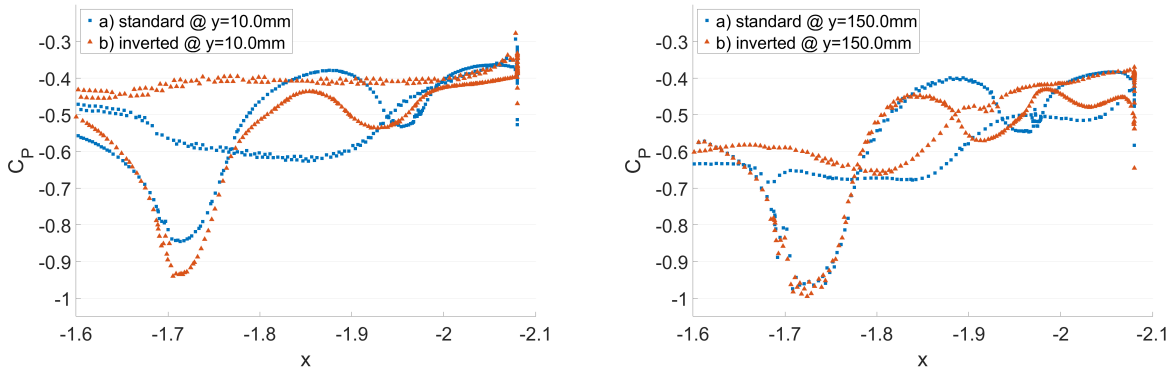

(a) y=10.0mm

(b) y=150.0mm

Figure 4.13: C_p plots on the body of the car for standard and inverted aft designs

The pressure gradients observed in figs. 4.12 and 4.13 justify the downforce difference between the two sets of designs.

4.2.3 Double Suction Versus Rounded Profile

For the last set of designs, two hypotheses were studied to further increase the performance of the back diffuser: the first one, based on the concept discussed in Ehirim et al. [43], consists of introducing a second expansion slope that will lead to a second suction peak and therefore to a second pressure recovery region; the other tested concept is the round diffuser, which is used in many applications and was used on the lateral diffuser case to avoid the abrupt pressure gradient present.

Tables 4.8 and 4.9 contain the average values of forces and efficiencies for the aerodynamic devices from designs in which the back diffuser follows the mentioned profiles.

Table 4.8: Forces comparison between designs with two expansion slopes and rounded back diffusers

	Double Suction		Rounded Diffuser		Double Suction		Rounded Diffuser	
	Avg DF	Δ (%)	Avg DF	Δ (%)	Avg Drag	Δ (%)	Avg Drag	Δ (%)
Force Coefficient	3.812	+3.8	3.832	+4.3	1.580	+0.7	1.593	+1.5
Front Wing	56.64	-0.5	56.63	-0.5	7.40	-0.4	7.41	-0.3
Mono	26.66	-16.8	27.08	-15.4	10.34	-34.1	10.08	-35.7
Lateral Diffuser	88.72	+6	86.00	+2.7	10.10	+1.9	10.07	+1.6
Side Cascade	24.54	+2.4	24.99	+4.3	25.05	+2.4	25.26	+3.3
Back Diffuser	10.60	+293.2	11.77	+336.5	6.19	+418	6.50	+444.1
Rear Wing	70.09	+5	70.87	+6.2	41.52	+3.4	41.92	+4.4
MBR	107.84	+6.3	109.72	+8.1	57.90	+1.5	58.50	+2.6

Table 4.9: Efficiency comparison between designs with two expansion slopes and rounded back diffusers

	Double Suction		Rounded Diffuser	
	Avg Eff. (L/D)	Δ (%)	Avg Eff. (L/D)	Δ (%)
Force Coefficient	2.417	+3.2	2.405	+2.7
Front Wing	7.66	-0.1	7.63	-0.4
Mono	2.56	+25.1	2.66	+30.3
Lateral Diffuser	8.82	+4.3	8.52	+0.8
Side Cascade	0.98	0.0	0.99	+0.9
Back Diffuser	1.80	-20.3	1.79	-20.8
Rear Wing	1.69	+1.8	1.69	+1.7
MBR	1.86	+4.4	1.88	+5.4

From the tables, it can be concluded that the main goal was achieved, as the accumulated downforce of the rear group MBR increased up to 6.3% for the double suction case and more than 8% for the round diffuser while also increasing its efficiency. Following the previous studies, this gain was made possible by maintaining the loss of DF on the mono and further improving the one generated both on the rear wing and the diffuser, through the redesign of the profiles.

Table 4.8 together with fig. 4.14 evidences the significant improvement in the downforce generated on the lateral diffuser for the first case, not only when compared with the baseline geometry but also when compared to a similar car that only differs in the back diffuser (they both have their top rear part tilted upwards and the rest of the design is the same). This reinforces the aforementioned idea that the car is a highly complex body where the change in a component may significantly alter the behavior of the airflow, ultimately influencing the effectiveness of other devices, in such a way that they cannot be thought of separately.

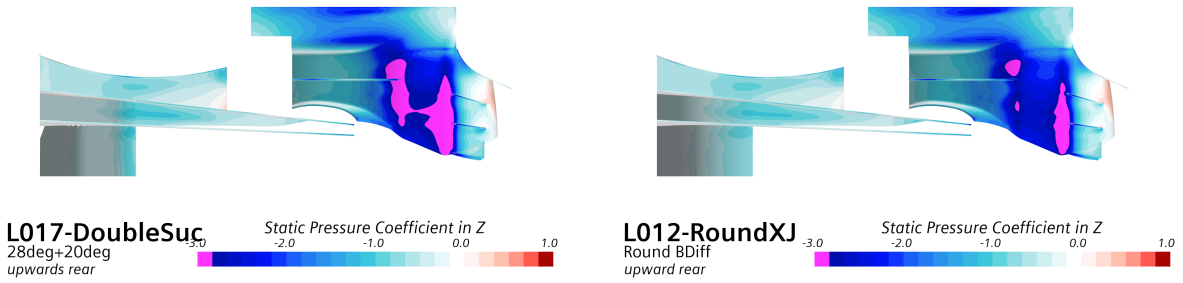

(a) Double suction

(b) Rounded diffuser

Figure 4.14: Comparison of pressure coefficient in Z between rounded and double suction back diffusers

The pressure distribution on the back diffuser is plotted in fig. 4.15 for both cases of study and a single expansion profile, like those analysed in sec. 4.2.1. From it, one can better understand that, even if the suction peak is weaker on the rounded profile, it is capable of generating a lot more suction than

its counterparts. Another conclusion that can be retrieved is the slightly better recovery of pressure on the double suction diffuser when compared to the other two.

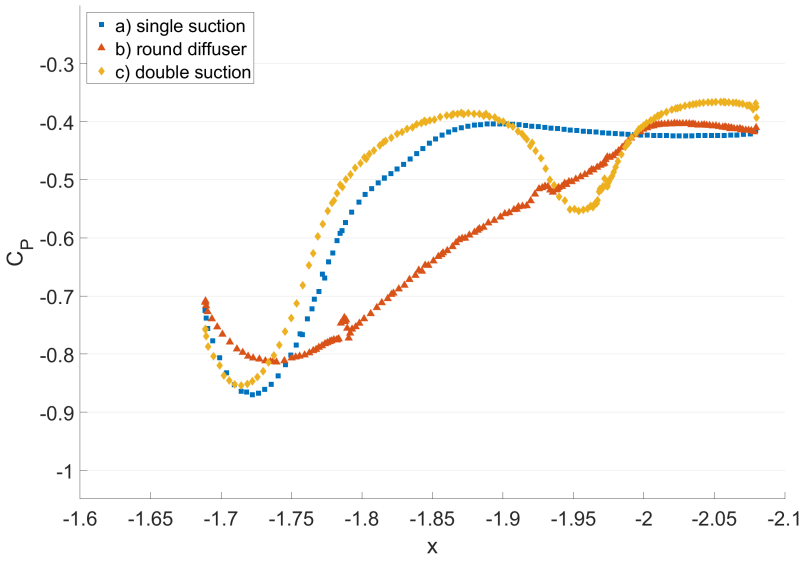

Figure 4.15: C_p plots on the back diffuser for the 3 diffuser profiles analyzed

Overall, the best result of the double suction case slightly surpassed the best one of the rounded profile diffuser, achieving a value of 3.857^2 and 3.847^2 for the C_L, respectively, corresponding to an improvement close to 4%.

On an additional note, figure 4.16 illustrates (in red) an undesired effect of the increased suction peak on the back diffuser: part of the flow that was supposed to nourish the upper devices is deviated to the undertray, flowing under the side cascade after passing above the front wing (the green streamlines represent the flow that reaches the expanding region of the lateral diffuser).

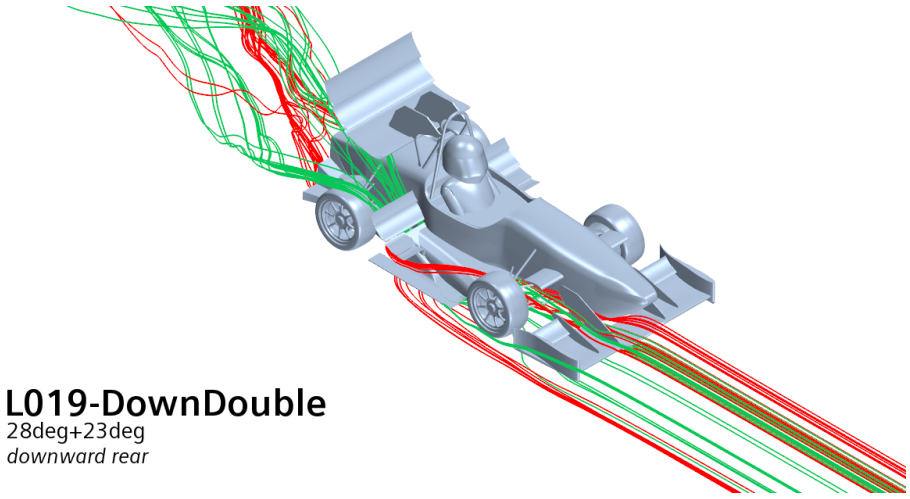

Figure 4.16: Airflow visualization on double suction back diffuser design

4.3 Chosen Region

From Sec. 4.1, one can retrieve that separation on the lateral diffuser could be both delayed and avoided just by adjusting the inner profile and that the interaction among the lateral diffuser, the side cascade, and the rear wing is clear and should be explored. From the performed studies, the airfoil-shaped diffuser performed significantly better than the intake-flat-diffuser system even with the drawback of not having the rest of the car design symbiotically to it. This also means that there is still a lot of room for improvement both on the profile employing a parametric study, but also by designing the side cascade and the lid accordingly.

Regarding sec. 4.2, it can be concluded that just by extending the rear of the car better performance is instantly achieved not only on the rear but on the car as a whole, due to the coupling of its devices. By exploring this concept, it was concluded that tilting the rear upwards could further increase the downforce generated both on the rear wing and on the back diffuser. Finally, two different groups of profiles were tested, one contemplating two consecutive expanding zones and the other a curved diffuser; they both presented good results, the first one achieving the highest downforce out of all the designs and the second obtaining an improvement in the downforce of the rear group (composed by the rear wing, the mono, and the back diffuser) of around 8%.

Taking into consideration the limitations of the wind tunnel tools and setup described in [2], where it was concluded that what can be extracted from the tests are mainly trends as well as some visual insights, the changes in the rear part of the car are more prone to impact the performance enough to present the aforementioned trends and ultimately validate the simulations. Furthermore, as it was previously referred to, Morgado [3] is currently working on a new design for a more efficient rear wing. His design might result in losses of downforce in the rear of the car together with an additional nose down moment. The designs analyzed in sec. 4.2 can also be used as a compensation mechanism to guarantee similar pressure distribution and therefore similar handling.

Bearing this in mind, since the main focus, as referred to, was the MBR group, and given that the overall C_L is practically the same, the chosen design for the wind tunnel tests, is the rounded one (displayed on fig 4.17).

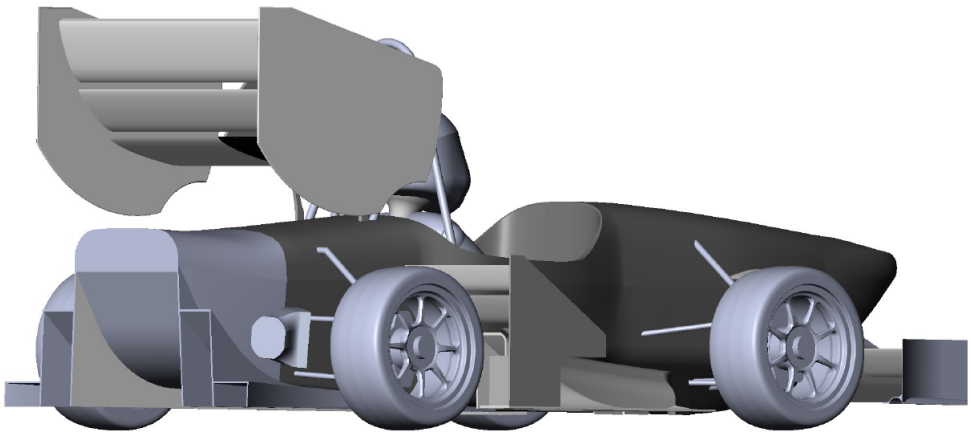

Figure 4.17: Rear-side view of chosen design

Chapter 5

CFD Validation Using Wind Tunnel

The wind tunnel experimental phase of this work comprised three main stages: additive manufacture of the module, calibration, and proper testing. These will be presented next, followed by a discussion of the results of the wind tunnel testing.

5.1 Experimental Setup and Previous Notes

5.1.1 Manufacturing New Parts

Following the choice of the design, the new component was scaled to a third of its size and a careful process of guaranteeing compatibility was performed via CAD by creating matching holes and confirming the main measurements in order to ensure that the assembly of the model and the new module raises no concerns. In this section, the assembly of the new back diffuser and rear portion of the monocoque, when scaled, will be referred to as module.

To manufacture this module, to be in accordance with the rest of the model, making use of the available printing machines and materials, 3D printing was the method chosen. The first step was to divide the module into 5 different parts (figure 5.1 (a)) due to the size limitations of the *Ultimaker*^{TM} *2* printing machines that would be used. Then a CAD file with the part was imported to the *Ultimaker Cura* ^{TM} software to prepare the geometry and slice it according to the chosen printing parameters (as exemplified in figure 5.1 (b)). The software then returned a g-code file to be introduced on the printer.

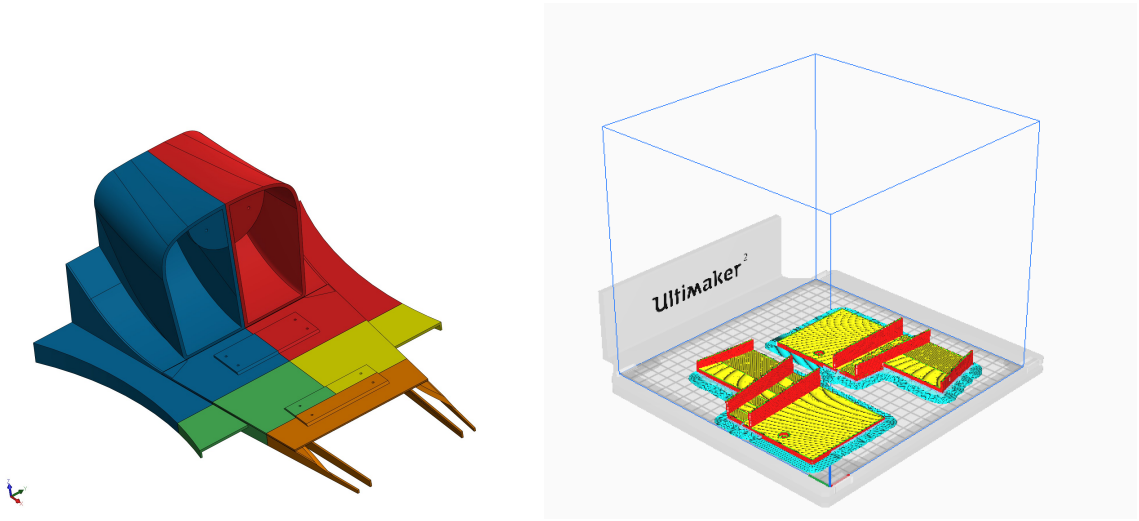

(a) 5-part module (b) Part on Cura

Figure 5.1: CAD designed module

The whole module took around 3 and a half days in cumulative printing time to be finished. After each part is collected from the printer, its supports are removed, its surface is sanded, and then it is ready to be assembled (figure 5.2).

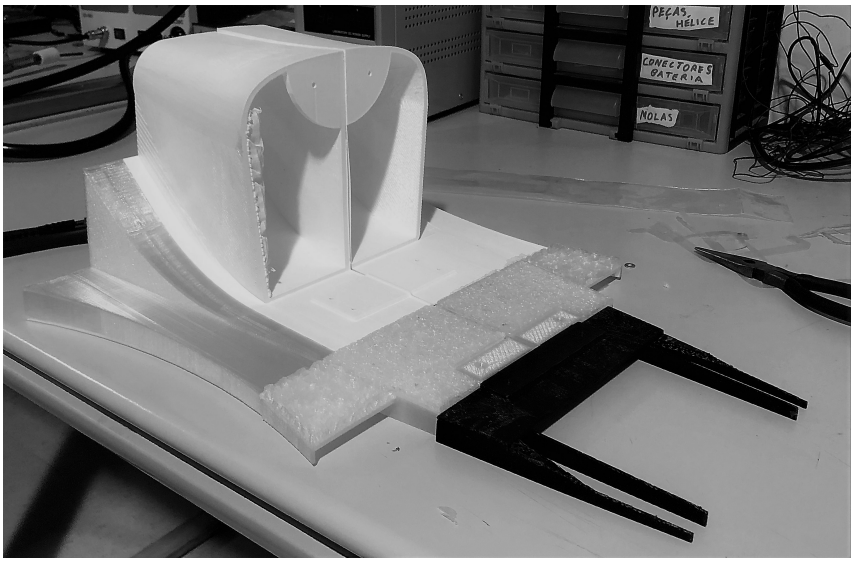

Figure 5.2: Printed module.

5.1.2 Force Balance Calibration

The forces and moments were measured with the balance produced by Oliveira [50]. This balance is composed of 6 sensing bars, each with a strain sensor associated, and its data is then collected by two *National Instruments*^{TM}*' NI 9237* acquisition systems. As part of their work, Oliveira [50] developed a downright methodology consisting of two *LabView*^{TM} interfaces, one for the force balance calibration and another for the wind tunnel tests, and a set of *MATLAB* scripts to convert the matrixes obtained

from calibration after some processing into the 6-degrees-of-freedom-formulas to be used to calculate the three aerodynamic forces and three aerodynamic moments by way correlating the 6 strains to the aerodynamic interest variables. This leaves to the user the freedom and responsibility to adequately choose the load cases and obtain the aforementioned matrices. The calibration matrix that converts the strains on the bars into forces and moments on the model can be found on fig. B.1.

With the reference values obtained from CFD, the load cases were defined and, making use of the calibration structure designed by Ferreira [7] and weight set provided by the Mechanical Engineering department (DEM), a total of the 170 distinct points resulting from 18 different load cases were collected.

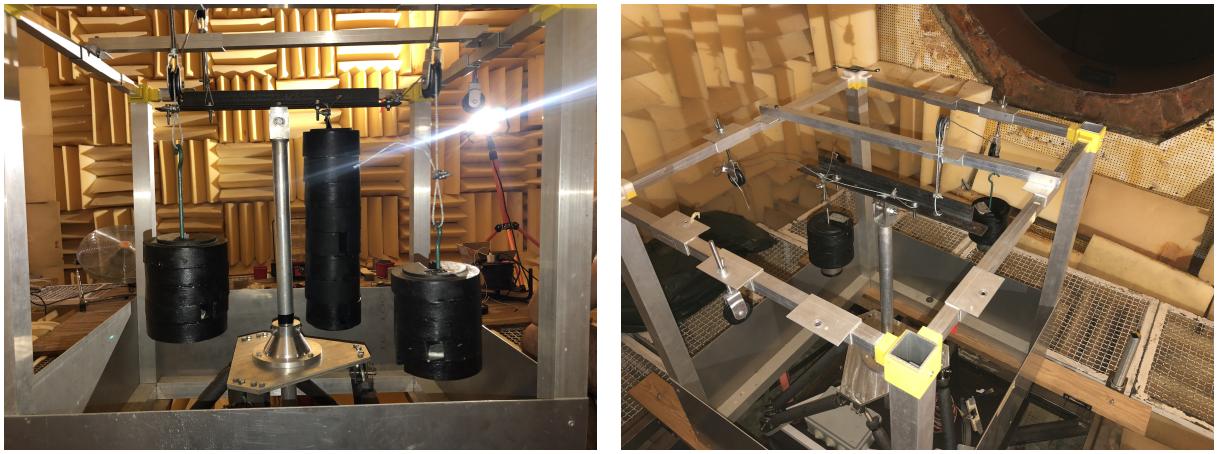

(a) Load case (b) Calibration structure

Figure 5.3: Calibration setup

To increase the set of data and, ultimately, increase the accuracy of the balance, after defining which component or set of components would be the focus of each load case, an excel sheet (fig. 5.4) was prepared in which each load was defined in terms of

- weight;
- point of application - as the loading bar has five different loading points (fig. 5.3 (a));
- direction of acting force - since, thanks to the pulleys in the structure, each point of application can be pushed in any wanted direction;
- time of application

For a list of all the load cases used for the calibration of the force balance, check fig. B.2.

From each load case, 30 seconds were given between loadings so that the strains were able to stabilize. From those 30 seconds, 7 were cut out of each end and the value of strain to be processed would be the average of the remaining 16 seconds. Figure 5.5 displays examples of the strains recorded on one of the bars for two different load cases. The red dashed line on (b) highlights the recovery of the extensometer since the value was nearly the same as in the beginning right after finishing the unload.

It is noteworthy that, since those forces and moments composed the only quantitative experimental result of this experimental phase, it was of utmost importance that these results were as reliable as

Load Case	11	Fx- Fz-My-
Material	#	
Gancho V	2	1N
Gancho P	1	5N
P1		1N
P5		5N
E10		10N
L10	5	10N
E20	6	20N
L20	3	20N

bilateral em x
barra alinhada com x
gancho verde em x e preto em y atrás
barra 7.5

Ensaio										
Tempo	X			Y			Z			
	massa	aplicado	total	massa	aplicado	total	massa	aplicado	total	
00:00			0			0			0	
00:30	1	gancho	1			0	6	grancho	6	
01:00	10	L10	11			0	20	x=7.5cm	26	L20
01:30			11			0	20	x=7.5cm	46	L20
02:00	10	L10	21			0	20	x=7.5cm	66	L20
02:30			21			0	30	x=7.5cm	96	E20
03:00	10	L10	31			0	30	x=7.5cm	126	E20
03:30	10	L10	41			0	30	x=7.5cm	156	E20
04:00	10	L10	51			0	30	x=7.5cm	186	E20
04:30	20	E20	71			0	30	x=7.5cm	216	E20
05:00										
05:30										
06:00										
06:30										

Figure 5.4: Load case sheet example.

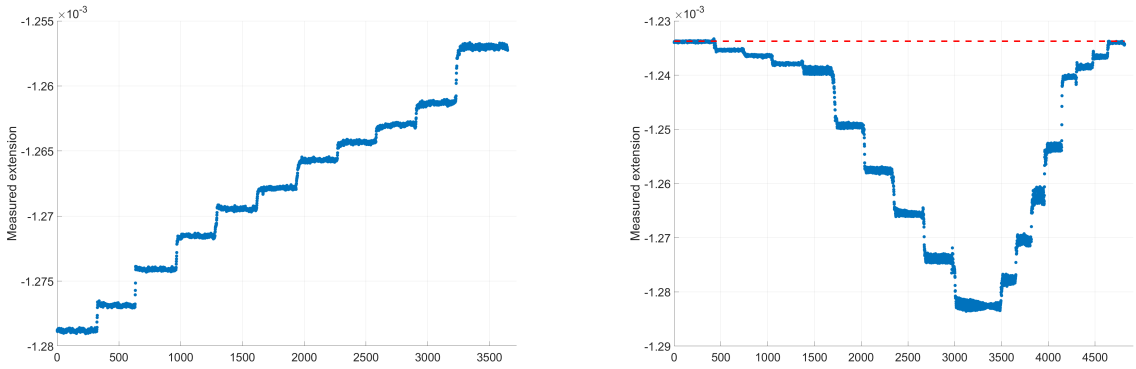

(a) Loading

(b) Loading and unloading

Figure 5.5: Extensometer data example cases

possible, and considering that the sensors are significantly sensitive, this whole calibration process, as well as the testing procedures, demanded extreme carefulness as not to spoil them. After this process, the results of the calibration were considered satisfactory.

5.1.3 Wind Tunnel Testing Procedure

Again, the testing procedure followed the basis executed in [2] and presented in figure 2.28. However, some adaptations, which will be referred to next, were made in order to reduce the time spent and improve the results.

At first, given the limited tunnel time available and the prior experience on the tunnel of Pacheco [2], only straightline with no lateral wind tests were scheduled, being that also the main reason why the designs in Chap. 4 focused on this type of inflow conditions. Nevertheless, after some contact with the experimental setup, a practical way to efficiently rotate the whole structure opened the door for a new type of simulation - straightline with lateral wind - not only for the new model but also as a way to complement the work of [2]. Given this, both the old model and the new one were tested for three configurations: no lateral wind ($\beta = 0°$), light lateral wind intensity ($\beta = 4°$) and high lateral wind intensity ($\beta = 10°$), figure 5.6 (a) displays the rotated setup.

After making sure that the position of the car was adequate, namely the side angle, the wheels were not touching the ”floor” so that all the loads are transmitted to the balance, guaranteeing that the setup is

(a) Yaw testing setup

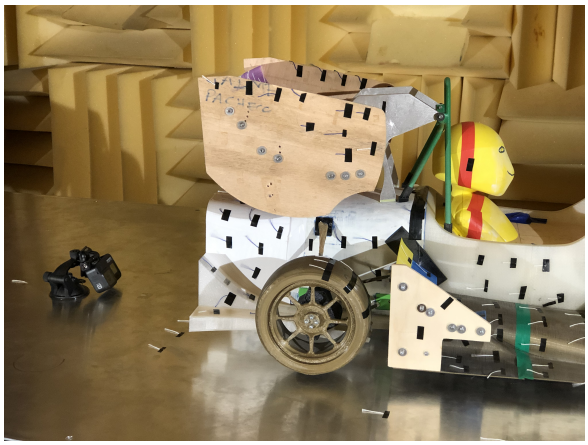

(b) Wool tufts and recording setup

Figure 5.6: WT mounting setups

safe for testing, meaning that there is no free tools or components and everything is correctly tightened up, and checking if the software is running, it was time for start recording that and turn on the WT motor. The testing itself consisted of increasing the airspeed to 15 m/s in the first stage and 25 m/s in the second stage. Every configuration was tested 3 times and careful monitoring of the recording as well as of the model was performed so that the test was repeated in the case of occurrence of any disturbance or unexpected behavior.

Given the state of balance looseness previously detected and already referred on Pacheco [2], instead of mounting the model in advance, for these tests, it was decided to mount immediately before the campaign in order not to force the balance. After the testing was done the model was left mounted for one day and the results varied more than 20%, which reinforced the decision made.

Additionally, to the monitored force results, wool tufts were placed on the module and both pictures and videos were captured resorting to video camera (fig. 5.6 (b)) mounted on the floor and to photographs so that some parallel can be drawn with the post-processing.

5.1.4 Limitations

Unfortunately, the experimental setup presents some limitations and, although being known beforehand, it is important that they are referred to and understood.

The first lacuna that comes into sight is the **static ground**. Most modern wind tunnels in which the testing is focused on cars are equipped with some sort of moving ground (usually made possible through a rotating belt). Its purpose is to better simulate racing conditions since, from the referential of the car, the floor is moving backwards, at the same speed as the approaching flow V_∞. In the absence of a moving floor, an unrealistic boundary layer will form on the floor surface; which is particularly undesirable because it might lead to choking of the flow under the car. Fago et al. [51] studied this effect and concluded that, especially for vehicles with low ground clearance, its impact is significant essentially because it alters the structure of the flow field around the car.

From the necessity to guarantee that the model is not touching anything other than the balance's

arm, so that all the forces are transmitted to it, arises the second problem: the **elevated, non-rotating wheels**. In a first instance, the absence of rotation will greatly influence the downwash upwind and the upwash downwind of the tire. Also, the airflow suffers significantly fewer disturbances and although this might mean the components downwind will be receiving undisturbed flow, one cannot assume that the behavior will improve as the design of the car is thought with rotation in mind. Wickern et al. [52] On a slightly different study concluded that removing the rotating wheels, the drag would decrease by around 30 percent. Other than that, a fictional ground effect will appear bellow each tire, further influencing the aerodynamic forces and flow behavior of the model. The elevation of the tires will also demand an elevation of the whole car, increasing the ground clearance.

Additionally, the previously referred **looseness of the balance arm** will allow the model to pitch forward when the WT motor is turned off because the mass center is positioned forward to the balance's arm mounting. When the motor is turned on, the pitching shifts backwards and even if the forces do not suffer that much by this looseness alone, the whole model has to be further elevated to ensure that no wheel touches the floor. When the distance between the ground and the undercar is increased, the diffusers (which contribute highly to the performance) become less effective and might even lose their purpose.

Concerning the wind tunnel airflow speed, the intended **Reynolds similarity was not possible**. Since the model's scale ratio is fixed at 1/3, to guarantee the Reynolds similarity, the inflow would have to achieve $45ms^{-1}$ (3 times higher than the $15ms^{-1}$ which is the full-size prototype speed). On a first instance, the maximum allowed airflow speed, for safety reasons, is $43ms^{-1}$ (990RPM) and though being close to the desired, Pacheco [2] concluded that for inflow speeds higher than $25ms^{-1}$ it would be impossible to stabilize the temperature (compromising not only the results but also the 3D printedmodel, which could partially melt). Other than that, for such high speeds, and due to the aforementioned looseness, the model would vibrate significantly more, harming the collected data.

Lastly, the fact that **only global forces and torques are being measured**, instead of individual contribution of components, hinders the perception of comparability with the simulations.

5.2 Results

5.2.1 CFD Simulations

Before building the model, CFD simulations on the setup with similar conditions to the wind tunnel facility developed by Pacheco [2] were performed to assess if the behavior corresponds to the one found in the full-size simulations. Table 5.1 reflects the relative changes between the baseline and the new designs in the downforce and drag of the main components at $\beta = 0°$ for the 1/3 scale model in the wind tunnel and the full-scale prototype on-road.

Table 5.1: Forces relative changes between original and new design on CFD simulations for full car and 1/3 model

	Downforce ($\Delta\%$)		Drag ($\Delta\%$)	
	Full	1/3 Model	Full	1/3 Model
Force Coefficient	+4.7	+4.5	+1.9	+2.7
Front Wing	-0.6	-2.4	-0.8	-5.4
Mono	-15	-18.3	-35.6	-39.8
Lateral Diffuser	+2.2	-1.4	+1.5	-4.2
Side Cascade	+6.8	+4.1	+4.7	+4.45
Back Diffuser	+344.1	+455.4	+452.1	+692.4
Rear Wing	+6.3	+4.2	+4.8	+6.6
MBR	+8.5	+10.9	+3.1	+4.05

From it, it can be retrieved that the trends observable on the full car are amplified for the case of the front wing, mono, and back diffuser, whereas for the rear wing and side cascade they were alleviated, and for the specific case of the lateral diffuser the trends shifted - for the 1/3 model case, the new design does not improve this device. The main differences between the simulations are the elevated car (which might explain the loss of performance of the lateral diffuser and, therefore, of the side cascade), the static ground and wheels, this asymmetry of the flow, and the not homogeneous airspeed at the inlet. Even so, as the general results, illustrated by the force coefficients, and the values concerning the main focused system (MBR) do not differ that much between the scaled and full-size simulations, and one can only measure global forces on the wind tunnel, the results were considered satisfactory.

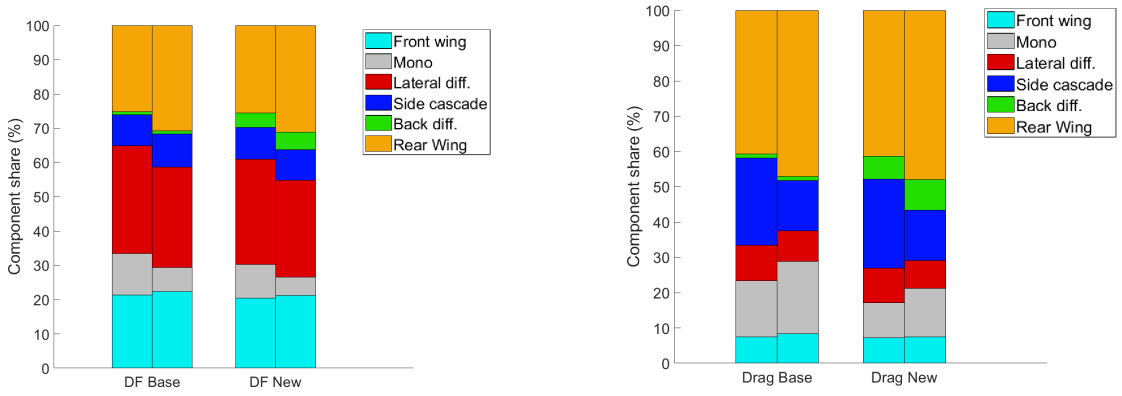

(a) Downforce (b) Drag

Figure 5.7: Comparison of CFD component share on forces

Fig 5.7 illustrates the contribution share of each component to the axial and vertical forces. The bar on the left of each corresponds to the full car and the one on the right to the 1/3 model.

Regarding the downforce, the stacked bars suggest an increase in the prevalence of the rear wing,

mostly compensated by the loss of contribution of the monocoque. This is verified both for the baseline and for the new designs.

When it comes to the drag generated, the rear wing gains importance again as well as the back diffuser, but contrarily to the case of the downforce case, the monocoque also increases its share. This time, the biggest loss of prevalence is verified on the side cascade, followed by the lateral diffuser.

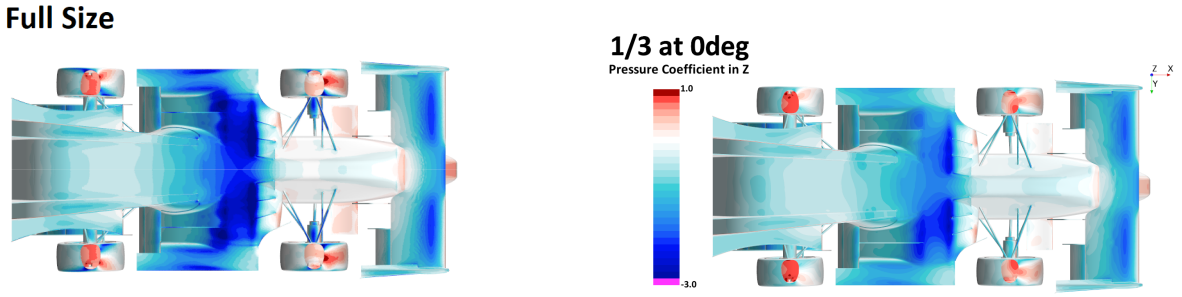

(a) Full size (b) 1/3 scale

Figure 5.8: C_{P_Z} comparison between full model and 1/3

Figure 5.8 suggests that, in absolute terms, the scaled model simulation suffers from a significant loss of downforce both on the front wing and on the center portion of the undertray. As previously mentioned, these regions make strong use of the ground effect so, by increasing the ground clearance, one can expect its performance to get worse (remember fig. 2.12 (b)). Fortunately, the rear diffuser does not appear to suffer from the same effect, as its pressure distribution does not differ much from the full-size simulation to the scaled one.

It is also noticeable that the pressure distribution on the scaled model is not symmetric. This is a result of the asymmetry of the anechoic chamber of the wind tunnel. In this case, the left side, which is the one closer to the wall, is generating more downforce, which might be a consequence of an unavoidable blockage effect.

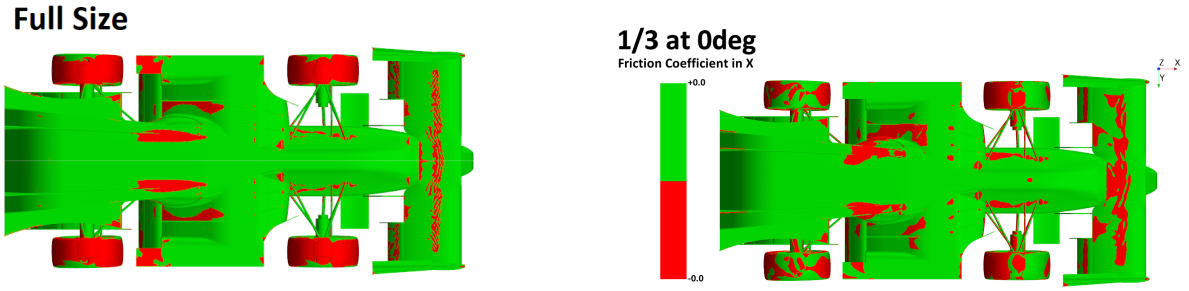

(a) Full size (b) 1/3 scale

Figure 5.9: C_{F_X} comparison between full model and 1/3

Fig. 5.9 displays the projection of the friction coefficient on the direction of the airflow, where the red reflects reversed flow regions. One can conclude that the patterns of separations are similar but that they are more severe on the scaled model, both on the front wing and the undertray. The afore-mentioned asymmetry helped the flow on the inner part of the left lateral diffuser to reattach, avoiding a

large separated region. Again, the flow on the added aft region seems to follow the full-size simulation behavior, which is highly desired for this study.

5.2.2 Wind Tunnel Testing

Following the procedures described in sec. 5.1.3, the wind tunnel testing comprised 18 runs: 3 for each yaw position (0°, 4° and 10°) for both the baseline model and the new one.

Fig. 5.10 depicts the forces and moments measured by the balance during the second run of the new model, for a slip angle of $\beta = 4°$. It will be used as an example since the remaining runs follow the same trends (except the 10° case). The red line represents the value obtained on the CFD, the solid blue represents the average value of the force/moment when the airspeed is 25m/s and the dashed blue line depicts the change between that value and the average of the initial and final values.

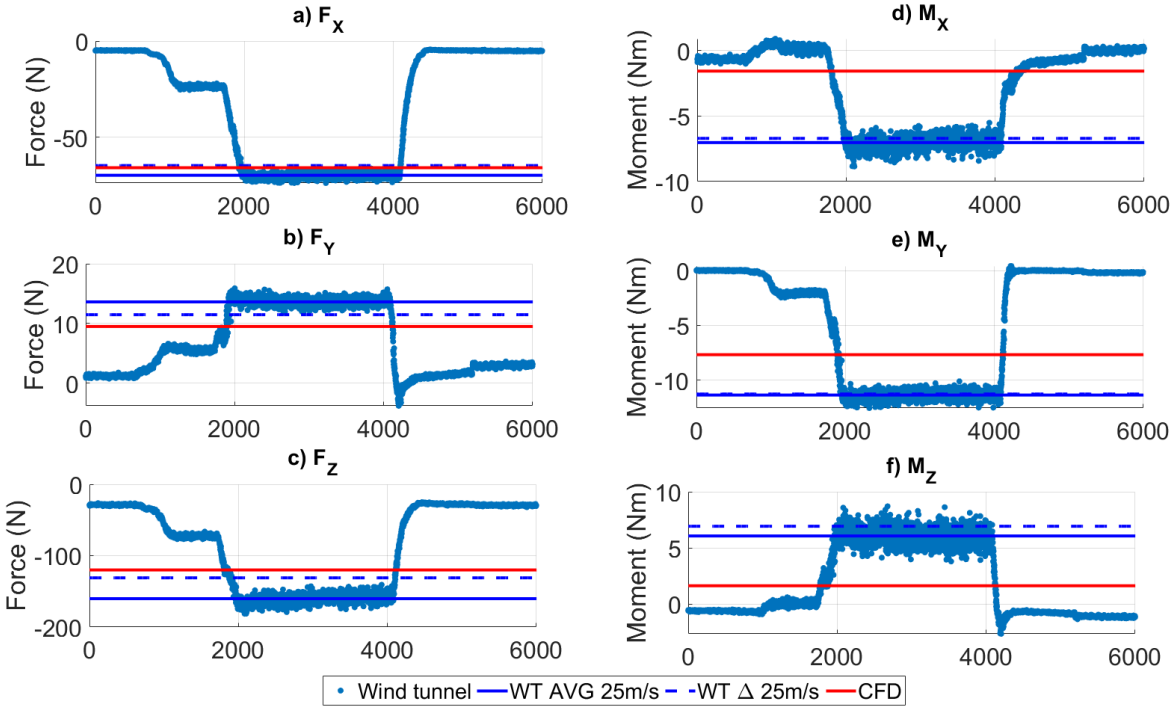

Figure 5.10: Forces and moments obtained for $\beta = 4°$ for 6000 samples

The comparison between the blue dashed line and the red one suggest that there was a good agreement between the forces measured on the wind tunnel and the CFD results, especially for the downforce and drag. In general terms, it is noticeable that, when compared to the wind tunnel testing, the CFD under-predicted the results and, while the difference is rather small for the case of the forces, it becomes substantial for the moments measured which were greatly magnified on the balance data. This might be due to the calibration process that, although concerning all these quantities, was primarily focused on accurately measuring the drag and downforce.

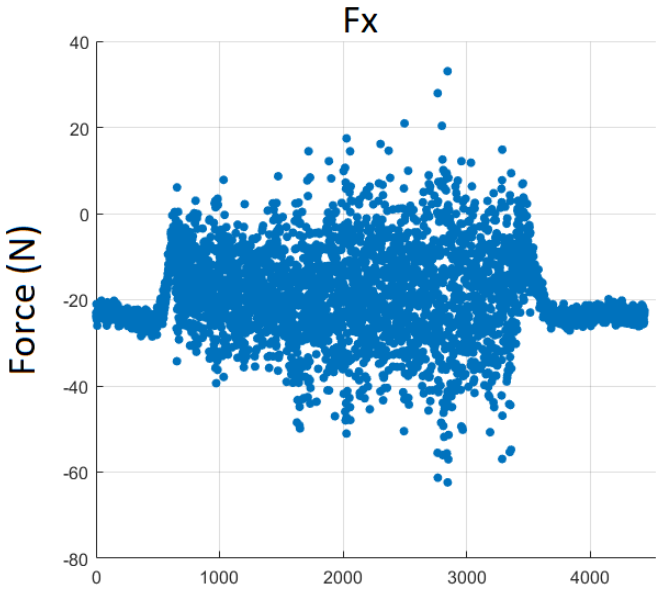

Figure 5.11: Downforce measure for $\beta = 10°$

While for the 0° and 4° cases, although overestimated, the wind testing results did follow the expected trends, this ceased to take place as the sideslip was increased to 10°, which can be confirmed on fig. 5.11. For the airflow speed tested, when $\beta = 10°$, the looseness of the balance arm became a critical factor, as it was observed that oscillations were highly amplified, leading to a highly unsteady environment of transient pitching, rolling, and yawing. These oscillations coupled with the calibration more directed to the straight case are probably the origin of the measurement error observed. For that reason, the analysis of the results will not concern the runs corresponding to this last case.

5.2.3 CFD vs EFD

One of the main purposes of this work is to assess if the increased performance due to the changes in the design that are verified on the CFD is confirmed by the wind tunnel experiments. Tables 5.2 and 5.3 gather the data of the changes in the overall downforce and drag between the original design and the new one with the added rear portion for the CFD simulations both on the full-sized car and on the 1/3 model, and for the wind tunnel testing.

By analyzing table 5.2, it can be retrieved that, in absolute terms, the downforces measured on the wind tunnel testing, for the new model, were higher than expected. Nevertheless, concerning the relative change from the original design to the new one, while slightly underestimating it, the CFD was able to predict it with good accuracy.

Table 5.2: Comparison of changes in downforce among CFD and wind tunnel testing

	CFD Full ($\Delta\%$)	CFD 1/3 ($\Delta\%$)	WT ($\Delta\%$)
0°	530.08 (+4.7)	119.8 (+4.5)	129.9 (+5.4)
4°	-	121.89 (+3.7)	134.46 (+3.8)
10°	-	112.33 (+2)	13.73 (-52.3)

Regarding the drag measurements (present on tab. 5.3), although the variations follow the simulated trends, the CFD ended up substantially under-predicting the drag values (2.7% to 4.2% and 3.6% to 5.7%). In terms of absolute value, despite the main focus being the trends, it is noticeable that for the case without slip angle, the drag measured on the WT testing differed less than 1% from the value predicted by the CFD.

Table 5.3: Drag comparison of changes among CFD and wind tunnel testing

	CFD Full ($\Delta\%$)	CFD 1/3 ($\Delta\%$)	WT ($\Delta\%$)
0°	220.44 (+1.9)	64.76 (+2.7)	64.57 (+4.2)
4°	-	65.81 (+3.6)	70.78 (+5.7)
10°	-	66.11 (+5.9)	32.37 (-37.2)

Given the aforementioned limitations, the results are considered satisfactory for the 0° and 4° cases. Taking into consideration the 10° case, the results reinforce what was stated in sec. 5.2.2 and the decision of not considering them for the analysis. A more complete table for the forces measured can be found on fig. A.1.

Figures 5.12 to 5.14 depict a comparison between the streamlines predicted by the CFD and the wool tufts glued to the surface of the car to try and capture the direction airflow on the vicinity of the wall.

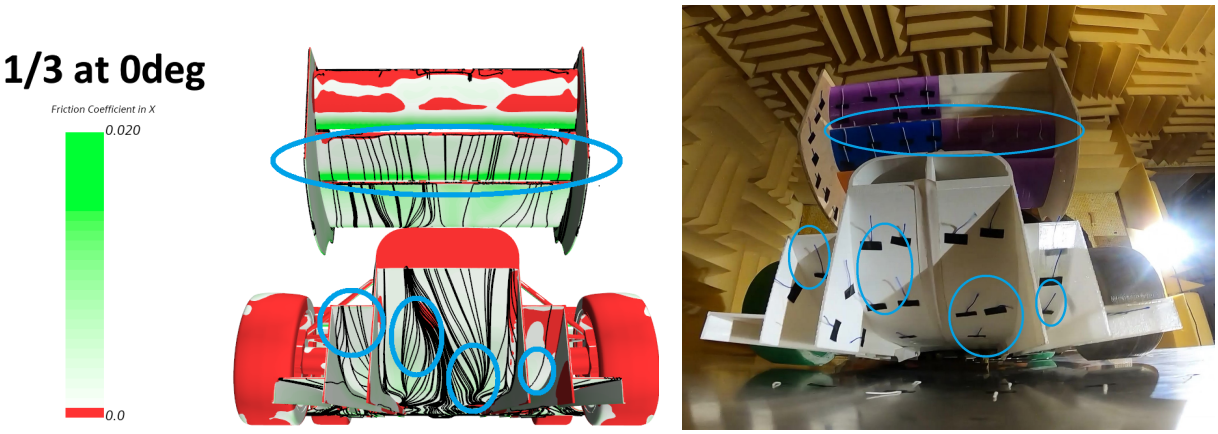

(a) CFD (b) WT

Figure 5.12: Rear view capture $\beta = 0°$

On global terms the wool tufts found on 5.12 seem to follow the expected direction both on the main

and secondary diffusers and on the rear wing flaps, however, due to its length, important phenomena, like the re-circulation bubbles on the third rear wing flap, were not captured. Moreover, some tufts look like they were captured by the high turbulence that the rear of the car is subjected to, losing its purpose.

(a) CFD (b) WT

Figure 5.13: Rear view capture $\beta = 4°$

Once the slip angle is increased, separation begins to take place on the back diffuser. Figure 5.13 suggests that some of the separated regions on the trailing edge of the diffuser on the right side of the car predicted by the CFD are also verified on the WT testing.

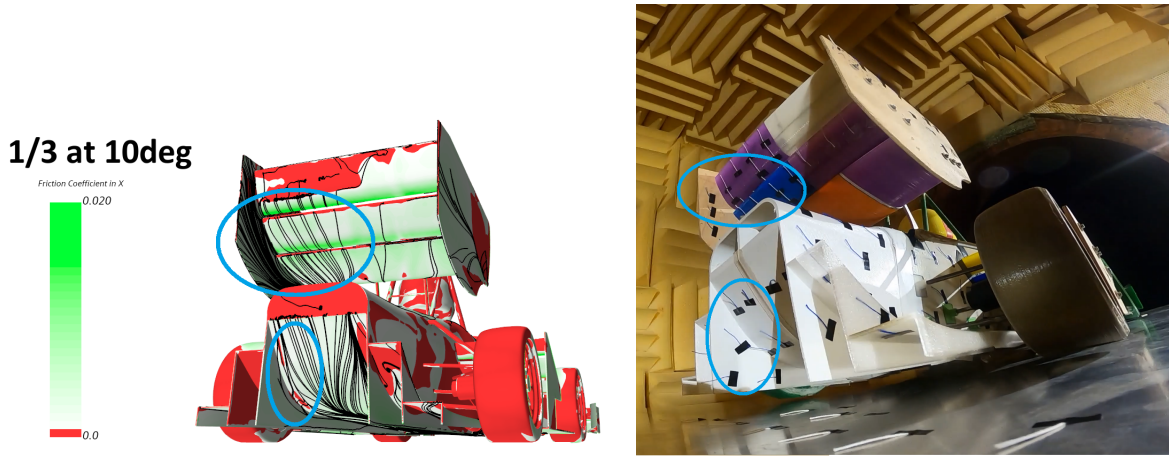

(a) CFD (b) WT

Figure 5.14: Rear view capture $\beta = 10°$

For the last case, where $\beta = 10°$, the separated regions on the secondary diffusers and the third rear wing flap were not captured by the wool tufts. One interesting effect that can be observed in this figure is that, for regions where the friction coefficient is higher (greener), the wool tufts seem to remain more attached to the surface of the model.

Chapter 6

Conclusions

6.1 Achievements

To achieve the main purpose of this work, many were the milestones reached on the way. As a starting point, by implementing some adaptations in the vehicle dynamics tool that simulates the hypothetical maximum score reachable given the car's parameters, it was concluded that the target downforce coefficient was $-C_lA = 5.75m^2$ and that the drag was not a limiting factor for FS competition.

From a baseline aerodynamic analysis, the main critical regions identified were the lateral diffuser, due to the large separation in its inner section, the rear wing, because it generates high drag, and the rear of the car including the back diffuser, as almost no attention had been given to it yet.

For the redesign phase, the lateral diffuser and the rear region were chosen. Two concepts were tested to mitigate the large separation on the lateral diffuser: reducing the expanding slope and slightly increasing the incidence of the side cascade elements downwind; redesigning the diffuser as an airfoil profile. Both proved to be satisfactory since separation was greatly minimized while the overall downforce generated was maintained, leaving much room for improvement (mostly on the latter) by redesigning the remaining components in accordance with these changes.

Regarding the changes in the aft region of the car, multiple designs were tested. Just by extending the monocoque, an increase in the overall downforce of just over 3% was verified. Inverting the top of this extended region proved to be favorable, as the overall performance was enhanced, mostly due to the increase in downforce generated by the rear wing and the back diffuser itself. By redesigning the diffuser profile, a total downforce coefficient of $3.832m^2$ was obtained (corresponding to a 4.3$\%$ gain from the original $3.674m^2$) for a round diffuser, and $3.812m^2$ for a profile with two subsequent expansion zones. For these designs, the efficiency of the car also improved by around 3%.

The design that contained the added round diffuser, which delivered the best results, was chosen. A 1/3 scale model was 3D printed and tested in the wind tunnel. CFD simulations on a setup with similar conditions to the wind tunnel facility were performed and yielded satisfactory results, as the main trends between the baseline and the new designs were verified as well as the pressure and friction distributions.

In terms of wind tunnel results, the CFD proved to correctly predict the measured forces while slightly

underestimating them, concerning the no slip-angle and $\beta = 4°$ cases. Regarding the measured moments, the values obtained were significantly larger than the prediction but it was considered a calibration issue instead of a CFD wrong prediction. The measurements for $\beta = 10°$ were considered unsatisfactory so they were not taken into account for the analysis.

On a concluding note, an aerodynamic study of the performance of the current model of the car, followed by a redesigning process of an underperforming region yielded better performance results from the CFD which were then validated in wind tunnel.

6.2 Future Work

Despite completing the purposed objectives, there is still room for improvement in most of the subjects studied in this work.

A more complex lap simulator could be developed, which could take into account the loads on all four wheels and car attitude through the described lap to increase the accuracy of the target aerodynamic coefficients and distribution.

The redesigned components presented in Chapter 4 may also be further improved. Regarding the lateral diffuser, to explore its full potential, the side cascade and rear wing should be adapted to the new designs so that the aerodynamic package can work as one. Concerning the rear region, a parametric study could be performed, i.e., changing the curvature and profile angles and finding the best combination.

Regarding the wind tunnel procedure, a better calibration method that deeply embraces the moments and not only the forces should be planned.

The looseness of the balance arm proved to be critical for the results obtained so an effort should be put into improving its rigidity as this would allow the car to be lowered and closer to real conditions. A way of rotating the wheels and moving the ground would also be highly desirable.

The current major drawback is that only global forces and moments are measured, which hinders the perception of validation, as one cannot actually understand the contribution of each device. Adding pressure sensors to the car would be a great way to bridge this gap. Some attention should also be paid to improving the flow visualization so that a parallel with the CFD can be drawn, for example, resorting to flowvis paint.

Bibliography

[1] M. Carreira. Aerodynamic mapping of a formula student prototype using numerical simulations and on-track validation. Master's thesis, Universidade de Lisboa - Instituto Superior Técnico, 2022.

[2] J. Pacheco. Wind tunnel testing of a complete formula student vehicle. Master's thesis, Universidade de Lisboa - Instituto Superior Técnico, 2022.

[3] J. Morgado. Design and testing of a rear wing for a formula student car. Master's thesis, Universidade de Lisboa - Faculdade de Ciências, 2022.

[4] C. Craig and M. A. Passmore. Methodology for the design of an aerodynamic package for a formula sae vehicle. *SAE International Journal of Passenger Cars-Mechanical Systems*, 7(2014-01-0596): 575–585, 2014.

[5] S. Wordley and J. Saunders. Aerodynamics for formula sae: a numerical, wind tunnel and on-track study. *SAE Transactions*, pages 744–756, 2006.

[6] S. Wordley and J. Saunders. Aerodynamics for formula sae: Initial design and performance prediction. Technical report, SAE Technical Paper, 2006.

[7] M. Ferreira. Design of a six-component external wind tunnel balance. Master's thesis, Universidade de Lisboa - Instituto Superior Técnico, 2015.

[8] B. Steinfurth, S. Feldhus, A. Berthold, and F. Haucke. Aerodynamic behavior of formula student open-wheel race car model with regard to head restraint/rear wing interaction. Technical report, SAE Technical Paper, 2018.

[9] K. R. Cooper, T. Bertenyi, G. Dutil, J. Syms, and G. Sovran. The aerodynamic performance of automotive underbody diffusers. *SAE transactions*, pages 150–179, 1998.

[10] A. Ruhrmann and X. Zhang. Influence of diffuser angle on a bluff body in ground effect. *J. Fluids Eng.*, 125(2):332–338, 2003.

[11] J. Katz. Aerodynamics of race cars. *Annu. Rev. Fluid Mech.*, 38:27–63, 2006.

[12] W. F. Milliken, D. L. Milliken, et al. *Race car vehicle dynamics*, volume 400. Society of Automotive Engineers Warrendale, PA, 1995.

[13] W. Bergman. The basic nature of vehicle understeer-oversteer. *SAE Transactions*, pages 387–422, 1966.

[14] H. Pacejka. *Tire and vehicle dynamics*. Elsevier, 2005.

[15] D. Bhosale, S. Rahate, K. Rege, and S. Palanivelu. To study the influence of variation in camber and toe on handling of passenger vehicle during cornering. Technical report, SAE Technical Paper, 2019.

[16] F. M. White. *Fluid mechanics*. McGraw-Hill series in mechanical engineering. McGraw-Hill Education, 8th edition in si units. edition, 2017.

[17] J. D. Anderson. *Fundamentals of aerodynamics*. McGraw-Hill series in aeronautical and aerospace engineering. McGraw Hill Education, sixth edition edition, 2017.

[18] V. d. Brederode. Fundamentos de aerodinâmica incompressível. *Edição do autor*, 1997.

[19] I. H. Abbott, A. E. Von Doenhoff, and L. Stivers Jr. Summary of airfoil data. 1945.

[20] J. Winslow, H. Otsuka, B. Govindarajan, and I. Chopra. Basic understanding of airfoil characteristics at low reynolds numbers (10 4–10 5). *Journal of Aircraft*, 55(3):1050–1061, 2018.

[21] F. P. Incropera, D. P. DeWitt, T. L. Bergman, A. S. Lavine, et al. *Fundamentals of heat and mass transfer*, volume 6. Wiley New York, 1996.

[22] T. Farrell and L. Miller. Development of a new boundary layer control technique for automotive wind tunnel testing. In *44th AIAA Aerospace Sciences Meeting and Exhibit*, page 356, 2005.

[23] E. L. Houghton and P. W. Carpenter. *Aerodynamics for engineering students*. Elsevier, 2003.

[24] J. Pauwelussen. *Essentials of vehicle dynamics*. Butterworth-Heinemann, 2014.

[25] S. McBeath. *Competition Car Aerodynamics 3rd Edition*. Veloce Publishing Ltd, 2017.

[26] J. Zerihan and X. Zhang. Aerodynamics of a single element wing in ground effect. *Journal of aircraft*, 37(6):1058–1064, 2000.

[27] X. Zhang and J. Zerihan. Aerodynamics of a double-element wing in ground effect. *AIAA journal*, 41(6):1007–1016, 2003.

[28] R. Ranzenbach and J. Barlow. Cambered airfoil in ground effect-an experimental and computational study. Technical report, SAE Technical Paper, 1996.

[29] X. Zhang and W. Toet. Ground effect aerodynamics research of racing cars. *AutoTechnology*, 6(6): 40–43, 2006.

[30] B. Green. *Fluid vortices*, volume 30. Springer Science & Business Media, 1995.

[31] J. Katz. Aerodynamics in motorsports. *Proceedings of the Institution of Mechanical Engineers, Part P: Journal of Sports Engineering and Technology*, 235(4):324–338, 2021.

[32] S. Leibovich. The structure of vortex breakdown. *Annual review of fluid mechanics*, 10(1):221–246, 1978.

[33] V. Y. Mudkavi. The phenomenon of vortex breakdown. In *Proceedings of the Fluid Dynamics Symposium*, pages 123–135, 1993.

[34] Fs rules 2021. Accessed: Nov 2021, url: https://www.formulastudent.de/fsg/rules/.

[35] J. Keogh, G. Doig, S. Diasinos, and T. Barber. The influence of cornering on the vortical wake structures of an inverted wing. *Proceedings of the Institution of Mechanical Engineers, Part D: Journal of Automobile Engineering*, 229(13):1817–1829, 2015.

[36] J. Wang, H. Li, Y. Liu, T. Liu, and H. Gao. Aerodynamic research of a racing car based on wind tunnel test and computational fluid dynamics. In *MATEC Web of Conferences*, volume 153, page 04011. EDP Sciences, 2018.

[37] W. A. Mokhtar and J. Lane. Racecar front wing aerodynamics. *SAE International Journal of Passenger Cars-Mechanical Systems*, 1(2008-01-2988):1392–1403, 2008.

[38] J. Katz, H. Luo, E. Mestreau, J. Baum, and R. Löhner. Viscous-flow simulation of an open-wheel race car. Technical report, SAE Technical Paper, 1998.

[39] Accessed: jan 2022, url: https://it.motorsport.com/f1/event/illustrazioni-2019/422045/.

[40] J. Katz and D. Garcia. Aerodynamic effects of indy car components. *SAE Transactions*, pages 2322–2330, 2002.

[41] J. Zerihan and X. Zhang. Aerodynamics of gurney flaps on a wing in ground effect. *AIAA journal*, 39(5):772–780, 2001.

[42] J. Katz. Aerodynamic model for wing-generated down force on open-wheel-racing-car configurations. *SAE Transactions*, pages 1106–1115, 1986.

[43] O. Ehirim, K. Knowles, and A. Saddington. A review of ground-effect diffuser aerodynamics. *Journal of Fluids Engineering*, 141(2), 2019.

[44] D. L. Garcia and J. Katz. Trapped vortex in ground effect. *AIAA journal*, 41(4):674–678, 2003.

[45] Y. Kuya, K. Takeda, X. Zhang, S. Beeton, and T. Pandaleon. Flow separation control on a race car wing with vortex generators in ground effect. *Journal of fluids engineering*, 131(12), 2009.

[46] O. Reynolds. On the dynamical theory of incompressible viscous fluids and the determination of the criterion (reprinted from papers on mechanical and physical subjects, vol 2, pg 535-577, 1901). In *Proceedings of the Royal Society-Mathematical and Physical Sciences*, volume 451, pages 5–47. ROYAL SOC 6-9 CARLTON HOUSE TERRACE, LONDON SW1Y 5AG, ENGLAND, 1995.

[47] D. C. Wilcox. Formulation of the kw turbulence model revisited. *AIAA journal*, 46(11):2823–2838, 2008.

[48] F. R. Menter. Two-equation eddy-viscosity turbulence models for engineering applications. *AIAA journal*, 32(8):1598–1605, 1994.

[49] Accessed: oct 2022, url: https://www.idealsimulations.com/resources/turbulence-models-in-cfd/.

[50] J. Oliveira. Design, construction, calibration and testing of a wind tunnel force balance. Master's thesis, Universidade de Lisboa - Instituto Superior Técnico, 2020.

[51] B. Fago, H. Lindner, and O. Mahrenholtz. The effect of ground simulation on the flow around vehicles in wind tunnel testing. *Journal of Wind Engineering and Industrial Aerodynamics*, 38(1): 47–57, 1991.

[52] G. Wickern, K. Zwicker, and M. Pfadenhauer. Rotating wheels-their impact on wind tunnel test techniques and on vehicle drag results. *SAE transactions*, pages 254–270, 1997.

Appendix A

Results

A.1 Wind Tunnel Testing

Downforce						
	Baseline			New design		
	CFD	CFD1/3	WT	CFD	CFD1/3	WT
0	253.123	114.597	123.248	265.042	119.805	129.902
4	-	117.547	129.550	-	121.893	134.456
10	-	110.179	28.789	-	112.334	13.729
Drag						
	Baseline			New design		
	CFD	CFD1/3	WT	CFD	CFD1/3	WT
0	108.199	63.040	61.982	110.223	64.755	64.574
4	-	63.546	66.958	-	65.812	70.778
10	-	62.454	51.546	-	66.115	32.369
Side Force						
	Baseline			New design		
	CFD	CFD1/3	WT	CFD	CFD1/3	WT
0	0.000	0.230	-12.462	0.000	-1.410	-8.993
4	-	5.777	15.040	-	9.566	5.183
10	-	14.496	9.970	-	20.991	-9.656

Figure A.1: Comparison of obtained forces among full size CFD, 1/3 scale CFD, and WT testing

A.2 Full Car CFD Data

General.SimulationNam	001_dBSLNE	002_sDif18	004_sDif15	009_sDifSC	016_sDifSC	018_sDifSC	020_sRound	021_sAirfo	022_sAirfo	023_sAirfo
General.CLA	3.674	3.623	3.580	3.680	3.704	3.688	3.605	3.707	3.551	3.676
General.CDA	1.569	1.570	1.550	1.589	1.590	1.584	1.564	1.580	1.531	1.551
General.MassFanRad	0.120	0.120	0.119	0.121	0.122	0.122	0.121	0.121	0.119	0.120
General.PressureFan	87.185	89.855	91.968	83.739	82.197	81.119	85.440	85.061	90.295	87.798
General.PressureRad	109.446	106.890	106.768	115.168	114.851	111.155	114.302	109.883	109.164	105.587
General.OriginM	-232.491	-232.393	-230.292	-236.882	-236.026	-235.668	-231.886	-225.359	-218.121	-223.371
General.Distribution	0.596	0.604	0.609	0.606	0.600	0.602	0.606	0.573	0.579	0.572
General.MassDiff	0.936	0.937	0.932	0.921	0.944	0.945	0.925	0.988	0.965	0.978
General.MassDiffBack	0.552	0.569	0.585	0.585	0.576	0.570	0.570	0.582	0.551	0.571
ClCd.CAR	2.342	2.308	2.311	2.317	2.329	2.329	2.305	2.346	2.320	2.370
ClCd.BDiff	2.256	1.847	2.403	2.232	2.539	2.150	2.371	1.935	2.317	2.150
ClCd.LDiff	8.450	9.192	9.148	9.201	9.174	9.238	8.777	7.604	7.827	8.308
ClCd.FW	7.660	7.660	7.668	7.636	7.637	7.642	7.660	7.631	7.659	7.666
ClCd.RW	1.662	1.662	1.674	1.656	1.702	1.704	1.654	1.658	1.645	1.606
ClCd.MONO	2.043	2.024	2.001	1.992	1.968	1.993	1.999	2.442	2.250	2.393
Downforce.Total	253.231	249.717	246.801	253.668	255.319	254.182	248.498	255.474	244.768	253.384
Downforce.BDiff	2.695	2.235	3.152	2.898	3.427	2.775	3.086	2.429	2.754	2.603
Downforce.LDiff	83.718	82.039	79.475	84.420	84.039	83.046	77.925	85.865	81.016	87.411
Downforce.FW	56.923	56.101	56.126	56.557	57.017	57.043	56.560	56.813	56.060	56.139
Downforce.RW	66.728	67.477	67.135	68.114	68.685	69.429	66.979	65.935	63.724	62.763
Downforce.MONO	32.026	31.128	30.425	31.460	31.043	31.032	31.242	34.240	33.035	34.845
Downforce.Under	118.439	115.403	113.052	118.778	118.510	116.852	112.254	122.534	116.804	124.860
Downforce.MDR	101.449	100.841	100.712	102.472	103.156	103.236	101.308	102.604	99.513	100.212
Downforce.SC	23.957	24.515	24.367	23.851	23.692	23.715	25.188	22.061	22.017	22.216
Drag.SC	24.456	25.031	24.871	24.343	24.216	24.214	25.714	22.563	22.546	22.741
Drag.Total	108.199	108.190	106.749	109.672	109.829	109.410	107.936	109.043	105.520	106.977
Drag.BDiff	1.195	1.210	1.311	1.298	1.350	1.291	1.302	1.255	1.189	1.211
Drag.LDiff	9.908	8.926	8.688	9.175	9.161	8.990	8.879	11.292	10.351	10.521
Drag.FW	7.432	7.324	7.319	7.407	7.466	7.464	7.384	7.445	7.320	7.323
Drag.RW	40.152	40.594	40.112	41.142	40.348	40.740	40.495	39.779	38.736	39.094
Drag.MONO	15.677	15.380	15.205	15.794	15.777	15.568	15.630	14.020	14.683	14.560
Drag.Under	36.687	34.441	33.892	35.442	35.448	34.839	34.688	37.860	36.573	36.814
Drag.MDR	57.024	57.184	56.627	58.234	57.475	57.599	57.426	55.054	54.608	54.864
Downforce.FW1	47.819	47.147	47.158	47.527	47.865	47.891	47.524	47.687	47.150	47.128
Downforce.FW2	6.553	6.484	6.490	6.523	6.593	6.592	6.524	6.586	6.450	6.523
Downforce.SC0	5.320	5.028	4.895	5.395	5.253	4.999	5.677	4.384	4.485	4.325
Downforce.SC1	5.685	5.834	5.743	6.054	4.406	4.238	6.022	4.823	4.797	5.099
Downforce.SC2	9.600	10.128	10.127	8.901	10.606	11.443	10.180	9.332	9.276	9.500
Downforce.SC3	3.850	4.040	4.108	3.994	3.952	3.533	3.836	4.024	3.988	3.817
Downforce.TYREF	-3.993	-3.882	-3.615	-4.540	-3.949	-4.164	-4.091	-3.869	-3.972	-4.385
Downforce.TYRER	-2.790	-3.037	-3.055	-2.533	-2.754	-2.992	-2.752	-2.651	-3.247	-2.649
Downforce.RW1	39.200	39.539	39.599	39.765	40.769	41.173	39.187	38.556	37.366	36.041
Downforce.RW2	18.074	18.367	18.118	18.562	18.392	18.596	18.222	18.029	17.316	17.462
Downforce.RW3	10.234	10.365	10.210	10.556	10.287	10.412	10.347	10.135	9.824	10.025
Downforce.BH	-5.446	-5.566	-5.591	-5.259	-5.248	-5.394	-5.442	-5.166	-5.379	-5.483
Drag.FW1	2.125	2.091	2.086	2.115	2.126	2.129	2.106	2.124	2.104	2.093
Drag.FW2	3.968	3.938	3.939	3.965	3.994	3.994	3.960	3.983	3.910	3.936
Drag.SC0	-1.470	-1.284	-1.213	-1.518	-1.503	-1.390	-1.603	-1.006	-1.031	-0.906
Drag.SC1	1.907	1.980	1.946	2.050	1.297	1.219	1.999	1.651	1.647	1.735
Drag.SC2	6.328	6.735	6.748	7.650	8.014	8.167	6.688	6.429	6.350	6.477
Drag.SC3	4.932	5.231	5.394	5.349	5.366	4.992	4.983	5.262	5.190	5.037
Drag.TYREF	6.101	6.190	6.300	6.334	6.161	6.370	6.407	6.621	6.742	6.708
Drag.TYRER	6.582	6.865	6.174	5.362	6.095	5.928	5.947	6.945	5.710	6.492
Drag.RW1	5.398	5.432	5.330	5.501	5.284	5.400	5.401	5.424	5.270	5.261
Drag.RW2	14.626	14.830	14.638	15.016	14.847	15.017	14.757	14.590	14.022	14.120
Drag.RW3	19.719	19.907	19.716	20.188	19.783	19.886	19.906	19.403	19.101	19.358
Drag.BH	0.175	0.191	0.137	0.179	0.221	0.184	0.181	0.187	0.177	0.162

Figure A.2: Lateral diffuser iterations

General.SimulationName	001_dBSLNE	003_bLongF	005_bDropF	007_bWideF	008_bLongF	011_bMiniF	012_bRndX	013_bStrXJ	014_bTriar	015_bRounc	017_bDoble	019_b2Succ
General.CLA	3.674	3.780	3.802	3.857	3.794	3.780	3.847	3.827	3.766	3.818	3.805	3.820
General.CDA	1.569	1.589	1.576	1.580	1.572	1.579	1.598	1.593	1.571	1.588	1.570	1.584
General.MassFanRad	0.120	0.121	0.121	0.119	0.120	0.120	0.120	0.120	0.119	0.121	0.119	0.119
General.PressureFan	87.185	85.416	83.745	90.002	88.650	88.537	89.054	87.894	90.832	85.175	90.615	92.754
General.PressureRad	109.446	110.896	114.354	104.513	107.334	106.754	107.584	107.236	106.370	106.311	104.936	104.101
General.Distribution	0.596	0.600	0.597	0.602	0.603	0.598	0.615	0.606	0.607	0.611	0.607	0.606
General.MassDiff	0.936	0.953	0.960	0.928	0.957	0.950	0.927	0.945	0.947	0.940	0.953	0.945
General.MassDiffBack	0.552	0.555	0.559	0.568	0.603	0.571	0.567	0.570	0.578	0.580	0.586	0.578
ClCd.CAR	2.342	2.379	2.412	2.441	2.413	2.394	2.405	2.403	2.398	2.405	2.423	2.411
ClCd.BDiff	2.256	3.034	2.689	2.100	2.632	1.407	1.769	1.872	2.382	1.805	1.815	1.780
ClCd.LDiff	8.450	8.569	8.818	8.799	8.566	8.681	8.457	8.921	8.617	8.573	9.046	8.834
ClCd.FW	7.660	7.656	7.642	7.639	7.656	7.625	7.647	7.629	7.674	7.611	7.683	7.672
ClCd.RW	1.662	1.663	1.683	1.695	1.701	1.688	1.686	1.699	1.685	1.695	1.681	1.695
ClCd.MONO	2.043	1.963	2.048	2.372	2.256	2.580	2.644	2.425	2.288	2.681	2.718	2.533
Downforce.Total	253.231	260.568	262.019	265.885	261.536	260.531	265.042	263.811	259.590	263.165	262.265	263.287
Downforce.BDiff	2.695	6.248	7.720	10.159	9.157	8.691	11.970	9.808	10.737	11.560	11.454	11.035
Downforce.LDiff	83.718	87.088	88.349	89.523	86.860	87.558	85.578	88.778	85.980	86.414	88.163	89.274
Downforce.FW	56.923	57.019	56.871	57.009	56.730	56.948	56.585	56.524	56.392	56.671	56.108	56.333
Downforce.RW	66.728	68.696	69.300	71.052	68.429	70.064	70.922	70.935	69.204	70.809	69.818	70.114
Downforce.MONO	32.026	29.420	28.191	26.614	29.428	26.139	27.206	27.319	26.811	26.964	27.094	26.704
Downforce.Under	118.439	122.756	124.260	126.295	125.445	122.387	124.755	125.905	123.529	124.937	126.710	127.013
Downforce.MDR	101.449	104.364	105.212	107.824	107.014	104.894	110.098	108.062	106.752	109.332	108.366	107.852
Downforce.SC	23.957	25.262	24.931	24.743	24.807	24.301	25.576	24.582	24.785	24.396	24.531	24.542
Drag.SC	24.456	25.812	25.464	25.255	25.332	24.816	25.607	25.089	25.328	24.921	25.042	25.062
Drag.Total	108.199	109.610	108.827	108.889	108.426	108.875	110.223	109.871	108.284	109.562	108.234	109.139
Drag.BDiff	1.195	2.059	2.871	4.836	3.480	6.179	6.596	5.239	4.509	6.406	6.312	6.199
Drag.LDiff	9.908	10.164	10.020	10.175	10.140	10.086	10.061	9.952	9.978	10.079	9.746	10.105
Drag.FW	7.432	7.448	7.442	7.463	7.410	7.469	7.374	7.409	7.349	7.446	7.303	7.342
Drag.RW	40.152	41.304	41.179	41.917	40.222	41.514	42.072	41.742	41.072	41.769	41.533	41.366
Drag.MONO	15.677	14.991	13.765	11.219	13.044	10.133	10.101	11.265	11.718	10.056	9.968	10.540
Drag.Under	36.687	37.378	36.676	36.404	36.803	36.483	36.818	36.408	36.183	36.621	35.772	36.950
Drag.MDR	57.024	58.354	57.816	57.972	56.746	57.825	58.769	58.246	57.299	58.232	57.813	58.106
Downforce.FW1	47.819	47.887	47.755	47.841	47.674	47.770	47.339	47.339	47.422	47.336	47.511	47.125
Downforce.FW2	6.553	6.573	6.575	6.611	6.531	6.625	6.542	6.542	6.583	6.541	6.626	6.496
Downforce.SC0	5.320	5.551	5.436	5.194	5.282	5.106	5.472	5.472	5.266	5.366	5.253	5.367
Downforce.SC1	5.685	6.024	6.075	5.808	5.908	5.859	6.085	6.085	5.959	6.028	5.806	5.759
Downforce.SC2	9.600	10.217	10.051	10.192	10.089	9.995	10.109	10.109	9.976	9.993	9.948	9.924
Downforce.SC3	3.850	4.021	3.902	4.062	4.054	3.857	3.942	3.942	3.887	3.941	3.915	3.991
Downforce.TYREF	-3.993	-4.302	-4.121	-4.411	-4.168	-3.971	-4.108	-4.108	-3.812	-4.164	-4.173	-3.887
Downforce.TYRER	-2.790	-2.991	-3.121	-2.611	-2.929	-2.926	-2.769	-2.769	-2.860	-2.838	-2.649	-3.096
Downforce.RW1	39.200	40.234	40.783	42.132	40.713	41.520	41.752	41.752	41.744	40.759	41.870	41.068
Downforce.RW2	18.074	18.643	18.781	19.051	18.228	18.786	19.227	19.227	19.290	18.701	19.066	18.941
Downforce.RW3	10.234	10.571	10.484	10.577	10.267	10.476	10.679	10.679	10.625	10.491	10.614	10.559
Downforce.BH	-5.446	-5.124	-5.447	-5.173	-5.618	-5.444	-5.427	-5.427	-5.518	-5.427	-5.348	-5.579
Drag.FW1	2.125	2.121	2.121	2.121	2.117	2.124	2.100	2.100	2.109	2.094	2.125	2.080
Drag.FW2	3.968	3.983	3.987	4.005	3.963	4.007	3.967	3.967	3.984	3.956	3.999	3.941
Drag.SC0	-1.470	-1.597	-1.500	-1.446	-1.413	-1.346	-1.444	-1.444	-1.325	-1.423	-1.404	-1.490
Drag.SC1	1.907	2.004	2.020	1.956	2.007	1.991	2.037	2.037	2.029	2.032	1.978	1.943
Drag.SC2	6.328	6.699	6.600	6.679	6.664	6.584	6.655	6.655	6.587	6.589	6.558	6.511
Drag.SC3	4.932	5.233	5.077	5.214	5.227	5.001	5.126	5.126	5.066	5.136	5.064	5.124
Drag.TYREF	6.101	6.186	6.495	6.093	6.464	6.128	6.317	6.317	6.242	6.244	6.116	6.592
Drag.TYRER	6.582	5.907	5.280	5.352	6.157	5.520	6.073	6.073	6.288	5.975	6.378	5.835
Drag.RW1	5.398	5.546	5.591	5.903	5.357	5.757	5.781	5.781	5.610	5.560	5.730	5.661
Drag.RW2	14.626	15.040	15.124	15.439	14.684	15.228	15.495	15.495	15.462	15.072	15.385	15.285
Drag.RW3	19.719	20.268	20.011	20.105	19.777	20.068	20.307	20.307	20.186	20.009	20.189	20.128
Drag.BH	0.175	0.224	0.180	0.215	0.133	0.186	0.196	0.196	0.174	0.186	0.189	0.153

Figure A.3: Aft region iterations

Appendix B

Calibration

It is possible to add PDF files to the document, such as technical sheets of some equipment used in the work.

B.1 Equations and Load Cases

$$R = \begin{bmatrix} -55.8418 & 43.3085 & 148.6382 & 1.5249 & 12.0463 & -56.4112 \\ 30.3599 & 37.3178 & -36.2455 & 2.9950 & 1.8995 & 4.1164 \\ -116.2311 & -116.7215 & 126.8305 & -14.7526 & 2.0050 & -39.5317 \\ -3.9885 & 8.1747 & 3.7103 & -0.3486 & 2.5804 & -7.2226 \\ 7.8070 & 2.8220 & 46.5544 & 13.7152 & -8.1607 & 9.7655 \\ 30.7660 & -8.8558 & -18.6696 & 2.0875 & -8.1602 & 29.3108 \\ 0.0251 & -0.0073 & -0.0064 & 3.70E-05 & -0.0038 & 0.0155 \\ 0.0068 & 0.0058 & 0.0056 & 0.0008 & -0.0020 & 0.0028 \\ 0.0079 & 0.0272 & 0.0628 & 0.0034 & -0.0047 & 0.0116 \\ 0.0026 & -0.0038 & -0.0001 & 0.0003 & -0.0015 & 0.0039 \\ 0.0009 & 0.0013 & 0.0034 & 0.0022 & -0.0012 & 0.0015 \\ 0.0043 & -0.0013 & -0.0062 & -0.0010 & -0.0005 & 0.0017 \\ 0.0138 & 0.0052 & 0.0493 & 0.0026 & -0.0063 & 0.0061 \\ -0.0050 & -0.0100 & -0.0842 & 0.0013 & 0.0057 & -0.0045 \\ 0.0356 & -0.0217 & -0.0634 & -0.0002 & -0.0081 & 0.0320 \\ -0.0052 & 0.0083 & 0.0298 & 0.0013 & 0.0001 & -0.0104 \\ -0.0199 & 0.0092 & 0.0042 & 0.0029 & 0.0030 & -0.0112 \\ -0.0151 & -0.0233 & -0.0534 & -0.0041 & 0.0057 & -0.0114 \\ -0.0116 & -0.0160 & 0.0273 & -0.0008 & -0.0023 & -0.0005 \\ 0.0183 & 0.0104 & -0.0458 & -0.0008 & -0.0012 & 0.0013 \\ 0.0024 & 0.0006 & -0.0495 & -0.0020 & 0.0022 & -0.0006 \\ 0.0545 & 0.0530 & -0.0845 & 0.0062 & 0.0004 & 0.0168 \\ -0.0389 & -0.0284 & 0.0698 & -0.0006 & 0.0033 & -0.0078 \\ -0.0108 & -0.0031 & 0.0700 & 0.0008 & -0.0010 & -0.0005 \\ -0.0010 & 0.0006 & -0.0296 & -0.0069 & 0.0039 & -0.0059 \\ -0.0168 & 0.0050 & -0.0002 & -0.0012 & 0.0048 & -0.0154 \\ 0.0046 & 0.0003 & -0.0153 & -0.0001 & -0.0003 & 0.0051 \end{bmatrix}^T \begin{bmatrix} r1 \\ r2 \\ r3 \\ r4 \\ r5 \\ r6 \\ r1^2 \\ r2^2 \\ r3^2 \\ r4^2 \\ r5^2 \\ r6^2 \\ r1*r2 \\ r1*r3 \\ r1*r4 \\ r1*r5 \\ r1*r6 \\ r2*r3 \\ r2*r4 \\ r2*r5 \\ r2*r6 \\ r3*r4 \\ r3*r5 \\ r3*r6 \\ r4*r5 \\ r4*r6 \\ r5*r6 \end{bmatrix}$$

Figure B.1: Calibration equations

Load Case	Iteration	Fx [N]	Fy [N]	Fz [N]	Mx [Nm]	My [Nm]	Mz [Nm]
1 Fx-	0	0	0	-8.3	0	0	0
	0.5	-5	0	-8.3	0	0	0
	1	-15	0	-8.3	0	0	0
	2	-25	0	-8.3	0	0	0
	3	-35	0	-8.3	0	0	0
	4	-45	0	-8.3	0	0	0
	5	-55	0	-8.3	0	0	0
	6	-65	0	-8.3	0	0	0
	7	-75	0	-8.3	0	0	0
	8	-85	0	-8.3	0	0	0
	9	-105	0	-8.3	0	0	0
2 Fz-	0	0	0	-8.3	0	0	0
	0.5	0	0	-14.3	0	-0.48	0
	1	0	0	-34.3	0	-0.48	0
	2	0	0	-54.3	0	-0.48	0
	3	0	0	-74.3	0	-0.48	0
	4	0	0	-94.3	0	-0.48	0
	5	0	0	-114.3	0	-0.48	0
	6	0	0	-134.3	0	-0.48	0
	7	0	0	-154.3	0	-0.48	0
	8	0	0	-174.3	0	-0.48	0
	9	0	0	-194.3	0	-0.48	0
	10	0	0	-214.3	0	-0.48	0
	11	0	0	-234.3	0	-0.48	0
3 Fy+	0	0	0	-8.3	0	0	0
	0.5	0	1	-8.3	0	0	0
	1	0	6	-8.3	0	0	0
	2	0	11	-8.3	0	0	0
	3	0	21	-8.3	0	0	0
	4	0	31	-8.3	0	0	0
	5	0	41	-8.3	0	0	0
	6	0	51	-8.3	0	0	0
4 My-	0	0	0	-8.3	0	0	0
	0.5	0	0	-8.3	0	-0.24	0
	1	0	0	-8.3	0	-2.64	0
	2	0	0	-8.3	0	-5.04	0
	3	0	0	-8.3	0	-7.44	0
	4	0	0	-8.3	0	-12.24	0
	5	0	0	-8.3	0	-17.04	0
5 Mx+	0	0	0	-8.3	0	0	0
	0.5	0	0	-8.3	0.24	0	0
	1	0	0	-8.3	1.44	0	0
	2	0	0	-8.3	3.84	0	0
	3	0	0	-8.3	6.24	0	0
	4	0	0	-8.3	8.64	0	0
	5	0	0	-8.3	11.04	0	0
6 Mx-	0	0	0	-8.3	0	0	0
	0.5	0	0	-8.3	-0.24	0	0
	1	0	0	-8.3	-1.44	0	0
	2	0	0	-8.3	-3.84	0	0
	3	0	0	-8.3	-6.24	0	0
	4	0	0	-8.3	-8.64	0	0
	5	0	0	-8.3	-11.04	0	0
7 Mz+	0	0	0	-8.3	0	0	0
	0.5	0	0	-8.3	0	0	0.14
	1	0	0	-8.3	0	0	1.54
	2	0	0	-8.3	0	0	2.94
	3	0	0	-8.3	0	0	4.34
	4	0	0	-8.3	0	0	5.74
	5	0	0	-8.3	0	0	7.14
7A Mz+	0	0	0	-8.3	0	0	0
	0.5	0	0	-8.3	0	0	-0.14
	1	0	0	-8.3	0	0	-1.54
	2	0	0	-8.3	0	0	-2.94
	3	0	0	-8.3	0	0	-4.34
	4	0	0	-8.3	0	0	-5.74
	5	0	0	-8.3	0	0	-7.14
8 Fx-Fz-	0	-5	0	-10.3	0	-0.48	0
	0.5	-15	0	-30.3	0	-0.48	0
	1	-15	0	-50.3	0	-0.48	0
	2	-25	0	-70.3	0	-0.48	0
	3	-25	0	-90.3	0	-0.48	0
	4	-35	0	-110.3	0	-0.48	0
	5	-35	0	-130.3	0	-0.48	0
	6	-45	0	-150.3	0	-0.48	0
	7	-45	0	-170.3	0	-0.48	0
	8	-55	0	-190.3	0	-0.48	0
	9	-55	0	-210.3	0	-0.48	0
	10	-75	0	-230.3	0	-0.48	0
9 Fx-My-	0	0	0	-8.3	0	-0.48	0
	0.5	-1	0	-8.3	0	-1.68	0
	1	-11	0	-8.3	0	-4.08	0
	2	-21	0	-8.3	0	-6.48	0
	3	-31	0	-8.3	0	-8.88	0
	4	-41	0	-8.3	0	-13.68	0
	5	-51	0	-8.3	0	-18.48	0
	6	-71	0	-8.3	0	-23.28	0

Load Case	Iteration	Fx [N]	Fy [N]	Fz [N]	Mx [Nm]	My [Nm]	Mz [Nm]
10 Fz- My-	0	0	0	-8.3	0	-0.28	0
	0.5	0	0	-14.3	0	-0.7	0
	1	0	0	-34.3	0	-2.1	0
	2	0	0	-54.3	0	-3.5	0
	3	0	0	-74.3	0	-4.9	0
	4	0	0	-84.3	0	-7.5	0
	5	0	0	-94.3	0	-10.1	0
	6	0	0	-104.3	0	-12.7	0
	7	0	0	-114.3	0	-15.3	0
	8	0	0	-124.3	0	-17.9	0
11 Fx-Fz- My-	0	0	0	-8.3	0	-0.28	0
	0.5	-1	0	-14.3	0	-0.7	0
	1	-11	0	-34.3	0	-2.1	0
	2	-11	0	-54.3	0	-3.5	0
	3	-21	0	-74.3	0	-4.9	0
	4	-21	0	-84.3	0	-7.5	0
	5	-31	0	-94.3	0	-10.1	0
	6	-41	0	-104.3	0	-12.7	0
	7	-51	0	-114.3	0	-15.3	0
	8	-71	0	-124.3	0	-17.9	0
12 Fz- Mx+	0	0	0	-8.3	0	0	0
	0.5	0	0	-13.3	0.6	0	0
	1	0	0	-23.3	1.8	0	0
	2	0	0	-33.3	3	0	0
	3	0	0	-43.3	4.2	0	0
	4	0	0	-53.3	5.4	0	0
	5	0	0	-63.3	6.6	0	0
	6	0	0	-83.3	9	0	0
13 Fz- Mx-	0	0	0	-8.3	0	0	0
	0.5	0	0	-13.3	-0.6	0	0
	1	0	0	-23.3	-1.8	0	0
	2	0	0	-33.3	-3	0	0
	3	0	0	-43.3	-4.2	0	0
	4	0	0	-53.3	-5.4	0	0
	5	0	0	-63.3	-6.6	0	0
	6	0	0	-83.3	-9	0	0
14 Fy+ Mz-	0	0	0	-8.3	0	0	0
	0.5	0	1	-8.3	0	0	0.192
	1	0	11	-8.3	0	0	2.112
	2	0	21	-8.3	0	0	4.032
	3	0	31	-8.3	0	0	5.952
	4	0	41	-8.3	0	0	7.872
	5	0	51	-8.3	0	0	9.792
14A Fy+ Mz+	0	0	0	-8.3	0	0	0
	0.5	0	1	-8.3	0	0	-0.192
	1	0	11	-8.3	0	0	-2.112
	2	0	21	-8.3	0	0	-4.032
	3	0	31	-8.3	0	0	-5.952
	4	0	41	-8.3	0	0	-7.872
	5	0	51	-8.3	0	0	-9.792
15 Fy+ Fz- My- Mz+	0	0	0	-8.3	0	-0.28	0
	0.5	0	1	-14.3	0	-0.7	0.192
	1	0	1	-34.3	0	-2.1	0.192
	2	0	1	-54.3	0	-3.5	0.192
	3	0	1	-74.3	0	-4.9	0.192
	4	0	11	-84.3	0	-7.5	2.112
	5	0	21	-94.3	0	-10.1	4.032
	6	0	31	-104.3	0	-12.7	5.952
	7	0	41	-114.3	0	-15.3	7.872
	8	0	51	-124.3	0	-17.9	9.792
15A Fy+ Fz- My- Mz-	0	0	0	-8.3	0	-0.28	0
	0.5	0	1	-14.3	0	-0.7	-0.192
	1	0	1	-34.3	0	-2.1	-0.192
	2	0	1	-54.3	0	-3.5	-0.192
	3	0	1	-74.3	0	-4.9	-0.192
	4	0	11	-84.3	0	-7.5	-2.112
	5	0	21	-94.3	0	-10.1	-4.032
	6	0	31	-104.3	0	-12.7	-5.952
	7	0	41	-114.3	0	-15.3	-7.872
	8	0	51	-124.3	0	-17.9	-9.792
16 Fy- Mz+	0	0	0	-8.3	0	0	0
	0.5	-5	0	-8.3	0	0	0.96
	1	-25	0	-8.3	0	0	4.8
	2	-45	0	-8.3	0	0	8.64
	3	-65	0	-8.3	0	0	12.48
	4	-85	0	-8.3	0	0	16.32
	5	-105	0	-8.3	0	0	20.16
16A Fy- Mz-	0	0	0	-8.3	0	0	0
	0.5	-5	0	-8.3	0	0	-0.96
	1	-25	0	-8.3	0	0	4.8
	2	-45	0	-8.3	0	0	-8.64
	3	-65	0	-8.3	0	0	12.48
	4	-85	0	-8.3	0	0	-16.32
	5	-105	0	-8.3	0	0	20.16

Figure B.2: Full list of calibration load cases